Nanostructured and Photoswitchable Biointerfaces for Controlling Cell Adhesion

Dissertation by

Laith F. Kadem

Submitted to the Faculty of Engineering
Christian-Albrechts University of Kiel, Germany
for the degree of Doctor of Engineering Sciences

2016

Declaration

I hereby declare that I wrote this dissertation by myself without improper external assistance and to the best of my knowledge and belief and that I have identified all quotations of other authors and used none but the indicated sources.

Laith F. Kadem
Christian-Albrechts-Universität zu Kiel

Date: Signature:

Reviewers:

Prof. Dr. Christine Selhuber-Unkel
Prof. Dr. Rainer Adelung

Date for the oral exam: 27.06.2016

To my family

Abstract

Cells are the smallest living units of life. Their ability to assemble allows for the formation of tissues and organs in multicellular organisms. The formation of a multicellular organism as well as maintaining it are two mechanisms that are predominantly regulated by the cells' capability to interact with each other and with their extracellular matrix. These interactions are complex and highly regulated processes, which play a crucial role in numerous fundamental cellular functions such as motility, proliferation and differentiation. They are primarily controlled by cell adhesion, which is an important cellular mechanism that is chiefly mediated by cell adhesion molecules such as integrins.

In this work, I present two novel approaches that enable a control of cell adhesion. The first approach provides a static spatial control while the other offers a reversible dynamic control at both cell- and molecular levels. In the first approach, a static control of cell adhesion is enabled by a biocompatible microstructured interface that accommodates an additional pattern of quasi-hexagonally ordered gold nanoparticles. The superposition of these two structures to generate a so-called micronanostructure is highly advantageous in numerous applications. For instance, changing the surface pattern of nano- and microstructured biofunctionalized substrates has a large impact on the adhesion of living cells. Thus, the ability of micronanostructures to spatially control surface patterns makes them eminently suitable interfaces for controlling cell adhesion at the micro- and nanometer level. The production of the micronanostructures has been realized using both photolithography and Block-Copolymer Micelle Nanolithography (BCML). First, the microstructured substrate has been prepared in a two-step photolithography process. Then, it has been followed by a subsequent BCML step to deposit the gold nanoparticles. The combination of particle self-assembly and the pre-structured patterns offers a controlled allocation of gold nanoparticle distribu-

tions, i.e. it is possible to obtain different interparticle spacings on adjacent segments of the same substrate. This novel strategy is a promising method for fabricating regular metallic nanopatterns on various types of substrates for a wide range of applications that demand a controlled allocation of nanostructures. Examples include DNA chips, nanowires and optically active nanocoatings.

Despite the spatial control offered by this approach, it neither resembles nor reflects upon the dynamic behavior of cells *in vivo* as it provides a static and stable interface. To overcome this limitation, I present a second approach that allows a rapid, reversible and dynamic way of controlling cell adhesion. The reversible switching in this approach has been fulfilled using two different surface chemistries, both of which are based on using light-responsive azobenzene molecules, which are capable of switching between two isomeric states, namely *trans* and *cis*. These azobenzenes have been biofunctionalized with RGD (Arginine-Glycine-Aspartate) peptides and immobilized, alongside a biologically inert monolayer of polyethylene glycol (PEG), onto glass surfaces. The first surface type modulates cell adhesion through UV illumination, which triggers a switching of the thermally stable *trans* isomer to the *cis* configuration. This isomerization leads to immersing the RGD peptide into the nonadhesive PEG background. A subsequent illumination with visible light yields a thermal reversion into the *trans* configuration, which makes the RGD available again for cellular binding. This method embodied a true and rapid reversibility of cell adhesion as confirmed by studies carried out using atomic force spectroscopy. However, this method has the inconvenience of needing two wavelengths to perform a two-way switching. This shortcoming can be overcome using a slightly different surface chemistry for providing a dynamic reversible switching of cell adhesion, which is based on using the push-pull type of azobenzenes. These azobenzenes offer an intriguing and unconventional method that allows the system to be set reversibly between two phases using a single wavelength within the visible spectrum. The first phase is a state of rapid *trans*/*cis* switching of the push-pull azobenzene that takes place during exposure to a 530 nm light, which induces an oscillation of the azobenzene. The second phase is set once the light is switched off, which seizes the oscillation of the push-pull azobenzene and leads to a complete resetting of the *trans* configuration. This oscillation significantly reinforced cell adhesion forces and increased the gene expression of proteins involved in focal adhesion clusters. The results from these studies provide a significant milestone in understanding and regulating cellular mechanosensory mechanisms through molecularly-controlled mechanical stimuli at both cell and molecular levels.

The interfaces presented in this thesis provide novel concepts for controlling cell adhesion. They pave the way toward understanding unexplored properties of cell adhesion as well as designing innovative functional biomaterials.

Zusammenfassung

Zellen sind die kleinsten lebenden Einheiten, die das Leben ausmachen. Ihre Fähigkeit sich anzuordnen ermöglicht die Entwicklung von Geweben und Organen zu mehrzelligen Organismen. Die Bildung von Organismen und deren Erhalt werden vorwiegend dadurch reguliert werden, dass Zellen mit anderen Zellen und mit ihrer extrazellulären Matrix interagieren. Diese Wechselwirkungen sind komplexe und streng regulierte Prozesse, die eine entscheidende Rolle für zahlreiche fundamentale zelluläre Funktionen spielen. Dazu gehören die Zellbeweglichkeit, Proliferation und Differentiation. Sie alle werden maßgeblich durch die Zelladhäsion gesteuert, die vornehmlich durch Zelladhäsionsmoleküle, wie Integrine, gesteuert wird.

In dieser Arbeit stelle ich zwei Ansätze vor, die es ermöglichen die Zelladhäsion zu kontrollieren. Der erste Ansatz bietet eine statische, räumliche Kontrolle der Zelladhäsion, während der zweite Ansatz eine reversible, dynamische Kontrolle auf zellulärer und molekularer Ebene erlaubt. Im ersten Ansatz wird die Zelladhäsion durch eine biokompatible, mikrostrukturierte Grenzfläche kontrolliert, die mit einem zusätzlichen Muster von quasi-hexagonal angeordneten Goldnanopartikeln ausgestattet ist. Die Überlagerung dieser beiden Strukturen zu sogenannten Mikronanostrukturen hat starke Vorteile für zahlreiche Anwendungen. Zum Beispiel hat die Änderung des Oberflächenmusters von nano- und mikrostrukturierten, biofunktionalisierten Substraten einen groåen Einfluss auf das Adhäsionsvermögen lebender Zellen. Folglich macht die räumliche Kontrolle der Anordnung von Goldnanopartikeln durch Mikronanostrukturen sie zu besonders geeigneten Grenzflächen zur Kontrolle der Zelladhäsion im Mikro- und Nanometermaßstab. Die Herstellung der Mikronanostrukturen wurde durch die Verwendung von Photolithographie in Kombination mit **Block-Copolymer-Mizell-Nanolithographie (BCML)** möglich. Zunächst wurde dafür das mikrostrukturierte Substrat in einem aus zwei Schritten bestehenden photolithographischen Prozess

hergestellt. Anschließend wurden Goldnanopartikel mit Hilfe von BCML abgeschieden. Die Kombination der Selbstorganisation von Goldnanopartikeln in den mikrostrukturierten Substraten führt zu einer kontrollierten Verteilung der Goldnanopartikel in einer Mikronanostruktur. Auf diese Weise ist es möglich, unterschiedliche Partikelabstände auf benachbarten Mikro-Abschnitten desselben Substrates zu erzielen. Diese neuartige Strategie ist eine vielversprechende Methode um regelmäßige, metallische Nanopartikelmuster auf einer Vielzahl von unterschiedlichen Substraten zu erzeugen. Dies ist für alle Anwendungen relevant, die eine kontrollierte Verteilung von Nanopartikeln voraussetzen. Beispiele hierfür sind DNA Chips, Nanodrähte und optisch aktive Nanobeschichtungen.

Obwohl obiger Ansatz eine räumlichen Kontrolle der Zelladhäsion liefern kann, kann er nicht das dynamische Verhalten von Zellen *in vivo* nachbilden, da er auf einer statischen und unveränderlichen Grenzfläche beruht. Um diese Einschränkung zu überwinden stelle ich einen zweiten Ansatz vor, der die Zelladhäsion reversibel und dynamisch kontrolliert. Das reversible Schalten wird durch zwei unterschiedliche Azobenzolsorten umgesetzt. Hierfür werden lichtgesteuerte Azobenzol-Moleküle verwendet, die zwischen den *cis*- und *trans*-Isomeren geschaltet werden können. Die Azobenzole wurden durch Abscheiden auf einer Glasoberfläche immobilisiert und anschließend mit RGD (Arginin-Glycin-Asparaginsäure) biofunktionalisiert. Die Zwischenräume wurden mit einer biologisch inerten Monolage aus Polyethylenglykol (PEG) aufgefüllt. Die erste Azobenzolsorte moduliert die Zelladhäsion durch UV-Strahlung, welche das Schalten des thermisch stabilen *trans*-Isomers in die *cis*-Konfiguration auslöst. Diese Isomerisierung führt dazu, dass das RGD-Peptid in die nicht haftende PEG Umgebung eintaucht. Eine anschließende Belichtung mit sichtbarem Licht schaltet das Molekül in die *trans*- Konfiguration zurück, die das RGD erneut für Zellen zugänglich macht. Wie Studien mit dem Rasterkraftmikroskop belegen bietet diese Methode eine effektive Möglichkeit, um die Zelladhäsion schnell hin- und herzuschalten. Allerdings benötigt diese Methode zwei verschiedene Wellenlängen. Dieser Nachteil wird umgangen, indem eine andere Azobenzolsorte, ein sogenanntes **push-pull**-Azobenzol, verwendet wird. Dieses ermöglicht das dynamische, reversible Schalten der Zelladhäsion mit nur einer Wellenlänge. Dieser Ansatz stellt eine faszinierende, unkonventionelle Methode dar, um durch die Benutzung einer einzigen Wellenlänge des sichtbaren Spektrums die Oberfläche reversibel zwischen zwei Phasen zu schalten. Die erste Phase ist ein Zustand einer schnellen *trans*/*cis* Oszillation der **push-pull** Azobenzole bei Belichtung mit Licht der Wellenlänge 530 nm. Die zweite Phase beginnt sobald das Licht ausgeschaltet wird. Dann erfolgt keine Oszillation der **push-pull** Azobenzole und

der Ausgangszustand, die *trans*-Konfiguration, ist wieder hergestellt. Die Experimente zeigten, dass die Oszillation der Azobenzole die Zelladhäsionskräfte signifikant verstärkt. Ebenso konnte eine Erhöhung der Genexpression von Proteinen, die für die Bildung von Fokalkontakten wichtig sind, nachgewiesen werden. Die Ergebnisse dieser Studien gelten als Meilenstein in Bezug auf das Verständnis und die Regulierung des zellulären Mechanosensing durch molekular kontrollierte, mechanische Stimuli auf der zellulären und molekularen Ebene.

Die in dieser Arbeit erforschten Grenzflächen stellen neuartige Konzepte zur Kontrolle der Zelladhäsion vor. Sie ebnen den Weg für ein künftig besseres Verständnis von bislang unerforschten Eigenschaften der Zelladhäsion, ebenso wie für die Entwicklung von innovativen funktionellen Biomaterialien.

Contents

Chapter 1

Introduction

1.1 Biological background

1.1.1 Cell adhesion

A cell is the smallest living building block in living creatures. Their ability to assemble and reproduce allows for the formation of tissues that build up to create an organism[1]. One of the most crucial cellular activities that triggers numerous cell functions is cell adhesion. Generally, cell adhesion can be divided into two forms: Cell-cell and cell-extracellular matrix adhesion[2]. They are both highly complex processes that are involved in many activities such as cell motility, differentiation and apoptosis (programmed cell death). Cell adhesion mediates cell guidance as well as its anchorage to the appropriate location inside the body. Therefore, cellular adhesive interactions play a major role in the construction and maintenance of living organisms[2]. Cell adhesion is mediated by membrane-bound cell adhesion molecules (CAMs) such as integrins, cadherins and selectins[3,4]. These transmembrane proteins interact with their extracellular ligands through structural affinity, which is realized through a molecular recognition mechanism between the receptors and their ligands[5]. Individual bonds formed during proteinprotein interactions, e.g., Van der Waals interactions, hydrophobic interactions, hydrogen bonds, and electrostatic interactions, are several orders of magnitude weaker than covalent bonds and are continuously competing with thermal energy. However, the relative weakness of specific bonds opens many possibilities for cells to easily manipulate the strength of their adhesion dynamically[3]. The cell-cell and cell-extracellular matrix interaction points, so-called cell junctions, are mediated

via cell membrane receptors, which serve as signaling molecules that enable a cell to "communicate" with its surrounding[2].

1.1.2 Cell junctions

Cell junctions are specialized regions of connection that occur in all tissues between either two cells or a cell and its Extracellular Matrix (ECM). There are three classes of junctions: Occluding junctions, communicating junctions and anchoring junctions[2]. An occluding junction can be found in an epithelium, where two cells are sealed together and a strong barrier is formed through which even small molecules cannot leak from one side to the other. Communicating junctions facilitate chemical and electrical signal-transmitting between two interacting cell partners[2]. As for anchoring junctions, they provide a mechanical attachment of a cell (and its cytoskeleton) to neighboring cells or the ECM. They are commonly found in animal tissues, specifically those subjected to large mechanical stresses such as the heart muscle and skin epithelium[2]. There are two functionally different types of anchoring junctions. The first ones are adherens junctions and desmosomes that are responsible of holding cells together and are formed by transmembrane adhesion proteins that belong to the cadherin family. The second type of anchoring junctions are focal adhesions and hemidesmosomes that are responsible of binding cells to the extracellular matrix and are formed by transmembrane adhesion proteins that belong to the integrin family. From the intracellular side of the membrane, focal adhesions and adherens junctions serve as anchorage sites for actin filaments, while desmosomes and hemidesmosomes are the anchorage sites for intermediate filaments[2].

In general, cell-extracellular matrix adhesion plays a significant role in controlling cell shape and also inside-out signal transduction, i.e. transmission of regulatory signals through integrins between the cell's cytoplasm and the extracellular domain[6]. On the other hand, cell-cell adhesion is essential for the formation of distinct groups or sheets of cells during embryogenesis, thereby preventing and arresting cell movement[2]. Anchoring junctions consist of two adhesion proteins. The first protein, the so-called receptor, binds the extracellular domain to an extracellular ligand. The second protein provides the connection between the intracellular segment of the receptor and the cytoskeleton[1,2].

1.1.3 The integrin receptor - a cell adhesion molecule (CAM)

In general, there are five families of cell adhesion molecules: Cadherins, immunoglobulins, selectins, mucins and integrins[2]. Each of these adhesion molecules is responsible for a specific type of cellular interaction. Cadherins and immunoglobulins mediate homophilic cell-cell adhesion with the difference that only cadherin binding implies a linkage of the adhesion site to the cytoskeleton. Selectins also mediate cell-cell adhesion via binding to the carbohydrate chains of mucin-like CAMs in adjacent cells[7]. The CAM that plays a major role in mediating cell-extracellular matrix adhesion is the integrin.

Integrins are a family of non-covalently bound α and β heterodimeric transmembrane receptor proteins. These proteins mediate cell adhesion via binding extracellular adhesion molecules to the intracellular actin cytoskeleton. In general, there are 18 α and 8 β subunits known today in mammalian cells where combinations of both subunits together form 24 distinctive receptors with different ligand specificity and functions[8]. Fig. 1.1 shows the RGD (Arginine-Glycine-Aspartate) binding receptor subfamily in the integrin family.

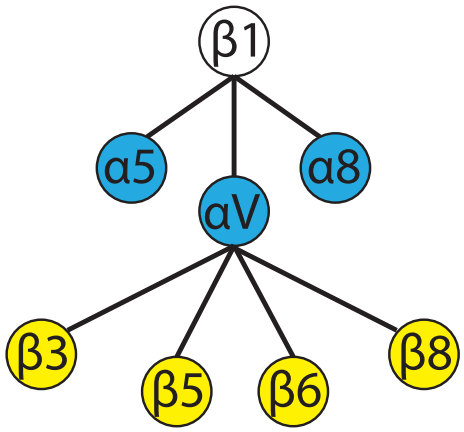

Figure 1.1: *The RGD binding receptor subfamily within the integrin family. Figure is modified from Hynes et al.*[8].

Integrins can vary between two conformational states: The low-affinity, non-activated and the high-affinity, activated state. Non-activated integrins have a v-shaped or bent structure with the headpiece close to the membrane. When integrins are activated, they change their structure through a switch-blade motion of the headpiece so that a binding site is exposed and made available for efficient interaction with the ligands (Fig. 1.2)[1].

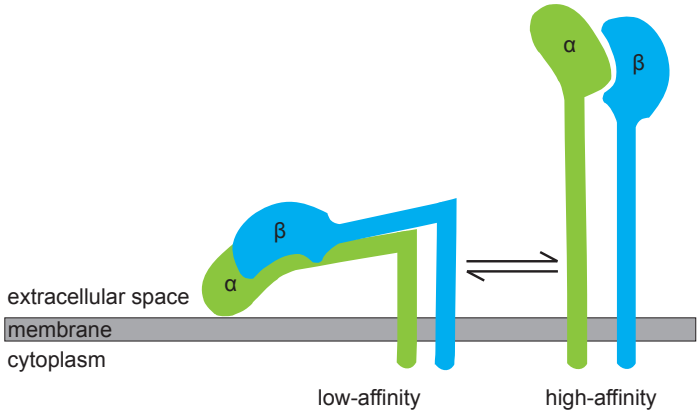

Figure 1.2: *A proposed mechanism for the activation of integrins. In the low-affinity state, i.e. inactive state, the integrin bends towards the membrane and both α and β subunits are adjacent to each other. When the integrin is in the high-affinity state, i.e. active state, the subunits separate and become available for interaction with ligands in the extracellular space. Figure is modified from Li et al.*[9].

In general, and when a sufficient number of ligands is available for the cell, activated integrins tend to form clusters at adhesion sites with increasing cell adhesion time. The integrin clustering at a cell surface induces a shift in the equilibrium between inactive-active states towards the active conformation. The integrin activity is mainly regulated by integrin interacting partners like cytosolic proteins, extracellular ligands and the cytoskeleton that affect the integrin's equilibrium binding between partner proteins and ligands[1]. The increase in the number of integrins within a cluster leads to the formation of large hierarchically assembled protein patches in the form of focal complexes, which subsequently mature into focal contacts, i.e. focal adhesions[7].
As mentioned above, cells are able to connect to the extracellular matrix via integrins that bind intracellularly to actin filaments. In a focal adhesion, the transmembrane integrin proteins bind to a protein component of the extracellular matrix from the extracellular domain side, while the intracellular domains bind to a patch of actin filaments. The latter binding is conceived via the intracellular anchor proteins such as talin, $\alpha-$actinin, filamin and vinculin (Fig. 1.3)[2].

1.2 Mechanics of the biomolecular bonds

Biological bonds are based on weak, non-covalent, interactions that enable them to rearrange quickly in response to external stimuli[10]. From a physical perspective, the easiest way to illustrate the energy landscape of a biological bond is a one-dimensional

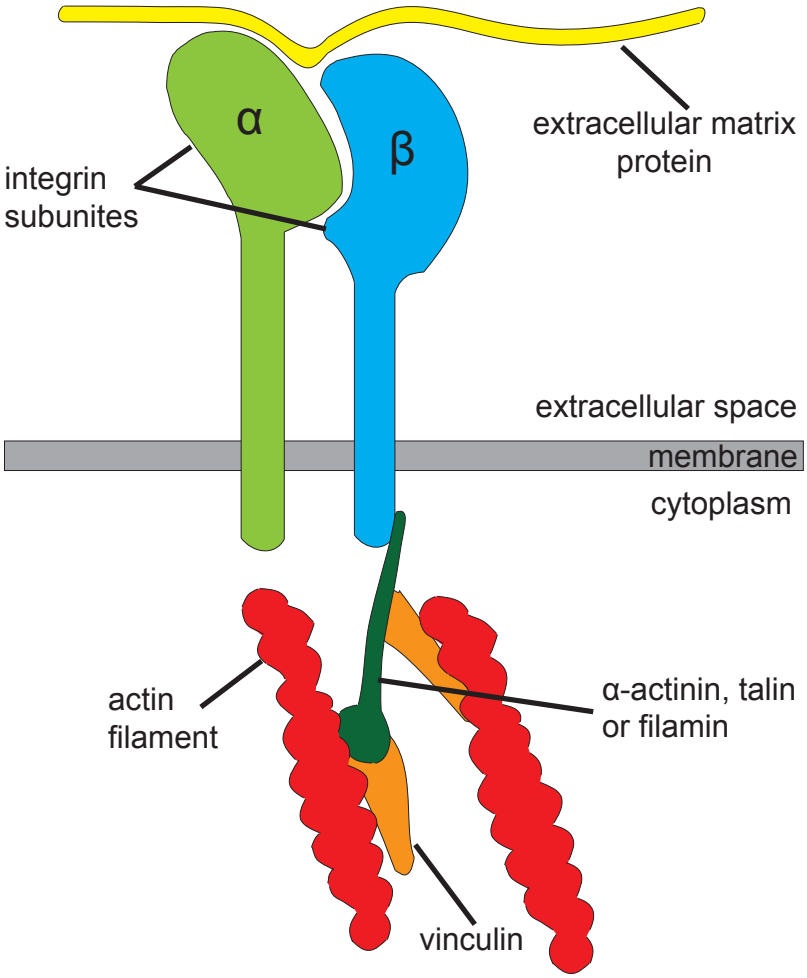

Figure 1.3: *An integrin binding enables a cell to connect to the extracellular matrix. On the extracellular domain side, the integrin proteins bind to a protein component of the extracellular matrix. On the intracellular domain side, the integrin binds to a patch of actin filaments via anchorage proteins such as talin, α−actinin, filamin and vinculin. Figure is modified from Alberts et al.*[2].

potential that consists of a bound state, an unbound state and a transition state barrier separating them (see section 1.2.1). Since biological systems function at physiological temperatures, biomolecular bonds have evolved to operate in the presence of thermally-driven fluctuations. Thus, bond-formation is constantly competing against the thermal energy available in the biological system that can overcome transition barriers between bound and unbound states at some point in time and hence leads to opening up the bond[10]. Although this implies that an organism should disintegrate over time, that is not happening due to physiological settings that favor rebinding, which in turn stabilizes molecular bonds.

1.2.1 Mechanically-assisted bond dissociation

Mathematical models have been developed to derive quantitative predictions about the survival of bonds under force. The most widely used method is to project a biological bond on a proposed energy landscape as promoted by Evans *et al.*[11] and derived from Kramers reaction rate theory[12]. In this method, the landscape of unbinding pathway projected onto the direction of applied force captures the essential properties of this system (Fig. 1.4)[13].

An external force applied onto molecular bonds lowers the potential energy barrier that stabilizes the bound state. This mechanically-assisted opening up of biomolecular bonds has been the point of research for many years both experimentally and theoretically. The main theoretical approach in this field is Kramers theory that explains thermally-assisted escape over a transition barrier from basic thermodynamic principles[14,15]. Experimental approaches to evaluate biomolecular bonds were first carried out using Atomic Force Microscopy (AFM) experiments performed by the Gaub group in 1994, which opened up the field of single-molecule force spectroscopy. They have reported on the mechanically-induced unbinding of single biotin-streptavidin bonds that exhibited a binding strength of 140 pN[16]. In 1997, Evans and Ritchie illustrated that the binding strength appears to be rather a dynamic than a static quantity and that it depends on the loading rate at which the bond is investigated[14]. It has been concluded that the faster the pulling rate, the less time thermal fluctuations have to contribute during unbinding, which in turn leads to a larger binding strength.

Based on the framework of Kramers theory, Evans and Ritchie presented bond rupture as thermally activated escape over a transition state barrier[14]. In the absence of force, the rate of barrier crossing (k_0) depends on the barrier height (E_b) as shown in the following equation

$$k_0 = \frac{1}{t_D} \cdot e^{-E_b/k_BT} \tag{1.1}$$

where k_BT is the Boltzmann constant multiplied with the temperature, or the thermal energy, and t_D is attempt time[10,13]. According to Kramers theory, an applied constant force (F) tilts the energy landscape with an additional term $-F \cdot x$, which

in turn lowers the transition state barrier by $-F \cdot x_b$ as follows

$$\begin{aligned} k(t) &= \frac{1}{t_D} \cdot e^{-(E_b - F(t)\cdot x_b)/k_B T} \\ k(t) &= k_0 \cdot e^{F(t)\cdot x_b / k_B T} \end{aligned} \tag{1.2}$$

where x_b is the distance between the bound state and the barrier along the dissociation path (linear reaction coordinate)[17]. Considering that $F_b = k_B T / x_b$, the transition rate under an external applied force will be expressed by the famous Bell equation[18]

$$k(t) = k_0 \cdot e^{F(t)/F_b} \tag{1.3}$$

Thus, the unbinding rate constant increases exponentially with force. This effect can be illustrated by adding the energy of the external force to the bond energy (Fig. 1.4)[11,19].

The transition state is assumed to be longer in the direction of force compared to the bound state, that is $x_b > 0$ as shown in Fig. 1.4. Hence, the energy barrier is lowered by the force which yields an increase in the unbinding rate, explaining why many bonds will be slip bonds. This bond landscape anticipates that there will be a single rate constant $k(t)$ at each force when bonds encounter an external force[13]. The fraction of bonds that survives with a single rate constant decreases exponentially with time. Due to the increase in decay rate with force, the mean lifetime will correspondingly decrease exponentially with increasing external force (Fig. 1.4)[13].

Although the transition rate is an important parameter to express the kinetics of bond rupture, the quantity that is typically measured in experimental settings such as force spectroscopy is the binding strength, i.e. unbinding force, which is the force needed to rupture a bond. However, as bond rupture is a stochastic process, there will be a distribution of unbinding forces rather than a single specific force value. The width of this force distribution is governed by the force scale factor (F_b). Thus, in the framework of Kramers theory for a single transition state barrier, Evans[20] concluded that the most probable rupture (unbinding) force (F^*) scales linearly with the logarithm of loading rate (r) as shown in the following equation

$$F^* = F_b \cdot ln \frac{r}{k_0 F_b}, \tag{1.4}$$

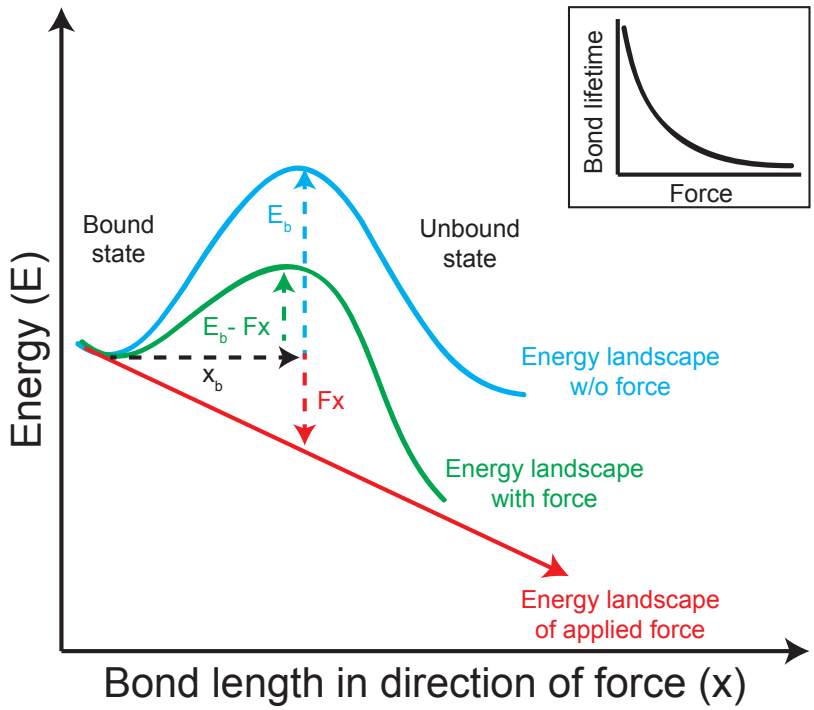

Figure 1.4: *Slip bonds. The projection of a one-dimensional energy landscape on the direction of an externally applied force. The dotted lines indicate the changes in energy (E) and length (x) that the bond experience before reaching the transition state. The inset demonstrates the average bond lifetimes as a function of the applied force levels. Figure is modified from Thomas et al.*[13].

where the nominal loading rate ($r = dF/dt$) in AFM is kv (spring constant times piezo retraction speed). In 1999, Merkel *et al.* have shown experimentally using dynamic force spectroscopy (increasing pulling forces) the linear dependence of unbinding force on loading rate with AFM experiments on biotin-streptavidin and biotin-avidin bonds (the general results are shown in Fig. 1.5)[21]. The measurements were performed over a loading rate range of six orders of magnitude, revealing unbinding strengths varying from 5 to 170 pN.

1.2.2 Mechanically-assisted bond strengthening

Biological bonds that mediate cell anchorage are *in vivo* regularly subjected to different mechanical forces and their response comes out through various means[13]. It is generally accepted and demonstrated that biological bonds slip apart (become shorter lived) under a tensile force[22], which led to the term "slip bonds". However, in 1988 the term "catch bonds" was introduced as a result of a hypothesis suggesting that some bonds catch (become longer lived) under tensile force[22]. Catch bonds provide

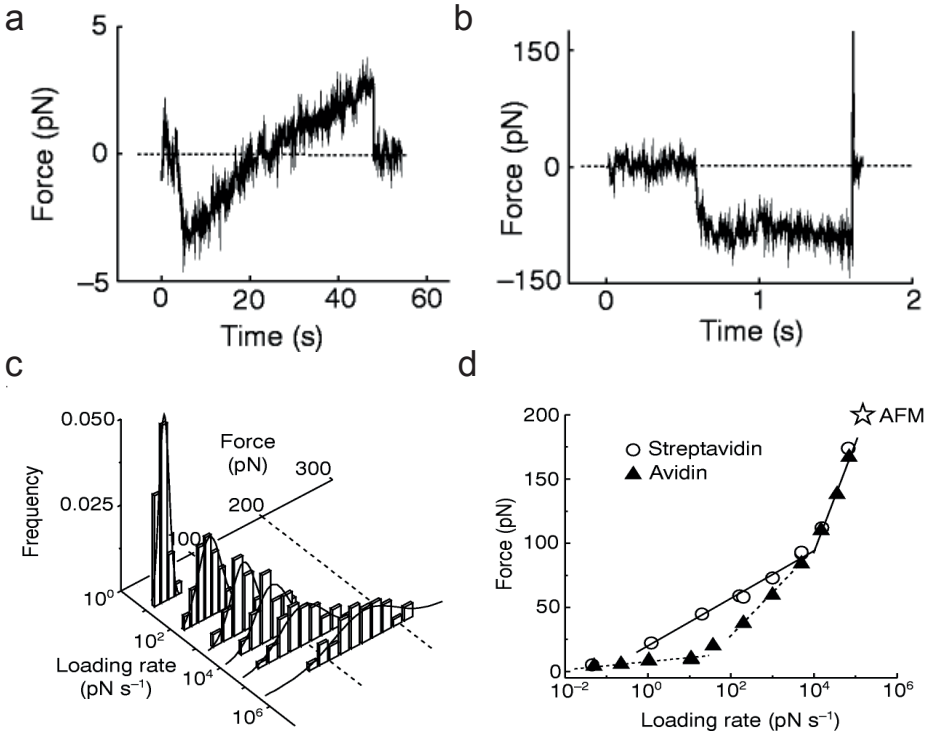

Figure 1.5: *Dynamic force spectroscopy conducted on biotin-streptavidin and biotin-avidin bonds using atomic force spectroscopy. (a) Long bond lifetime of 24 s and small bond strength of 3 pN resulted from low loading rates. (b) Short lifetime of 0.003 s and large bond strength of 170 nN resulted from high loading rates. (c) Unbinding force histograms for varying loading rates over six orders of magnitude. (d) The increase in unbinding strength with increasing loading rate. The dynamic loading also shows the different transition state barriers for both biotin-streptavidin and biotin-avidin bonds. Reprinted by permission from Macmillan Publishers Ltd: Nature*[21]*, copyright 1999.*

means to cells that help stabilizing their adhesion exactly at the time they need it most - when bonds are otherwise pulled apart by forces. Such responsive adaptation is commonly seen in proteins even though the source of regulation is biochemical, e.g. another protein, rather than mechanical. Nevertheless, a number of proteins and biological mechanisms can be activated mechanically, and the principles of both biochemical and mechanical regulations can be applied on catch bonds[13].

The behavior of catch bonds has only been recently demonstrated at the single-molecule level through stretching individual bonds using atomic force microscopy. In 2003, Marshall *et al.* showed that the dissociation of individual catch bonds is governed by a single rate constant at each level of force applied to the bonds. The bond dissociation was shown to decrease with the force level which led to an increase in the average bond lifetime with force. However, when the applied force exceeded a certain

critical value, this trend was reversed and these bonds were overpowered like any other adhesive interaction subjected to sufficient force. Therefore, catch bonds, with this biphasic response to force, exhibit longer lifetime at an intermediate force level termed the critical force[13,23].

Several conceptual models have been proposed to explain how tensile mechanical forces might strengthen bonds. The first suggested model is a hook or a harpoon[24] where both ends catch each other if tensile force is applied, when otherwise easily unbind if not pulled apart (Fig. 1.6 a). The other model resembles a Chinese finger trap which has a meshed cylindrical shape that narrows when elongated and thus grips more tightly due to the applied tensile force (Fig. 1.6 b)[13].

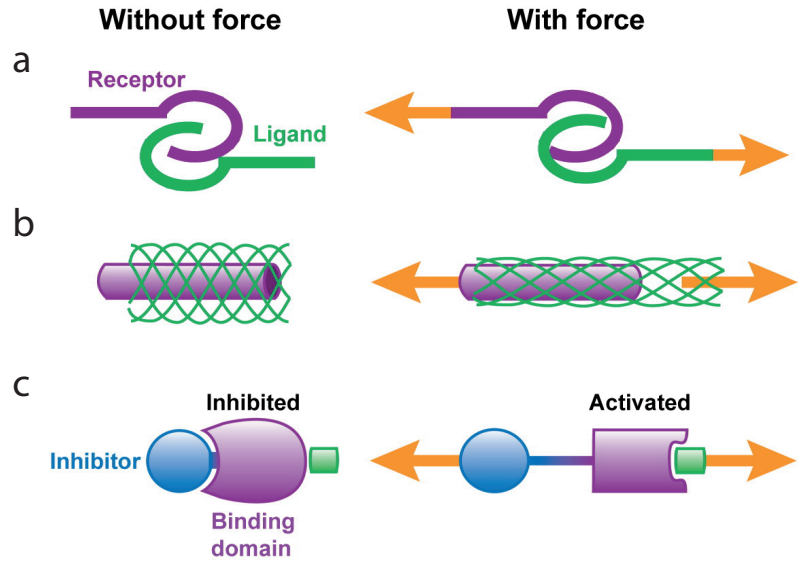

Figure 1.6: *Selected conceptual models for demonstrating catch bonds. (a) The hook model suggests that for the ligand and receptor to unbind, they must come towards each other. (b) A Chinese finger trap model. (c) The allosteric model presumes that the applied force pulls away an allosteric inhibitor that causes a certain conformational change to a stronger-binding state. Reprinted by permission from Annual Reviews: Annual Review of Biophysics[13], copyright 2008.*

The aforementioned models are based on mechanical concepts that are more familiar to physicists. Biologists on the other hand consider concepts based on protein regulation to explain catch bond behavior. Most proteins change their structure and thus, their function due to an external stimuli. One of the most common means that is accepted in a large number of proteins as a functional regulation mechanism is allostery. Allostery is the modulation of a protein's affinity or activity caused by the binding of a molecule to an additional site other than the protein's active site. Therefore, it has been proposed that a mechanical force could act on an allosteric site of a

catch bond rather than directly on the ligand-binding pocket[25]. Fig. 1.6 c illustrates an example of a ligand-binding domain interacting with another domain that acts as an allosteric inhibitor. A mechanical force could remove the inhibitor from the regulatory site of the ligand-binding pocket, favoring a high-affinity over a low-affinity state[13].

When the transition state is shorter in length than the bound state, i.e. $x_b < 0$, an external force will increase the energy barrier and the bond is then a catch bond[22–24]. In this case, there will be a second classical slip unbinding pathway ($x_b > 0$) where the bond then has two pathways to unbind (Fig. 1.7).

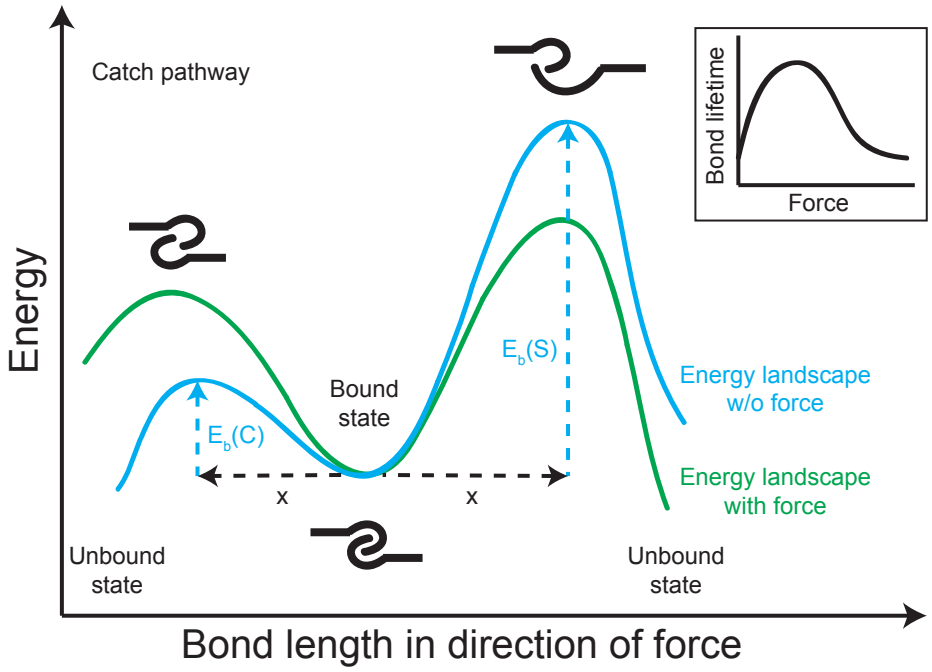

Figure 1.7: *Catch bonds. Projection of a one-dimensional energy landscape on the direction of force as shown in Fig. 1.4, with an additional catch pathway. The cartoon figures demonstrate the bound and transition states based on the hook concept of catch bonds from Fig. 1.6. The inset demonstrates the average bond lifetimes as a function of the applied force. Figure is modified from Thomas et al.[13].*

A bond is considered a catch bond when the catch pathway dominates at low force[13]. This condition is met when the catch pathway has a faster rate constant than the slip pathway, with $E_b(\mathrm{C}) < E_b(\mathrm{S})$ where S and C denote slip and catch pathways as displayed in Fig. 1.7[23]. There are at least two concepts that describe this model. The first concept is based on the assumption that the bond is shaped like a hook or a harpoon. To "unhook" the bond, the catch pathway requires bridging the ends together while the slip pathway simulates the case of bending an elastic hook forcibly. The alternative concept presumes that the receptor undergoes an allosteric or ligand-

induced switch to an extended active conformation as shown by the cartoon of the bound state in Fig. 1.7[13]. The transition in the catch pathway would be structural reversion to the compact inactive conformation that lets go of the ligand. The slip pathway on the other hand would be a direct unbinding of the ligand from the active state[13]. Mathematical models have been developed to predict the lifetime of a catch bond under applied forces. When considering the two force-dependent transition rate constants $K_C(t)$ and $K_S(t)$ for the two pathways defined in analogy to equations 1.1 and 1.2, the bond has a single transition rate at each force, which can be expressed as $k(t) = K_C(t) + K_S(t)$. This single transition rate will be lowered first with force then increase, therefore the bond mean lifetime, 1/k(t), will show a biphasic behavior in response to force (inset in Fig. 1.7).

1.3 Cell-response to adhesion-mediated mechanical forces

1.3.1 Mechanosensing

Cell behavior is affected by numerous signals that a cell can be exposed to, some of which, for instance, can lead to pathological conditions[26]. The ability to understand and regulate these inputs is a vital aspect in tissue engineering and disease treatment. Recently, there has been a lot of focus on studying the influence of mechanical signals on cellular growth, migration and differentiation. All these studies are considered part of the growing research field of mechanosensing. Understanding the mechanisms of mechanosensing opens up potentials for developing novel therapeutic interventions for diseases such as cancer and also enables crossing of barriers in the field of tissue engineering[26].

The complex interaction between a cell and its environment is a strong regulating factor of cellular behavior. Although research has mostly been focused on chemical factors, recent works provided increasing concrete evidences that adhesion-regulated mechanical forces can play an equally significant role[26]. Mechanical forces are either translated into direct interactions with intracellular components[27] or, more likely, transform into intracellular chemical signals in areas that are adjacent to the plasma membrane where adhesion takes place[26]. This indirect cellular interaction with an applied mechanical force can also lead to changes in gene expression[28,29].

The extracellular signals can take a number of forms such as rigidity[30,31], shape[32,33] and topography[34]. It has been illustrated that culturing fibroblasts on soft substrates lead to apoptosis while solid substrates enhanced cell growth[35]. Additionally, substrate rigidity has been shown to determine the differentiation of mesenchymal stem cells *in vitro*[36]. It has also been demonstrated that cells appear to exhibit active growth when allowed to spread on substrates without constraints compared to ones that undergo apoptosis when spreading is hindered[33]. This provides evidence to the vital role of shape and geometry, which exhibit similar effects on cells as mechanical forces.

1.3.2 Mechanical force-sensing mechanisms

Mechanical forces applied on cells trigger transmembrane signaling[26]. This signaling can be initiated due to inducing the entry of calcium ions through stretch-activated channels[37–40] and/or due to prompting structural changes at adhesion sites[26]. A lot of attention has been drawn to focal adhesions in adherent cells because they provide the direct mechanical linkage between the cells' cytoskeleton and the extracellular matrix[41]. Additionally, focal adhesions are the sites where crucial signal transduction enzymes such as SRC kinase (a family of tyrosine kinases that play a key role in regulating cell adhesion, growth, differentiation and apoptosis[42]) and Focal Adhesion Kinase[43] (an important signaling component that has an effect on the cellular cytoskeleton and the structure of cell adhesion sites and thus can regulate cell motility[44]) are concentrated.

Cells respond to mechanical forces by activating small GTPase (a family of enzymes involved in regulating a wide variety of cellular activities such as cellular growth and differentiation) and RhoA (a small GTPase protein that plays a role in regulating the cellular cytoskeleton through actin fiber formation), in addition to increasing the size of focal adhesions and strengthening intracellular contractility and traction forces[45,46].

One of the crucial components of focal adhesions are integrins that have been hypothesized to be mechanosensors[47–49]. Mechanical forces have been proven to enhance integrin clustering, ECM binding and the recruitment of focal adhesion proteins[45,50,51]. Hence, it is seemingly evident that mechanosensing involves integrin activation as well as the resulting concentration of focal adhesion kinase and SRC[52,53]. Another potential mechanism suggests that these signaling molecules have an inherent mechanosensitivity. This theory proposes that mechanical forces may promote direct conformational changes as is the case with focal adhesion proteins, e.g. vinculin[54]. Furthermore, the

theory also suggests that mechanical inputs lead to exposing autoregulated catalytic domains, shielded substrate domains and/or cryptic binding sites of scaffold proteins (Fig. 1.8)[26].

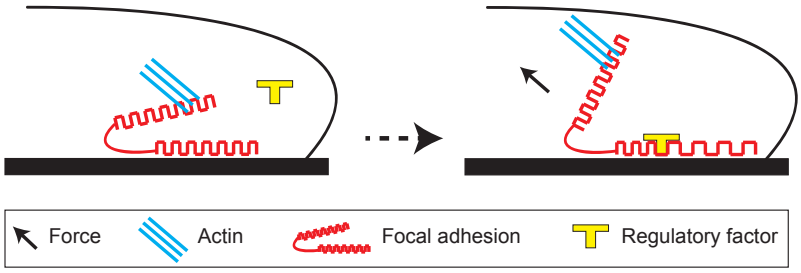

Figure 1.8: *A conceptual model for signal transduction based on force-triggered conformational changes. Forces induced by actin cytoskeleton results in protein unfolding, which leads to the exposure of binding sites to regulatory factors. Figure is modified from Rape et al.*[26].

Force-mediated structural changes take place on both intra- and intermolecular levels[55]. The actin filaments associated with focal adhesions illustrate force-driven assembly and retrograde flux. Some focal adhesion components show selective association to actin filaments which results in differential transport and relative shear movements of these components (Fig. 1.9)[26]. Therefore, the interaction among the proteins that are associated with focal adhesions is governed by their affinity for integrin/membrane components versus the actin cytoskeleton.

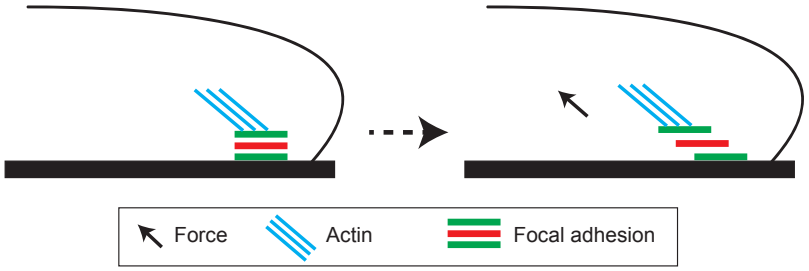

Figure 1.9: *A conceptual model for signal transduction based on force-triggered protein shear movements. Forces induced by the actin cytoskeleton results in lateral shear and relative movements of focal adhesion proteins. Such movements can modify protein-protein interactions and influence enzymatic activities within focal adhesion. Figure is modified from Rape et al.*[26].

Focal adhesion response to forces can be expressed in several forms. Riveline *et al.* showed that a force applied locally using a micropipette on an integrin containing focal adhesion leads to a growth in contact size[45,56]. The applied mechanical force causes a change in cell contractility, which in turn is required to generate tension applied

by the cell to focal complexes. This tension is a significant factor that assists focal complexes maturing into focal contacts[45]. It has been elucidated that an increase of cell contractility yields a growth in focal contact size, whereas blocking cell contractility resulted in a rapid disassembly of focal adhesions[45]. These studies demonstrate that both focal complexes and focal contacts respond to applied forces and act as miniature mechanosensors through which cells react to their microenvironment.

1.3.3 Implications in biomedical engineering and disease treatment

Despite the limited understanding of the mechanism of mechanosensing, tissue engineers and pathologists agree on the profound role of numerous adhesion-mediated signals and their significant implications of cellular responses in disease treatment and regenerative medicine[26,57]. Mechanosensing may offer a unique approach and a new dimension to find effective treatments for cancer. Cancer therapies are often unsuccessful due to uncontrolled cell growth and migration, both of which are modulated by chemicals as well as adhesion-mediated signals. One of the main aspects that contribute to the disease phenotype of cancer is the loss of anchorage dependence. Most normal, non-hematopoietic cells adhere strongly to a surface in order to survive[34,58,59]. The loss of anchorage dependence in cancer cells allows them to grow and proliferate in the absence of adhesion to the ECM proteins. This anchorage independence is believed to be closely correlated with tumorigenicity in animals[60]. This ability of cancer cells reflects the tendency of tumor cells to survive and grow in inappropriate locations *in vivo* as well as floating through the bloodstream towards distant sites elsewhere in the body. The other important aspect that contributes to the cancer disease phenotype is the increase in stiffness in various tumors in comparison to their normal counterpart or their surrounding tissues[61,62]. It has been realized that increased ECM stiffness leads to tumorigenesis in an integrin and cytoskeleton contractility dependent manner[63,64]. Pathologists suggest that an increase in stiffness leads to durotaxis (cells migration towards areas of greater stiffness[65]), which may cause tumor cells to migrate away from home tissue and consequently leads to growing of blood vessels into the tumor to provide nutrients. Altogether, it is clear that understanding mechanotransduction pathways offers state-of-the-art approaches for cancer therapy.

The ongoing research on mechanobiology will also facilitate controlled engineering of man-made tissues that have great potentials to be employed in the field of regenerative

medicine. Stem cells researchers have realized that in order to guide cells toward desirable differentiation pathways, they will have to consider not only the chemical environment but also physical parameters such as stiffness and topography of the surrounding materials[26]. To successfully engineer complex tissues, the mechanical and topographical environment need to be regulated at a matching complexity.

1.4 Nano-biomaterials

Nanoscience and nanotechnology are broad fields which cover wide areas of research ranging from electronics and sensors to medicine and healthcare. In all these fields, the functionality is defined by physical or chemical properties, which are influenced by the choice of material, shape and the surrounding matrix[66–69]. One of the most essential factors involved in the fabrication of functional nanostructures is the ability for a designated placement of nanometer-sized objects in periodic and aperiodic arrangments on substrates with different composition and electrical properties[70]. In general, the two major strategies that scientists follow to answer demands in nanosciences are the top-down and bottom-up approaches. Photolithography and electron-beam lithography are the most routinely employed techniques, which are widely used in microfabrication and chip production. Recurring improvements in these techniques, such as the use of shorter wavelenghts, e.g. deep UV or X-ray, as well as the adjustment of resist material have provided a wide range of state-of-the-art lithographic capabilities for sophisticated patterning of surfaces. Owing to those modern techniques, patterns as small as 50 nm are feasible using photolithography. Numerous forms of such micro- and nanostructured substrates have been employed in biological research[71,72]. In this section, I present powerful tools for fabricating structured substrates that can be used as platforms for conducting specific cell adhesion studies.

1.4.1 Surface structuring

Metallic nanoparticles have been thoroughly investigated in recent years due to the intriguing electronic properties imposed by their dimensions[73,74]. Captivating ideas and perspectives have been established in the development of novel electronic devices[75] and electro-optical applications[76,77]. A plethora of techniques have been developed to fabricate nanostructured surfaces. The most widely used state of the art tools are Electron Beam Nanolithography (EBL), Dip-Pen Nanolithography (DPN) and

Block-Copolymer Micelle Nanolithography (BCML). EBL is a specialized fabrication technique for sub-50-nm patterns. The working principle of EBL is relatively similar to optical lithography. It is based on a focused electron beam that is used to expose across a substrate coated with an electron-sensitive resist whose solubility changes according to the energy deposited by the electron beam[78]. The exposed areas, or the unexposed areas depending on the resist properties, are removed through a developing process. Then, a layer of the desired material is deposited on the substrate followed by stripping off the remaining resist, which leaves patterns of the deposited material only on the pre-developed areas. However, the major drawback of electron beam lithography is that it is a slow and a very expensive fabrication method. On the other hand, DPN is a direct-writing fabrication method based on an (AFM) that allows precise surface nanopatterning of various materials on different surfaces. In this technique, a tip of an AFM cantilever is employed to transfer molecules of an ink solution onto a substrate. The tip is first coated by dipping it into the ink that is required to be deposited. Next, those molecules are delivered onto the substrate through a solvent meniscus that is created between the cantilever tip and the surface when both come close to each other[79,80]. However, despite being an attractive method for accurate structuring of organic and inorganic nanomolecules, DPN has a critical disadvantage represented by the low throughput. The speed at which patterning takes place is limited by tip movement that needs to be slow enough to permit a consistent ink delivery onto the substrate.

While both electron beam and dip-pen nanolithography are complicated and extremely time-consuming, block-copolymer micelle nanolithography offers simple and straightforward fabrication of micro- and nanostructures. Driven by self-assembly, this powerful surface patterning method is superior to other techniques in delivering highly-complex structures on large areas of the substrate with high-throughout rates at low costs.

In this work, BCML was chosen as a fabrication method to produce novel micro-nanostructured substrates which will be presented in Chapter 2. BCML will be discussed in more detail in the next section.

1.4.2 Block-Copolymer Micelle Nanolithography (BCML)

Block-Copolymer Micelle Nanolithography is a versatile and widely used surface-structuring tool for designing both periodic and aperiodic nanoparticle arrays as well

as other complex patterns[81–83]. Substrates decorated with such structures exhibit promising potentials in numerous fields of research such as optical[84] and cell biology[85]. In this section, I introduce the working principles and all steps comprised in a BCML technique.

Micelle formation

In BCML, block copolymers that consist of two polymers with different polarities, most commonly polystyrene (PS) and poly-2-vinylpyridine (P2VP), are dissolved in a solvent. Above the critical micelle concentration, these block copolymers arrange into spherical micelles that can be loaded with a metallic precursor[81]. Other block copolymers can be used to fabricate patterns with various shapes such as ring-like, rod-like as well as cylindrical features[82,83].

The amphiphilic diblock copolymers used in this work consist of a non-polar polystyrene (Block A) and a polar poly-2-vinylpyridine (Block B) (Fig. 1.10).

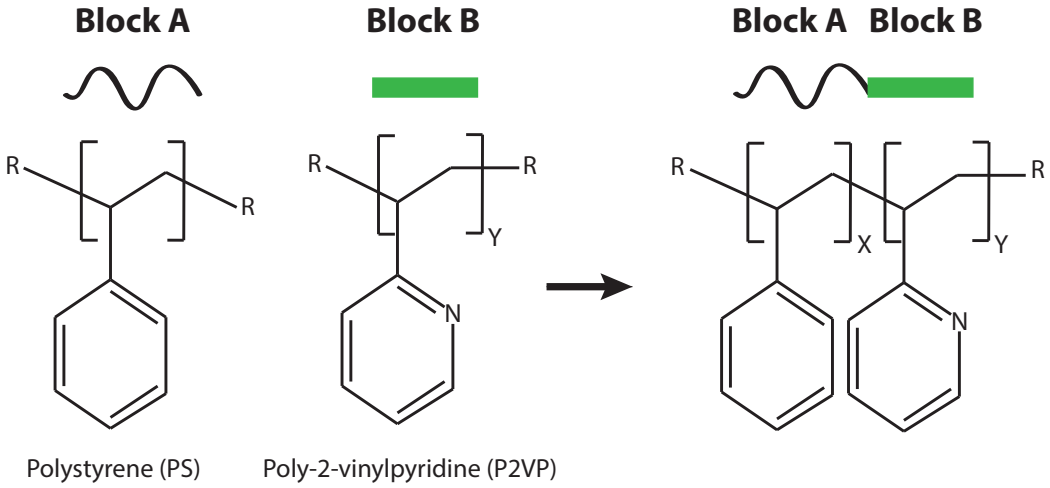

Figure 1.10: *The chemical structure of the two constituent polymers, polystyrene and poly-2-vinylpyridine, forming the diblock copolymer.*

Each chain holds a specific amount of monomer units, which can vary in length and ratio. The polymer contains X units of styrene and Y units of 2-vinylpyridine PS(X)-b-P2VP(Y). Block copolymers associate into uniform micelles when dissolved in specific solvents. The soluble block creates a shell around the insoluble block to protect it from energetically unfavorable interactions with the solvent[86]. In this thesis, polystyrene-block-poly-2-vinylpyridine is dissolved in a non-polar solvent (toluene or O-xylene) where micelles with a hydrophobic (PS) shell and a hydrophilic (P2VP) core

are formed.

Micellization, i.e. micellar formation, is dominated by two opposing effects: The first is the selective solubility as well as the incompatibility of the two blocks that induce association of the insoluble blocks of the copolymer. The second effect is the steric hindrance that restricts unlimited growth of micelles[87]. The micelle size is determined by the aggregation number, which is regulated by the molecular weight of the diblock copolymers as well as the interaction parameter between the polymers and the solvents on one hand and between the polar and non-polar polymer blocks on the other hand. The association of micelles has been described in a number of models in previous works[70,87,88].

The concentration (C) of block copolymers in the solvent where the spontaneous micelle association is initiated is called Critical Micelle Concentration (CMC) (Fig. 1.11)[89]. The CMC for each polymer is controlled by the used solvent, the temperature as well as the chemical structure and the behavior of each block of the copolymer.

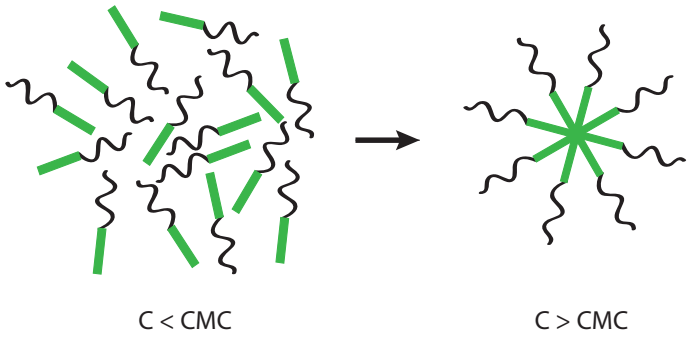

Figure 1.11: *A schematic representation of micelle formation, which initiates as the dissolved diblock copolymer reaches the critical micelle concentration.*

Micelles with uniform sizes can be formed using monodisperse block copolymers. Increasing the dispersity of the block copolymer will yield a wide range of micelle sizes. Due to polydispersity of all synthesized block copolymers, polydisperse and polyform micelles are inevitably obtained.

Micelles as nanoreactors

The hydrophilic core of the micelles can be loaded with various inorganic compounds like $HAuCl_4$, H_2PtCl_6, $ZnCl_2$ and other inorganic acids and salts through protonating the pyridine units. The chemical structure of the metal precursor determines the

nature of interaction with the polar core where such interactions vary from complexation to acid-base reactions. The loading of micelles with inorganic salts enhances the incompatibility of the polar core against the solvent and turns polyform micelles into spherical ones[90,91]. In this work, hydrogen tetrachloroaurate(III) $[HAuCl_4]$ is used as a metal precursor to load polystyrene-block-poly-2-vinylpyridine in order to create gold loaded micelles (Fig. 1.12).

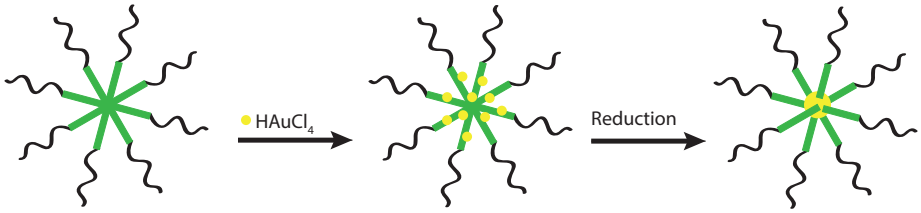

Figure 1.12: *Schematic illustration of nanoparticle formation inside block copolymer micelles. The metal precursor is added to the micelle solution. As the precursor dissolves, $[AuCl]^-$ ions embed within the micelles cores, and eventually reduce to a single gold particle.*

As the precursor dissolves in toluene or O-xylene, it protonates the weak pyridinium base in the polar core and thus the chloroaurate counterions $[AuCl]^-$ are embedded within the core of the micelle and eventually reduce to a single gold particle (Fig. 1.13)[70]. The particle size is determined by the molecular weight of the used copolymers as well as the amount of metal precursor added to the micellar solution[92].

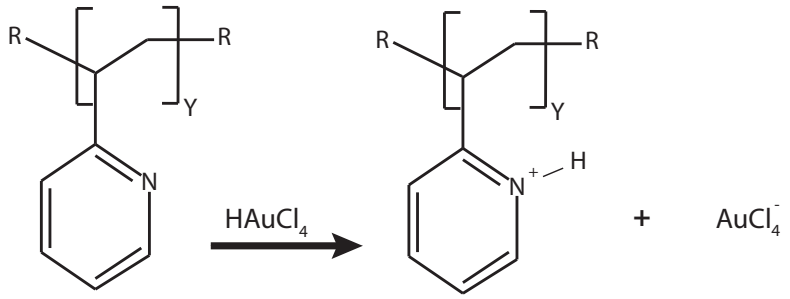

Figure 1.13: *The protonation (neutralization) reaction of vinylpyridine by $[HAuCl_4]$, which takes place in the micelle core. Figure is modified from Glass et al.*[70].

Substrate coating

Spreading of the micelle solution on substrates to obtain a monolayer of gold-loaded micelles has been successfully achieved using dip- and spin coating processes. In order

to simply demonstrate the process of micelle monolayer formation on a substrate, the dip coating technique will be addressed in this chapter.

Dip coating was employed for the first time by Dimitrov *et al.*[93]. In this method, a substrate is immersed in a suspension at a certain speed and for a specific period of time before it is withdrawn at a controlled retraction rate. Dimitrov had shown the ability to generate well-ordered quasi-hexagonal layers of polystyrene beads simply through dipping a substrate in an aqueous solution that contains those beads. Generating regular particle monolayers requires a substrate that allows dense and ordered pattern formation through particle mobility during the film drying period[1]. The formation of a particle monolayer can be described as a two-phase process: (1) Nucleus formation that is dominated by lateral capillary forces appearing between particles confined in a liquid layer; (2) Crystal growth through convective particle flux caused by solvent evaporation from the previously ordered array (Fig. 1.14)[1,94,95]. The lateral capillary forces are discussed in the following section.

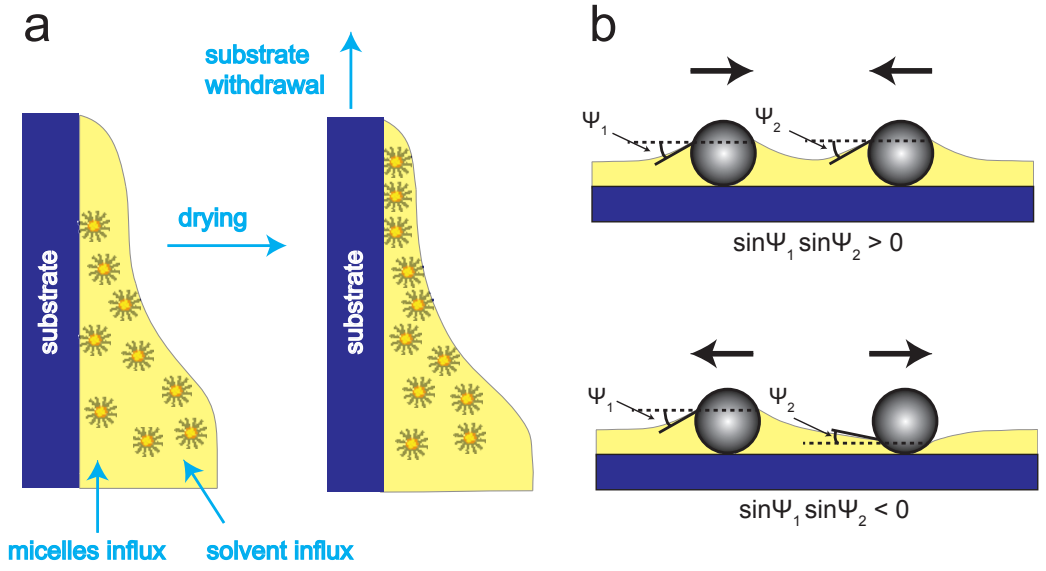

Figure 1.14: *Substrate coating with gold-loaded micelles in a BCML experiment. (a) Micelle layer formation mechanism via a dip coating process. The quasi-hexagonal arrangement of micelles takes place as the solvent dries out. (b) Schematic illustration of immersion forces for partially-immersed particles in liquid. Immersion forces attract particles towards each other when* $sin\Psi_1 sin\Psi_2 > 0$ *and repel them when* $sin\Psi_1 sin\Psi_2 < 0$*, where* Ψ_1 *and* Ψ_2 *are the meniscus slope angles at the two contact lines.*

The coating process yields a substrate covered with loaded micelles that have been self-assembled into quasi-hexagonal patterns. Then, the micellar polymer shell is removed by plasma treatment, which leaves quasi-hexagonally ordered arrays of metal

nanoparticles on the surface[96]. The lateral spacing between the nanoparticles can be varied by controlling the molecular weight of the diblock copolymers, the polymer concentration, and the coating speed during deposition of the micelle solution[97]. For example, increasing the rotational speed during spin coating reduces the thickness of the micelle-containing liquid film on the surface and results in a lower density of packed micelles, which leads to larger interparticle spacing as discussed in section 2.2.

Capillary-driven self assembly

Experimental results have shown that floating particles on a fluid interface attract each other[98]. This phenomenon has been observed and employed in a number of extraction and separation processes[99,100]. Nicolson had shown that the formation of these lateral capillary forces is attributed to the deformation of the interface caused by particle weight and buoyancy force[101]. The greater the interfacial deformation generated by the particles, the stronger the capillary interaction between them. This attractive force between two floating particles appears because the liquid meniscus deforms in such a way that the gravitational potential energy (the potential energy required to elevate an object against the earth's gravity) of the two particles is lowered when they come closer to each other. Thus, the origin of this attractive force is particle weight[98,101]. However, despite the insignificant weight of small colloidal particles and their inability to create any surface deformation, these particles show attraction and form ordered two-dimensional arrays when confined in liquid films (instead of being freely floating). Due to their confinement in the liquid film, these particles generate interfacial deformation. Such deformations are resulting from the wetting properties of particle surfaces induced by the thermodynamic necessity of having the particle surface meeting the liquid interface at a certain angle - the contact angle[98]. Such wetting-driven deformations also promote lateral capillary forces[102].

A number of studies have been conducted to investigate lateral capillary forces in floating particles[101,103,104]. However, a theoretical study of capillary forces between two partially immersed (confined) spheres was first carried out by Kralchevsky *et al.*[102]. Kralchevsky presented a general expression that is valid for both floating and confined particles to describe the interaction energy. The interaction energy combines several energy contributions like gravitational, particle wetting and also the energy that arises from an increase in meniscus area resulting from deformation caused by particles[98,102]. It was observed that capillary forces obey a two-dimensional version of the Coulomb law of electricity. Based on this analogy, "capillary charges" of the particles have been

presented. Thus, depending on whether the capillary charges have similar or opposite signs, the capillary force will be accordingly attractive or repulsive[98].

In 1993, Paunov *et al.* had described the physical nature of lateral capillary forces and analyzed the force magnitude for both floating and confined particles[105]. It has been established that in the case of floating particles, the energy of capillary interaction becomes negligible (lower than the thermal energy) for particles with diameters smaller than 5 - 10 μm. However, when the particles are partially immersed into a liquid film rather than freely floating, the energy of capillary interaction is larger (for the same particle size) and can also be much higher than the thermal energy even for nanometer-size particles[98,105]. The former type of capillary interaction is called "floatation forces" and the latter is "immersion forces"[106]. Despite the similar dependency on interparticle separation exhibited by the two forces, they show very different dependencies on particle radius and the liquid's surface tension.

Immersion forces, which are the dominant capillary effect in certain BCML coating situations, can be either attractive or repulsive depending on the signs of the meniscus slope angles Ψ_1 and Ψ_2 at the two contact lines. The sign of the meniscus slope determines the "capillary charge" of the particle (Q_i) according to the following formula

$$Q_i = r_i \cdot sin\Psi_i \tag{1.5}$$

where (r_i) represents the radii of the two contact lines (r_1) and (r_2). Thus, the immersion force is attractive between the two "capillary charges" when $sin\Psi_1 sin\Psi_2 > 0$ and repulsive when $sin\Psi_1 sin\Psi_2 < 0$. In the case of immersion forces between two particles protruding from an aqueous layer, $\Psi > 0$ for hydrophilic particles and $\Psi < 0$ for hydrophobic particles (Fig. 1.14)[98]. Moreover, the capillary charges also determine the capillary forces between two particles as shown in previous works[104–106].

1.5 Methods for quantifying cell adhesion

1.5.1 Laminar flow, optical and magnetic tweezers

In this section, I present the most widely employed state of the art techniques that enable cell characterization as well as cell adhesion force studies. Forces have a significant impact on biological mechanisms. Molecular scale forces govern a wide

range of biological motions including cellular motility and DNA replication. Force is also involved in bond formation that takes place when thermally-driven ligand-receptor unbinding forces are surmounted. Hence, a study of forces involved in biological events is essential. Numerous techniques have been developed in order to perform force measurements studies at the single-cell level. The most commonly used tools in this field are laminar flow, optical tweezers, magnetic tweezers and atomic force microscopy.

Laminar flow allows measurements of cell attachment through the cells' resistance to a shearing force. This force can be applied by exposing cells to a laminar flow in a flow chamber. The shear stresses resulting from a moving fluid near a stationary wall exert a tangential force per unit area. This quantity is analogous to pressure and is expressed in dynes/cm^2 unit. This technique allows examining the resistance of adhering cells to detachment from the substrate in response to a controlled ramping of a laminar flow inside a flow channel. The adhesion force between cells and the substrate can be, in principle, determined by breaking the contact upon applying a known force. The attachment strength can be used to study the influence of adhesion molecules and biomaterial properties on cell spreading and adhesion.

A laminar flow experimental setup includes gluing a disposable flow chamber onto a substrate (Fig. 1.15) and then both are mounted on the stage of an inverted phase contrast microscope. Next, cells in medium are fed into the flow chamber (Fig. 1.15 a) and allowed to adhere for a specified period of time. Then, fresh cell medium is injected from one end of the chamber at a ramping flow with certain speeds within certain times. The continuous detachment of cells from the substrate due to shearing forces exerted by the flow is monitored with a video camera. Fig. 1.15 c shows a sequence of images displaying the subsequent detachment of cells from the substrate. The continuous reduction in the number of cells is demonstrated in Fig. 1.15 b, where the relative area covered with cells is shown relative to the ramping increase in shear stress.

Compared to the other methods discussed here that are used for cell adhesion measurements, the laminar flow technique provides a better statistical study of cell adhesion as it allows testing many cells at the same time. However, the laminar flow setup does not provide cell adhesion measurements at the single-molecule level, and this hinders a better understanding of the behavior of cellular adhesion. Hence, other available methods, such as Single-Cell Force Spectroscopy (SCFS), are considered superior to the laminar flow technique in terms of examining cellular adhesion in greater detail.

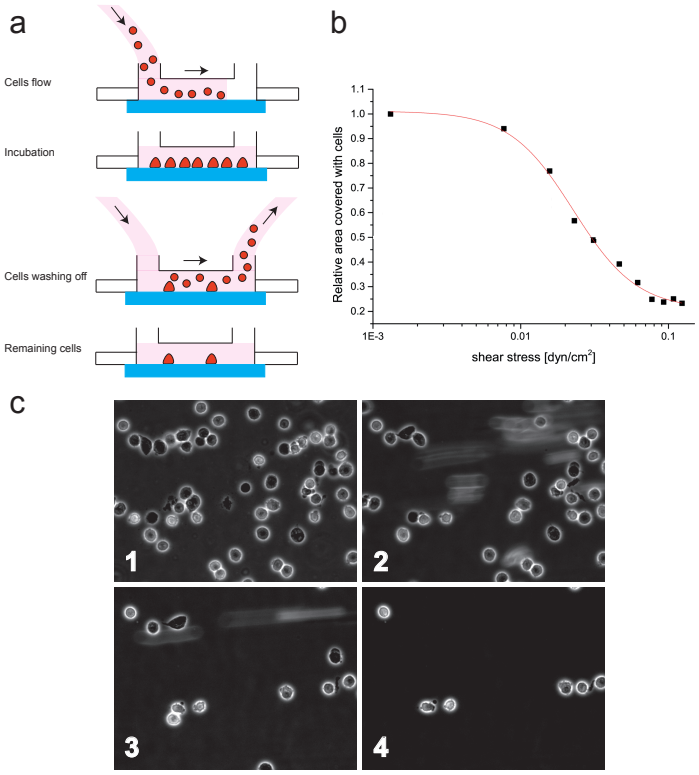

Figure 1.15: *A laminar flow experiment. (a) A schematic illustration of a laminar flow experimental setup. Before the experiment begins, a disposable flow chamber is glued onto a substrate. Cells suspended in medium are injected into the flow chamber and allowed to adhere for a predefined period of time. Then, fresh medium is fed from one of the flow chamber's ends at a ramping flow speed for a specified period of time. (b) The reduction in the relative area of the substrate covered with cells as a function of the shearing stress arising from the flowing medium within the chamber. (c) A sequence of images demonstrating the subsequent detachment of cells from the substrate.*

The optical tweezers or the optical trap technique is a widely used and versatile method in single-molecule force manipulation. It is capable of applying forces in the range of 100 pN on both nano- and micrometer sized particles while simultaneously calculating the displacement of the trapped particle with nanometer precision and millisecond time resolution[107]. These features make optical tweezers a suitable technique for force and motion measurements. The working principle of optical tweezers is as follows: A laser focused through a microscope objective onto a spot generates an optical trap. A strong electric field gradient is formed at the narrowest point of the focused beam. Particles in the proximity of the focused beam experience restoring forces that attract them towards the center of the beam where the electric field is strongest[107,108]. Despite the ability to trap particles with a fairly large size spectrum ranging between 20 nm to a few microns, there are a couple of drawbacks to this tech-

nique. The first major drawback in optical tweezers is the limit in achieving higher forces than 100 pN[107]. Also, the motion-range measureable with a stable trapping of particles is limited to around 400 nm or less[107]. Although the range can be increased through incorporation of dynamic position control of the trap and the stage, this inevitably adds complexity to the instrument. Additionally, the high intensity of the focused beam that creates the optical trap leads to local heating. This results in a local change in the viscosity of the medium and a thermal gradient that can affect the measurement[107].

The magnetic tweezers technique is a straightforward method used in single-molecule measurements. In this method, forces as little as 1 nN can be exerted in order to manipulate and, more essentially, rotate magnetic particles with a size range of 0.5 - 5 μm[107]. Magnetic tweezers have two important aspects that make this technique preferable compared to optical tweezers. The first one is that it provides a passive force clamping over large displacements[107]. The other advantage of magnetic tweezers is the capability of applying forces up to 200 pN on micron-sized particles. The operating concept of magnetic tweezers is to some extent similar to that of optical tweezers. A magnetic particle experiences a force that is proportional to the gradient of the square of an externally applied magnetic field[107,108]. Large forces can be acquired with fairly small magnetic field strengths that can generate a steep field gradient. A single-direction force can be applied on a magnetic particle by using a single magnet. However, in order to apply a force or generate torque, a minimum of two magnets are required[107]. Despite its superiority to optical tweezers in terms of the accessible force range, magnetic tweezers fall short of providing forces above 200 pN, which in turn can be easily attained by AFM. Also, the configuration of the permanent magnets does not provide the manipulation ability offered by other techniques, i.e. the manipulation is limited to a single dimension. Furthermore, in order to generate a large magnetic field and a large field gradient, high current electromagnets are needed which can cause local heating[107].

Altogether, AFM has proven to be the simplest and most versatile tool to examine adhesion on a single cell and molecular level. The superiority of AFM to other tools is represented by the wide range of forces attainable through a large diversity of cantilevers of varying stiffness values. The other significant advantages of AFM are the simplicity in sample preparation as well as the ability to perform measurements of biological samples at near-physiological conditions[107,109]. In my thesis, AFM was employed in single-cell force spectroscopy experiments that were conducted to study

and promote novel artificial dynamic environments that enable an *in situ* control of cell adhesion at the molecular scale, as will be discussed in Chapters 3 and 4. The SCFS will be discussed in detail in the following section.

1.5.2 Single-cell force spectroscopy (SCFS)

Single-cell force spectroscopy is a technique that was developed to measure cell adhesion strength to a substrate or another cell down to single-molecule level. Having an optical microscope combined to an AFM helps positioning a cell for studying cellular interactions at a specific site on functionalized surfaces, tissues or other cells[110]. Although the atomic force microscope is more widely known for using a cantilever to scan or "feel" a sample's surface and obtain an image that provides topographical information about the substrate, it can also be used as a force spectroscopy tool. In a SCFS experiment, the AFM cantilever remains stationary in the xy-direction and ramps in the z-direction at a defined location of the substrate. The cantilever deflection is recorded as a function of piezo movement in z-direction and translated into a force-distance curve (Fig. 1.17 b). The AFM cantilever exhibits a Hookean spring behavior for small deflections. Therefore, the cantilever deflection is linearly related to the applied force, which is causing the deflection. Thus, when the cantilever spring constant is determined, the cantilever deflection (d) can be translated into a corresponding force according to Hook's law: $F = k \cdot d$, where k is the cantilever spring constant[111,112].

Compared to other techniques like optical tweezers and magnetic tweezers, SCFS offers the largest force range, which varies between 10 to 10^6 pN owing to a wide variety of cantilevers available with different stiffness values[111]. Despite the higher resolution that optical tweezers and magnetic tweezers offer in the low force regime, AFM enables studying cell-to-cell interaction forces. AFM also has a major advantage over the other techniques in resolving molecular forces ranging from 5 pN up to several nN[3]. Having this force range enables studying cell adhesion with a wider scale, starting from single-molecule up to a full-cell level.

In a SCFS experiment, a tipless cantilever is used in order to prevent harming the cell that is bound to it[3]. An AFM suitable for SCFS experiments is equipped with a fluid chamber that allows measurements in aqueous environment to be performed under controlled temperatures[111]. Performing live cell experiments at controlled temperatures is an essential parameter. Most mammalian cells undergo opti-

mal metabolism at 37°C and the viscosity of their cellular membranes is also largely temperature-dependent[3]. After adding a drop of cell suspension into the fluid chamber, a single-cell is then captured (fished) by applying a gentle pressure onto it with a tipless AFM cantilever, which has been functionalized to promote cellular adhesion (Fig. 1.16 a-c).

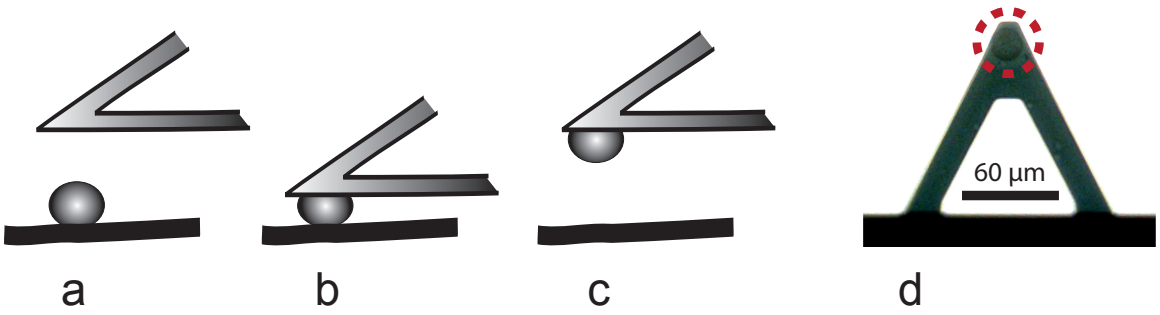

Figure 1.16: *A schematic demonstration of cell capturing in a SCFS experiment. (a) A tipless AFM cantilever functionalized with conA (Concanavalin A) is positioned above the cell. (b) The cantilever approaches the cell with a contact force of a few nN and stays in contact for several seconds. (c) The cantilever is carefully lifted off the surface and kept resting for a few minutes to ensure a firm adhesion of the cell. (d) Image of a cell-capturing tipless cantilever.*

This transforms the fished cell into a probe (Fig. 1.16 d), which is used in the setup illustrated in Fig. 1.17 a which depicts the stages comprised in a SCFS measurement. The cell-carrying cantilever is brought into contact with the substrate for a certain cell-surface contact time. During retraction, the cantilever deflection is directly proportional to the force acting on the cell and is typically plotted against the distance of the cantilever from the surface (Fig. 1.17 b). In detail: As the cantilever-bound cell vertically approaches the surface, the force remains zero until the cell reaches the surface at ≈ 0 μm. Upon further approach, the cantilever exerts an increasing force to the cell until a preset contact force is reached. After a defined contact time the cantilever movement is reversed and the cell is retracted from the substrate at a defined speed. Fig. 1.17 b shows both the approach (black) and retract (red) segments of a representative force-distance curve of a cell adhering to a substrate. In the initial part of cell retraction the cantilever releases its force load from the cell. Thus the force becomes zero again around the contact point. Upon further retraction an increasingly attractive (negative) force is detected as a consequence of cell adhesion to the substrate. With further retraction of the cantilever the pulling force reaches a critical value termed the cell detachment force (step 3 in Fig. 1.17 b), at which the cell starts to successively detach from the substrate. Under continued force load during

cantilever retraction, individual cell-substrate bonds dissociate (step 4 in Fig. 1.17 b) until the cell is completely detached from the surface and the cantilever jumps back to zero force.

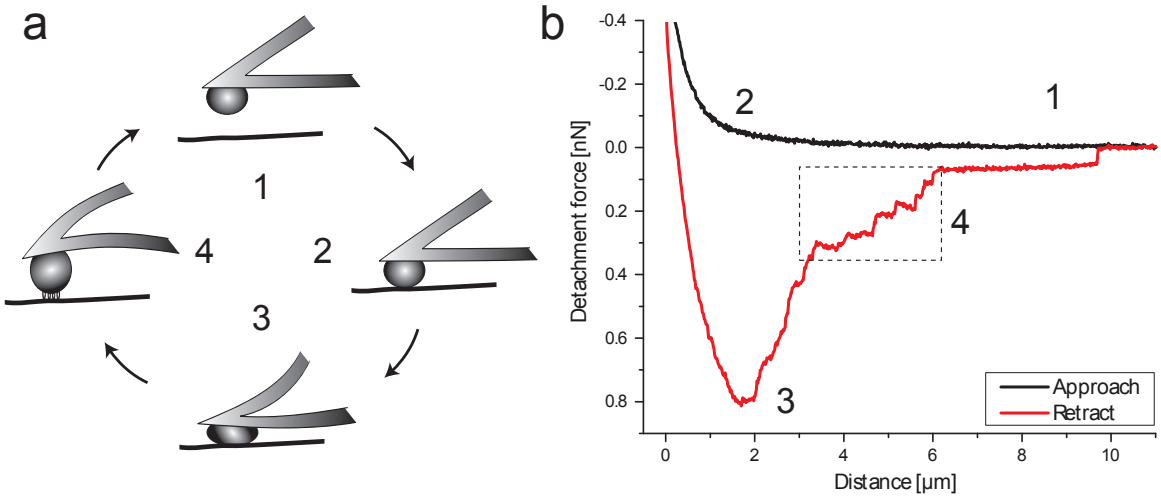

Figure 1.17: *(a) A schematic demonstration for the working principle of a SCFS experiment. The cell-capturing AFM cantilever (1) is approached to the substrate (2). A contact to the substrate is established for a specified period of time (3) during which a cell-sample adhesion is generated. As the cell retracts (4), the cantilever bends due to the strength of adhesion between the cell and the substrate[113]. (4) shows the cell-substrate bindings that developed during contact and unbind in successive rupture events as the cantilever retracts. (b) A representative force-distance curve demonstrating all the steps illustrated in (a). Both the approach (black) and the retract (red) segments of the force-distance curve are displayed.*

The retraction segment of the force curve provides a plethora of information concerning the cell adhesion process, as will be discussed in this chapter. Due to the numerous specific and non-specific events occurring during this process, interpreting these information is a challenge[111]. The retract segment can be divided into three phases: The first phase represents the inversion of force applied on the cell from pushing to pulling. As the pulling force increases, the force acting on individual cell-sample binding sites increases. If a number of receptors are acting alongside each other, the detachment force will be sufficient to cause a mechanical deformation in the cell cortex[111]. The receptors' binding strength, their number as well as their geometric arrangement dictate the force at which a cell begins to detach from the substrate. The highest recorded binding force, referred to as detachment force (F_{det}) (the minima of the force-distance curve), represents the maximum cell-substrate adhesion strength. In the second phase, individual rupture events are observed as the cell is starting to detach from the substrate (Fig. 1.17). These ruptures are representatives of receptors

that are either detaching from the substrate or are stretching away from the cell cortex and are held by the tip of a membrane tether. Either of these events can occur as long as parts of the cell body are in contact with the surface[111]. In the final detachment phase, the contact between cell cortex and the substrate is almost lost, therefore the attachment is mostly mediated through membrane tethers[111,114]. A number of parameters can be extracted from force curves obtained in a SCFS experiment, some of which will be addressed below[3].

The *detachment force* refers to the minimum force obtained from the force plot. It represents a rough initial approximation of the total cellular adhesion strength. The *distance* of a single-rupture event from the surface is a measure of a bond lifetime, as time is equal to distance divided by pulling velocity. Investigating bond lifetime distribution provides a means to study the kinetics of biological bonds. The *rupture force* of a single-rupture event is a rough estimate of a bond's actual unbinding force. Strictly speaking, only the last rupture event is an accurate measure of the true unbinding force. Despite the fact that other de-adhesion events might be larger than the last rupture, they will appear smaller in a force-distance curve due to the possibility of rebinding of the same tether. Besides, breaking a bond while others are still intact leads to a smaller force measurement as a portion of the force is redistributed towards other bonds. Hence, the rupture force of the otherwise not last rupture is not a factual representation of the strength of those de-adhesion events. The *area* under a force-distance curve has the dimension of energy and it reflects the work of de-adhesion. It is rather a representative of the energy dissipated during cell-surface separation than a summed adhesion energy contributed by individual molecular bonds. It is a complex parameter that expresses various properties such as cell mechanics, binding energy, contact area and possible active cell movements[115]. *Tethers* are lipid membrane tubes often seen in force-distance curves. A membrane tether in the form of a lipid bilayer tube has a typical diameter of 10 - 200 nm. The diameter of the membrane depends on the composition of lipids and proteins in the membrane, the sample temperature and the amount of molecules (e.g. actin filaments) that are pulled within the tube[3]. Likewise, the force needed to extend a tether also depends on the lipid composition of the cellular membrane as well as the mechanical properties of the cell cortex. Hence, the lifetime of a membrane tether depends on the receptor-ligand interaction at the membrane tip[111,116]. During cantilever retraction with a constant speed in a force experiment, the membrane tether can be identified as a constant force plateau that precedes a rupture event in a force-distance curve. In this situation, the tether acts as a force clamp and the loading rate of the bond that follows this tether is almost

zero[3]. The *slope prior to a de-adhesion event* provides information concerning the mechanical "spacer", i.e. the mechanical environment anchoring the bond(s) which open up at the subsequent de-adhesion event. A slope close to zero corresponds to tether formation, while a steep slope reflects a stiffer elastic anchorage. The slope preceding the a de-adhesion event defines the loading rate ($r = dF/dt$) applied to the ultimately ruptured bond. The loading rate is an important parameter in adhesion force measurements because the strength of a biological bond increases logarithmically with increasing loading rate (see section 1.2.1)[3,14]. This is attributed to the fact that the faster the pulling speed is, the less time thermal fluctuations have to assist unbinding, and the greater the binding strength will be[10].

1.6 Artificial dynamic cellular environments

Cell adhesion is a highly dynamic process in nature that can be intrinsically adapted to different biological circumstances through modulation of specific properties of the cellular adhesion machinery[117,118]. Proteins from the integrin family are key players in such regulation processes[119] and they are essential in a large variety of different adhesion scenarios ranging from inflammatory processes to wound healing and cell-extracellular matrix adhesion[120–122]. The ability of cells to adjust their adhesion to different environments and physiological situations influences cell-matrix adhesion and cell migration, and exhibits remarkable switchability and dynamics[123,124]. In contrast to such very dynamic and reversible *in vivo* adhesion environments, typical biomaterials provide static adhesion conditions that only change slowly over time. Such changes are first observed by the adsorption of proteins and ultimately by biodegradation and biointegration processes.

In order to engineer the highly dynamic adhesion conditions of cells found *in vivo* on biofunctional interfaces *in vitro*, novel types of surface coatings are required that provide controlled reversible and dynamic switching of cell adhesion. Such surface coatings may confer switching between a non-adhesive and an adhesive condition, but can also comprise states with defined reduction or enhancement of adhesion, as well as switching in defined patterns. This is particularly important as the time of cell exposure to adhesion ligands and the density of adhesion ligands significantly influence cell differentiation[125] and can even guide vascularization *in vivo*[126]. This shows that cells keep track of their adhesion history and that dynamic changes in adhesion signals are imperative for controlling cell functions and behavior. Unidirectional

and irreversible switching is usually achieved by light-triggered activation of caged molecules or by electrochemical switching[127–129] and all such studies showed that cells sense temporally-controlled and even tiny variations in their adhesive environment. This is in agreement with other studies that have demonstrated an extremely high sensitivity of cell adhesion to nanometer spacing and spacing gradients of adhesion ligand positions[97,130] and have demonstrated extremely fast molecular turnover rates inside cell adhesion structures[131]. Altogether, cells are able to quickly react and adapt to changing adhesion environments.

In order to explore and utilize the influence of dynamic adhesion environments on cell behavior thoroughly, biointerfaces with reversibly switchable properties are required[126,132]. Light-triggered switching of cell adhesion was conducted using photocleavable linkers[128,133–135]. However, these materials provide a one-way, irreversible switching of cell adhesion. On the other hand, dynamic and reversible control of cell adhesion is so far mainly based on thermoresponsive materials, such as poly(N-isopropylacrylamide)[136,137]. The application of thermoresponsive surfaces is, however, limited to changing cell adhesion on large surface areas as the spatial and temporal distribution of temperature stimuli is difficult to control. This makes such surfaces ill-suited for local switching at the micrometer or sub-micron level.

1.6.1 Azobenzene

Photoresponsive and photofunctional materials are among a large plethora of novel advanced materials under research nowadays. There are numerous advantages to employing light-responsive materials. Among which is the possibility of performing light stimulation remotely without disrupting other intervening materials with the localization and specificity that light activation offers[138]. Like all "smart" materials, the desired response of light-sensitive materials is programmed into the material architecture rather than being induced during the preparation process. Functional and photoresponsive smart materials show promising potential in modern industrial applications that largely depend on optical processes like telecommunications and lithography[138].

Photoresponsive materials can be generally divided into three categories. The first category includes photoswitching materials that exhibit two distinct states with light-triggered interchangeability. The second category involves photoresponsive materials illustrating a continuous response to varying light levels. The third category comprises photodeformable materials that undergo mechanical deformation elicited by light and

revert static after illumination has stopped[139]. One of the most promising photoresponsive materials available today is the azobenzene. Azobenzene has strong absorption properties and a remarkably efficient photochemistry that has been exploited in numerous functional materials. It is an aromatic molecule where two phenyl rings are joined by a nitrogen double-bond (azo linkage) as shown in Fig. 1.18.

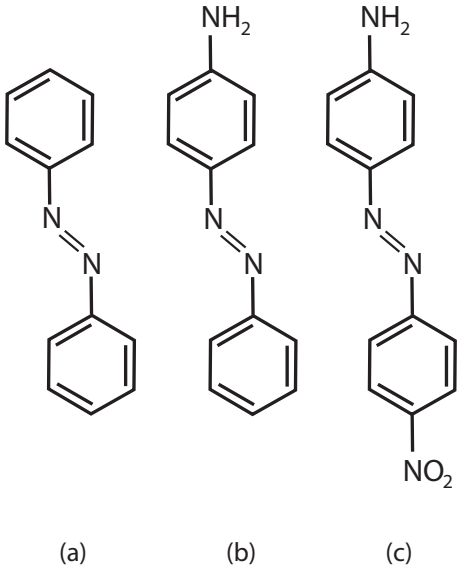

Figure 1.18: *Examples for azobenzenes. (a) Azobenzene class, (b) aminoazobenzene class and (c) pseudo-stilbene class. The photophysical properties change significantly through the substitution of aromatic rings with functional groups. Figure is modified from Yager et al.*[138].

A vast class of compounds are attainable through substituting the aromatic rings with functional groups. Those compounds, referred to as "azobenzenes", share a number of spectroscopic and photophysical properties. All azobenzenes share the unique and characteristic behavior of efficient and reversible photo-isomerization, which takes place upon absorption of photons within the absorption band (Fig. 1.19). Fig. 1.19 also shows that the azobenzene molecule changes its length from $9\mathring{A}$ in the *trans* configuration to $5.5\mathring{A}$ in the *cis*[140,141].

Azobenzenes have two isomeric configurations: A thermally stable *trans* state and a metastable *cis* state. The *trans* state transforms to the *cis* form upon irradiation. Reversion from the *cis* to the *trans* state takes place through irradiation with a different wavelength or through thermal relaxation that occurs within a timescale that is specific to the molecule's substitution pattern. The clean chemistry offered by these systems gives rise to various photoswitching and photoresponsive behaviors[138,139].

As described by Rau[142], azobenzenes are divided into three spectroscopic classes

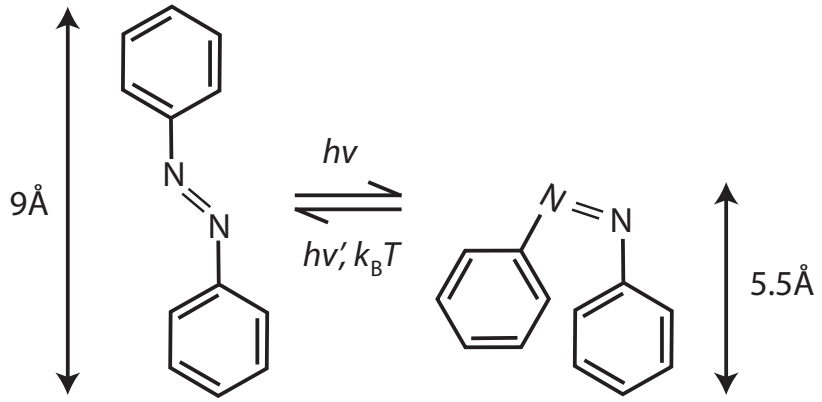

Figure 1.19: *The switching behavior of the azobenzene molecule. The molecule exists normally in the stable trans state. Upon absorption of a photon during UV exposure, the molecule isomerizes to the metastable cis state. The cis molecule isomerizes back to the trans state through either thermal relaxation or exposure to a wavelength within the cis absorption band. The azobenzene's length changes from 9Å in the trans configuration to 5.5Å in the cis. Figure is modified from Yager et al.*[138].

(Fig. 1.18). The first class is the azobenzene-type molecules that are similar to unsubstituted azobenzenes. The other class is aminoazobenzene-type molecules that are ortho- or para-substituted with an electron-donating group. The third type are the pseudo-stilbenes that are substituted at the 4 and 4' positions with an electron-donating and an electron-withdrawing group such as amino and nitro group[138]. The latter (called pseudo-stilbene because of their similarity to stilbene photochemistry) have counterposing electron-withdrawing and electron-donating groups that create a strong asymmetric electron distribution with the conjugated system. This yields a considerable overlap between the *trans* and *cis* absorption spectra. Thus, illumination of this molecule with a single wavelength light induces a cyclic *trans*-to-*cis* and *cis*-to-*trans* photoisomerization. This overlap in the absorption spectra is absent in other azobenzenes and thus two different wavelengths of light are needed to switch between the two isomeric states.

1.6.2 Push-pull azobenzene

Molecular and synthetic photoswitches have been widely used in biological research due to accurate spatiotemporal control provided by light[132]. One molecule in particular that attracted more attention for its ability to withstand chemical modifications is azobenzene[132,143]. However, regular azobenzenes impose a serious shortcoming for use

in biological research: Isomerization from the *trans* to the *cis* isomer takes place though illumination with UV light. Long UV exposure is problematic in biological systems cause it leads to damage and also UV light has a poor penetration in mammalian tissues[143]. The second problem with regular azobenzenes is their bistability. Despite the fact that the *cis* isomer is capable to relax back to the lower-energy more stable *trans* isomer, the half-life is in the range of minutes to hours[143]. All these problems can be overcome using a modified azobenzene that is activated with a single wavelength within the visible part of the spectrum. This azobenzene is capable of relaxing back instantaneously to the inactive *trans* state in the absence of light. A common example of such visible-light triggered azobenzenes is the push-pull azobenzene. It is called like that because one benzene ring is ortho- or para-substituted with an electron-donating group, while the other ring is substituted with an electron withdrawing group. This yields a red-shift in the absorption as well as a decrease in the energy barrier for the *cis*-to-*trans* isomerization, i.e. it will offer a rapid (microsecond) thermal reversion (*trans*/*cis* isomerization) and a complete resetting of the *trans* state in the absence of light[132,144,145].

1.6.3 Using conventional azobenzene to switch cell adhesion

A very powerful strategy to control cell adhesion with high spatial and temporal resolution is the use of reversibly photoswitchable molecules, such as azobenzenes. Azobenzenes can be switched with light between two isomerization states, i.e. a *cis* and a *trans* state. Once immobilized on surfaces, two defined surface conditions can be achieved. Azobenzenes have proven to be highly suitable molecules for developing photoswitchable materials with applications from optical devices to surfaces and polymers[146]. For specific control of cell adhesion, azobenzenes can be biofunctionalized with bioactive molecules such as RGD (Arginine-Glycine-Aspartate) peptides, which are ubiquitous cellular adhesion ligands that bind many members of the integrin cell adhesion receptor family[147]. Recent projects that employed RGD-functionalized azobenzenes showed promising results in controlling cell adhesion[148–150], but required at least one hour of illumination with UV light to photoswitch surfaces. Such long exposure to UV light is not suitable for dynamic biointerface applications due to severe phototoxic damage to living cells[151]. To date, the dynamic control over cell adhesion properties is still a highly challenging task, but once successful, it could revolutionize biointerface research and many biomaterials applications[152].

1.6.4 Using push-pull azobenzene to switch cell adhesion

Conventional azobenzenes have attracted a lot of attention as molecular photoswitches due to their ability to accommodate chemical tailoring that enables alteration of the wavelength used for photoisomerization, thermal relaxation rate and the steric rearrangements upon isomerization[132,153,154]. However, the bistability of regular azobenzenes can be problematic due to the capability of the *cis* isomer to relax back to the lower-energy, more stable *trans* isomer[143]. Also, using a second wavelength to switch the metastable *cis* state means that the biological system will be exposed to a wider, possibly undesirable, range of the electromagnetic spectrum[143]. Instead, the push-pull type of azobenzenes are great alternatives to the regular ones, as they can be set reversibly into either an active and an inactive state. Active is a state of rapid thermal *trans*/*cis* switching, and thus inducing mechanical oscillation, using a single wavelength within the visible part of the spectrum. Once irradiation is seized, the molecules switch into an inactive state where a complete resetting of the *trans* state takes place[144,145]. Such push-pull substituted azobenzenes have previously, for example, been used to exert large forces in polymers[155]. Hence, Push-pull azobenzenes are good candidates for use as molecular switches in biological context where circumvention of UV is essential[156]. Due to their ability to isomerize through irradiation with visible light, these azobenzenes overcome the limitations of long UV exposure that leads to significant implications in biology represented by cellular toxicity[157], mutations and alterations in cell signaling pathways[158]. Push-pull azobenzenes can tackle limitations in biological processes where two specific wavelengths are needed to achieve a two-way switching of a desired biological property[156].

Chapter 2

Surface Nanostructuring using Block-Copolymer Micelle Nanolithography

2.1 Introduction

Block-Copolymer Mmicelle Nanolithography is a versatile and a widely used method to produce quasi-hexagonal metal nanoparticle patterns on various types of surfaces including Teflon[159], silicon and glass[160] as well as hydrogels[161]. Such substrates are exploited in numerous applications such as biomimetic optics[84], protein binding[162] and also controlled cell adhesion[85,115,163]. However, this method falls short of providing a controlled allocation of regular arrays of nanoparticles with particular spacing onto micropatterns. Superimposing such quasi-hexagonal nanopatterns onto an additional microstructure to create a so-called micronanostructure[1] is highly advantageous in various applications. Living cells, for instance, exhibit a great capability to react on both biofunctionalized nano-[163] and microstructures[165]. Additionally, the ability to regulate gold nanoparticles spacing on the microscale is a very attractive aspect in applications like DNA chips[166], nanowire fabrication[167] and optically active nanocoatings[84].

Previous attempts to achieve micronanostructures using a combination of BCML-generated nanopatterns and microstructures include electron beam lithography[168] and photolithography[169] top-down approach. The fabrication of such structures using those

[1]Part of this work is published in Kadem *et al.*[164], *Langmuir*, 2015.

techniques are inhibited to microscale areas consisting of patterns having a specific gold interparticle spacing separated by uncoated regions[170]. The production of micronanostructures with various gold nanoparticle spacing on neighboring areas would be a very time-consuming method utilizing the above mentioned approach due to the required repetition of coating and lithography steps[72]. Moreover, precise alignment of multiple lithography and BCML processes would be a major hurdle. Altogether, a simple and high-throughput method to fabricate neighboring nanopatterned arrays within a microstructure having different defined interparticle spacings remains a challenge. In this chapter, a simple and straightforward method is presented that offers great potentials for high-throughput fabrication of nanoparticle structures with well-defined interparticle spacing on nanotopographic segments of Si substrates. This method comprises the usage of a mere single BCML step to deposit gold nanoparticles on substrates and yield neighboring microarrays of quasi-hexagonal nanoparticle distributions that are significantly different in their interparticle spacing. Although surface disruptions impair the regularity of the quasi-hexagonally distributed nanoparticles typically created using BCML[171,172], this method exploits this surface dis-uniformity in the shape of sharp edges on Si substrates to guide gold-loaded micelles into the microstructure. Whereas the topographic height of the segments play a dominant role of dictating the spacing between gold nanoparticles, the arrangement of these nanoparticles is regulated by immersion forces as well as their self-assembly within the segments. Additionally in this chapter, a second method to break the symmetry of the particles distribution is demonstrated. This method employs a combination of particles self-assembly with pre-structured patterns produced by photolithography to create aperiodic gold nanoparticles distribution on various substrates. Based on this top-down and bottom-up approach, this method enables a guided allocation of nanoparticles to specific areas of the substrate. Both of these two novel strategies are greatly promising methods for producing regular metallic nanopatterns on various types of substrates for a wide range of applications.

2.2 Symmetrical nanoparticle patterning on substrates

2.2.1 Varying interparticle distance

Well-ordered metallic nanoparticle patterns with defined interparticle distances can be obtained using BCML[171]. This technique also offers a control over the interpar-

ticle spacing through utilizing different diblock copolymers with various molecular weights[163]. In the work of Arnold *et al.*, controlling cell adhesion and spreading was attempted via tailoring the distances between gold nanoparticles on glass substrates. The results from their work exhibit cell responsiveness to nanometer-scale alteration in the distance between anchorage points represented by gold nanoparticles functionalized with RGD-peptide.

In this work, varying the interparticle distance was obtained through changing the rotational speed during the spin coating process. In a BCML experiment, gold-loaded micelles were spin coated onto two glass substrates with two different speeds, which were 3000 and 7000 rpm. In order to remove the micellar polymer, the samples were exposed to plasma using a gas mixture of hydrogen and argon (10 % H_2, 90 % Ar) in a plasma etcher for 1 h at 0.4 mbar and 300 W. Fig. 2.1 shows that increasing the spin coating speed increases the interparticle distance as well as the order parameter. The interparticle distance for the sample prepared with 3000 rpm was 70.1 ± 5 nm with an order parameter of ≈ 60 %. Increasing the spin coating speed to 7000 rpm yielded an interparticle distance of 87.8 ± 6 nm and an order parameter of ≈ 63 %. The calculation of both the interparticle spacing and the order parameter is illustrated in 2.2.2.

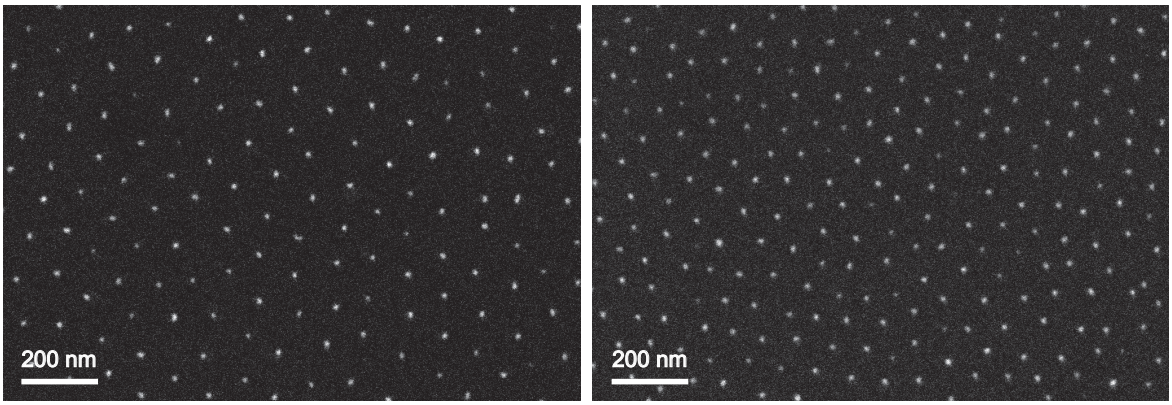

Figure 2.1: *Dependance of the interparticle distance and order parameter on spin coating speed. Left: A glass substrate spin coated at 7000 rpm yielded an interparticle distance and an order parameter of approximately 88 nm and 63%, respectively. Right: A glass substrate spin coated at 3000 rpm yielded approximate interparticle distance and order parameter values of 70 nm and 60%, respectively.*

2.2.2 Calculation of order parameter and interparticle spacing

In order to calculate the average gold interparticle distance as well as determining the hexagonal accuracy (order parameter) of the pattern, a mathematical algorithm was used to verify the angles and spacings between neighboring particles. This algorithm was developed by Dr. P. Girard as a plug-in to the ImageJ image processing and analysis software.

The calculated 6-fold bond orientation order parameter Ψ_6 is defined as

$$\Psi_6 = \left| \frac{1}{N_{bonds}} \sum_j \sum_k e^{i6\theta_{jk}} \right| \tag{2.1}$$

where N_{bonds} is the number of bonds between a central particle and its nearest neighbors. The angle between a particle and two of its neighbors is represented by θ_{jk}, where j being the central particle and k are the neighboring ones as shown in Fig. 2.2.

The difference between each angle in a real (imperfect) hexagon and an ideal 60° hexagon is calculated by the inner sum in equation 2.1. The outer sum is for a repeated calculation of all imperfect hexagons found in the SEM image.

The factor $1/N_{bonds}$ in this equation is to normalize the calculated value, so that a value of 1 is the highest (best) and 0 is the lowest. The order parameter value is inversely proportional to the standard deviation of the mean distance of adjacent micelles. In a perfect hexagon, every angle and distance is equal to the other (Fig. 2.2). This value represents a measure of the quasi-hexagonal distribution[173].

The second method I utilized to calculate the interparticle spacing in this thesis is based on a particle-density algorithm that functions using a custom-written Matlab routine. In this method, the particle density within a specific given area is first determined and then, assuming a perfect hexagonal particle distribution, the interparticle spacing is acquired.

The working principle for this method is as follows: When every three adjacent particles are located at the three vertices of a equilateral triangle with an area B (e.g. the red triangle in Fig. 2.2), and there is an m number of triangles confined within an

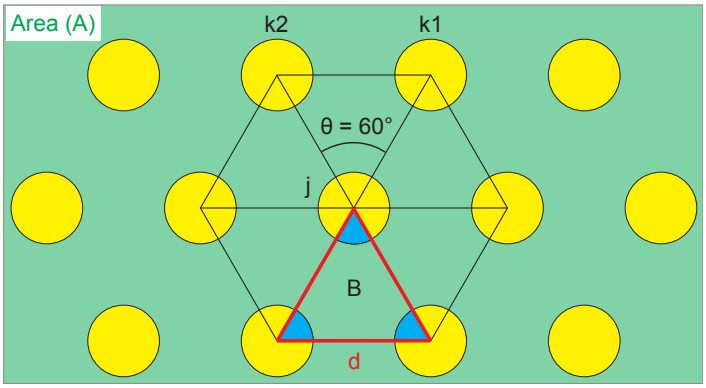

Figure 2.2: *A graphic description for the 6-fold bond orientation. In order to evaluate the quality of the hexagonal patterns, all angles between each particle (j) and its two nearest neighbors (k_1 and k_2) are compared to a perfect 60° angle using equation 2.1. Figure is modified from Williges et al.*[173].

area A, then

$$A = m \cdot B \tag{2.2}$$

The number of triangles in the specified area represents only half the number of particles in this area, which is given by 2n. Thus, the following substitution can be made

$$A = 2n \cdot B \tag{2.3}$$

Because every three particles make up one triangle, and every particle is shared by 6 neighboring particles, therefore the area of a single triangle encloses only a half particle i.e. $3 \times \frac{1}{6}$ of a particle. The area of the equilateral triangle itself equals $B = d^2 \cdot \sqrt{3}/4$.

$$A = 2n \cdot \frac{d^2\sqrt{3}}{4} \tag{2.4}$$

where d here represents the interparticle spacing and is therefore given by

$$d = \sqrt{\frac{2A}{n\sqrt{3}}} \tag{2.5}$$

2.3 Symmetry breaking of nanoparticle patterns by photolithography

Guided self-assembly offers and provides a powerful method to conduct small-scale structuring of aperiodic patterns where nanometer sized features are separated by microscopic scale distances. Self-assembly of particles in combination with topographical pre-structuring using photolithography offers the breaking in the symmetry of the particle distribution on surfaces and provides guided allocation of nanometer sized features to specific areas of the substrate[70]. With this process that was first introduced by Aydin *et al.*, quick and reproducible fabrication of well organized micro- and nanostructures with a resolution down to 50 nm is feasible[169]. The technique represents an innovative approach to combine self-assembly processes with conventional lithography. The combination of those two techniques provides a versatile method for the production of small-scaled features as well as meeting demands of controlled structures allocation of periodic and aperiodic patterns with the required separation distances.

In order to fabricate patches of gold nanoparticles on substrates, gold-loaded micelles are deposited on topographical pre-structures originated using photolithography. The combination of photolithography and self-assembly through block-copolymer micelle nanolithography is shown schematically in Fig. 2.3.

These aperiodic patterns of nanoparticles can be obtained by two approaches, both of which employ a combination of photolithography and BCML[169]. The first one is represented by using BCML first in order to create an extended array of gold nanoparticles. A positive photoresist is then spin coated on the nanoparticles-decorated surface and irradiated using UV light in a photolithography process. After developing, the exposed particles are removed through a gentle ultrasonic treatment in an aqueous solution of cysteamine. Eventually, the rest of the photoresist is stripped out using acetone and the desired gold nanoparticles patterns remain on the surface (Fig. 2.3 a). Fig. 2.4 shows patches of gold nanoparticles on glass substrates.

The second approach that exploits the combination of both photolithography and BCML to create patches of gold nanoparticle patterns separated by non-structured areas involves using defined pre-structured surfaces as a platform for micelles deposition. In a photolithography process, a positive photoresist-coated substrate is irradiated with UV light through a mask that contains the desired pattern. Using BCML,

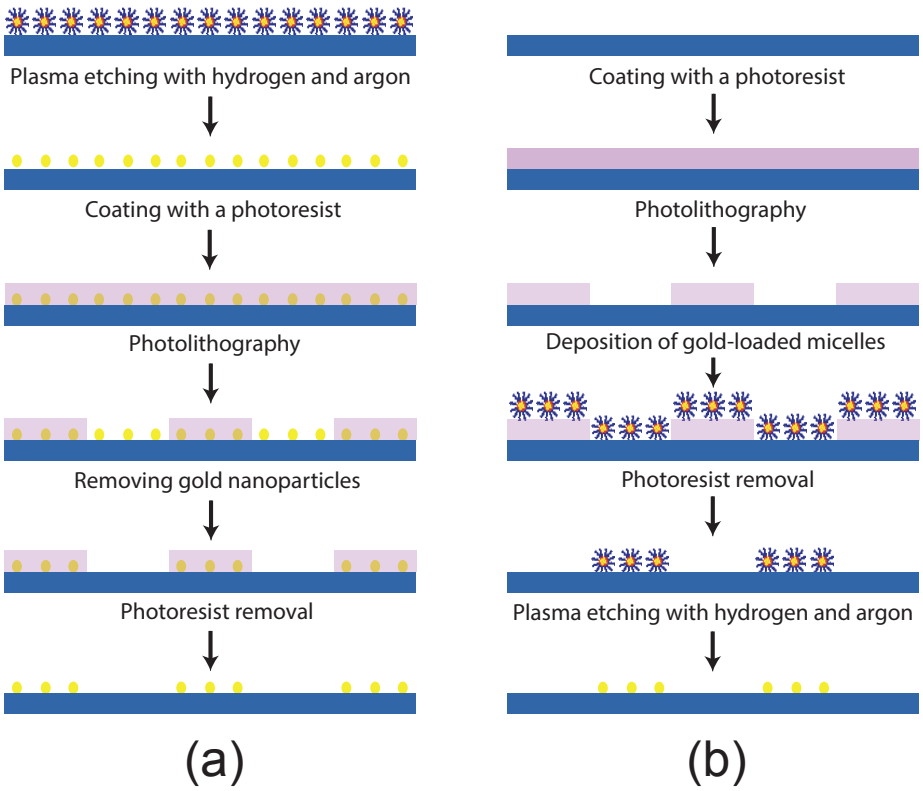

Figure 2.3: *Two approaches for generating micropatches of gold nanoparticle arrays using a combination of photolithography and BCML. (a) A positive photoresist is spin coated onto a nanoparticle-patterned substrate. After developing the photoresist in a photolithography process, the exposed particles are removed in a sonification step in a cycteamine solution. (b) In a photolithography process, a positive photoresist is spin coated onto a substrate and irradiated through a mask with a predefined pattern. Gold-loaded micelles are then spin coated on the substrate, followed by a removal of the remaining photoresist that leaves nanoparticle arrays on the predefined patterns.*

gold-loaded micelles are then spin coated on the pre-structured surface. Afterwards, those micelles are pinned onto the surface through a short exposure to hydrogen-argon mixture plasma in order to avoid washing off during the topographic pre-structure lift-off process that follows. In the lift-off process, the micelles that are located on top of the remaining photoresist are removed, while the ones in contact with the substrate stay. Eventually, the sample undergoes a plasma-etching process using a mixture of hydrogen and argon in order to remove the polymeric shells surrounding the gold nanoparticles (Fig. 2.3 b). The gold nanoparticle patches from this approach are shown in Fig. 2.4 b.

However, the multiple steps required to fabricate these patches as well as the arduous work needed to acquire an accurate alignment of the photomask during the photolithography process make these fabrication methods slow and tedious. Thus, in

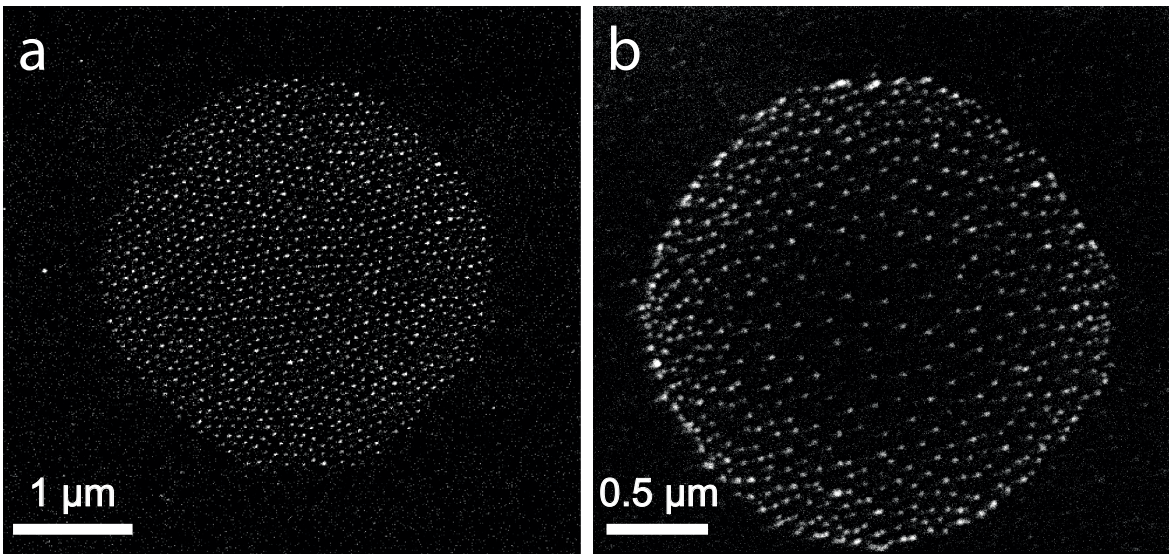

Figure 2.4: *Micropatches of gold nanoparticle arrays fabricated through symmetry breaking using a combination of photolithography and BCML. (a) is a nanoparticle pattern produced using method (a) in Fig. 2.3. (b) is a pattern that was generated using method (b) in Fig. 2.3.*

the following section, a novel, simple and straightforward fabrication method for a controlled allocation of nanoparticles is presented.

2.4 Symmetry breaking of nanoparticle patterns by nanotopography

The formation of micronanostructures through a superposition of nanopatterns and an additional microstructure is advantageous in numerous applications[164]. Such applications where a controlled spacing of gold nanoparticles on the microscale is beneficial include DNA chips[166], nanowire fabrication[167] and optically active nanocoatings[84] in addition to biofunctionalized nanopatterns[163] and microstructures[165] for cell adhesion experiments. Despite previous attempts to generate micronanostructures that were based on using a combination of BCML with either photolithography[169] or electron beam lithography[168], the produced patterns were restricted to microscale areas. Also, micronanostructure production using these methods require multiple coating/lithography cycles, hence the process is considerably time-consuming[72].

In classical BCML, an undisturbed self-assembly of micelles is required to acquire a homogeneous distribution of nanopatterns. This in turn requires substrates with

no surface disruptions in order to attain a regular quasi-hexagonal distribution of nanoparticle arrays[171,172]. However, in this section I present a straightforward method that exploits surface dis-uniformity in the shape of sharp edges on Si substrates to guide gold-loaded micelles into a certain microstructure. On one hand, the height of those microtopographic segments dictates the interparticle distance between gold particles. On the other hand, immersion forces and self-assembly control the nanoparticle arrangement within the segments. In this method, a mere single BCML step is performed to deposit arrays of quasi-hexagonally arranged gold nanoparticles with significantly different interparticle spacings. This technique offers an easy approach to a high-throughput fabrication of nanoparticle patterns with well-defined interparticle spacing on nanotopographic segments.

A microstructured Si substrate is the heart of this method. The microstructures are presented in the form of quadruple surface patterns of 5 × 5 μm square segments that were produced using photolithography and wet etching (Fig. 2.5 a). To obtain such microstructures, a single-side-polished, 4 inch Si wafer was coated with a photoresist then irradiated with UV light through a mask that contains stripes of 5 μm width with 5 μm intervals. The following wet etching process yielded a surface topography that exhibits 5 μm wide and 60 nm deep stripes. After stripping off the remaining resist, the wafer was spin coated again with a photoresist and then exposed to UV light for a second time through the same mask, which had been rotated by 90°. The final etching step following the second lithography procedure results in a multileveled checkerboard topography of 5 × 5 μm segments in a quadruple pattern with a height difference of 60 nm between adjacent segments (Fig. 2.5 b). A detailed description of the microstructure fabrication process is addressed in Appendix B.1.4.

Introducing the nanostructures onto the micropatterned substrates was performed through spin coating gold-carrying micelle solution in a BCML procedure (Fig. 2.6 a). After removing the polymer matrix of the micelle shell using plasma treatment with a mixture of hydrogen and argon (10 % hydrogen, 90 % argon), elementary gold nanoparticles remain on the surface of the Si substrates. A detailed description of the BCML process on the Si microstructures can be found in Appendix B.1.4. A scanning electron microscopy (SEM) image of a plasma-etched substrate that has a gold nanopattern on the nanotopographic Si substrate is shown in Fig. 2.6 b.

A representative magnified SEM image for the center of a quadruple segment with a nanoparticle coating is shown in Fig. 2.7 a. The four areas of the quadruple are designated *a*, *b1*, *b2* and *c* according to the thickness of their silicon dioxide layer.

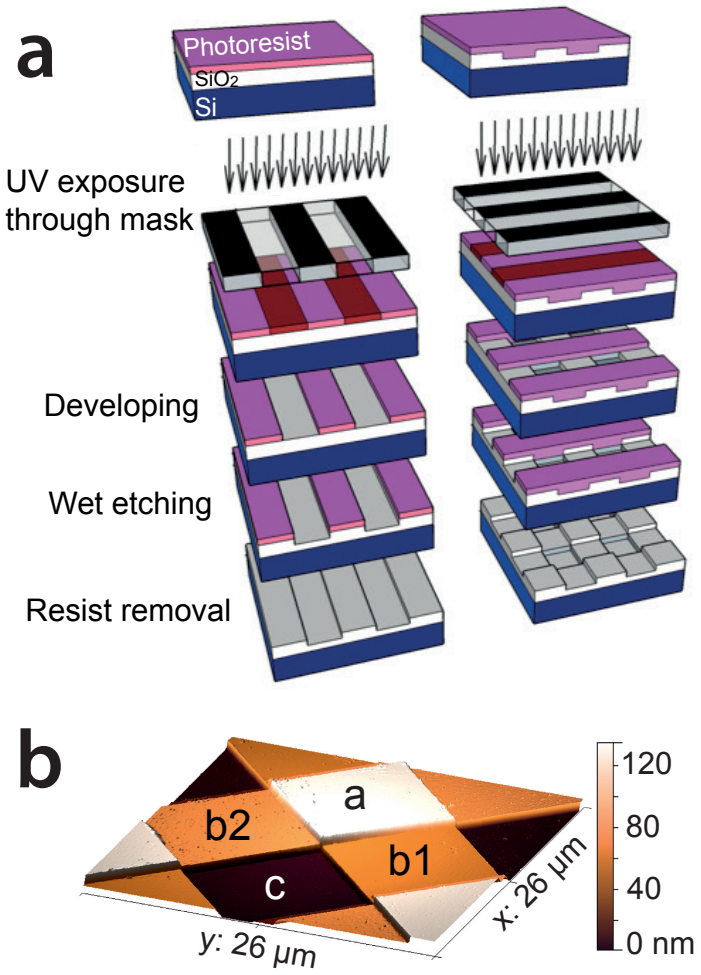

Figure 2.5: *(a) Generation of nanotopographic Si substrates with a quadruple structure by photolithography and wet etching. (b) AFM surface scan of the patterned substrate showing the four 5 × 5 µm segments (a, b1, b2 and c) with height differences of 60 nm between adjacent segments. Reprinted by permission from the American Chemical Society: Langmuir*[164]*, copyright 2015.*

Segment *a* is the highest, *c* is the lowest and segments *b1* and *b2* have an identical intermediate value. Visible differences in the interparticle spacing from one segment to the neighboring one can be seen in the image (Fig. 2.7 a). For a detailed analysis of these differences, 1 × 1 μm spots on segments of different topographical height were examined and the average interparticle spacing on each segment was measured. This detailed analysis of the interparticle spacing on each segment will be discussed in section 2.4.1. The average interparticle spacings for a nanotopographic substrate spin coated at 1000 rpm that was determined using our particle-density-based algorithm (see section 2.2.2) is shown in Fig. 2.7 b. The topographically highest segment *a* exhibits a significantly greater average interparticle spacing compared to the lowest

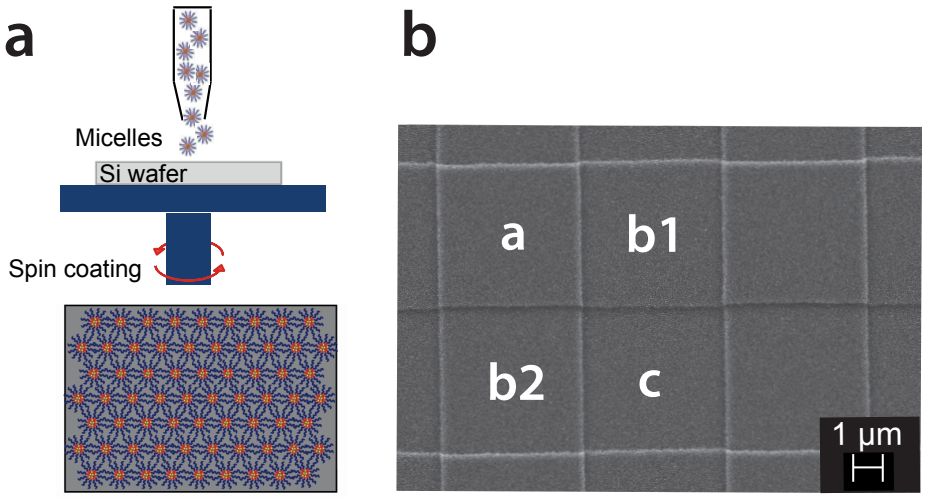

Figure 2.6: *(a) Schematic illustration of the BCML procedure. A micelle solution is transferred onto the Si wafer in a spin coater, and micelles self-assemble on a planar substrate into a quasi-hexagonal structure. Plasma treatment removes the polymer micelles, leaving only metallic gold nanoparticles on the substrate. (b) SEM image of the nanostructured nanotopography showing the four segments a, b1, b2 and c of the quadruple. Reprinted by permission from the American Chemical Society: Langmuir*[164]*, copyright 2015.*

segment *c*, with a difference of approximately 23 nm. On the other hand, both *b1* and *b2* segments display similar intermediate interparticle spacings. In agreement with the particle-density analysis of the interparticle spacing, the nearest-neighbor analysis demonstrated comparable results [(*a*) 84.1 ± 9.9 nm, (*b1*) 71.8 ± 9.5 nm, (*b2*) 71.4 ± 9.5 nm, (*c*) 63.0 ± 10.0 nm], where the standard deviation in this method is a measure of the variation in spacing of individual nanoparticles.

In order to elucidate the observed dependence of interparticle spacing on a segment's topographical height, also the distribution of micelles on the substrate prior to plasma etching using Atomic Force Microscopy (AFM) was investigated. The AFM images illustrate that a monolayer of micelle solution covers the substrate uniformly and a significant difference in micelle coating density can be seen among the four segments (Fig. 2.8 a). Segment *a* is depleted in micelles at the edges bordering lower segments *b1* and *b2*, which have the same topographical height. On the other hand, segments *b1* and *b2* are in turn depleted in micelles toward segment *c*, which is the lowest segment. Further analysis of the height profiles of these AFM images (Fig. 2.8 b) was carried out and is shown as arrows in Fig. 2.8 a. The height profiles provide evidence that only a monolayer of micelles is present in the center of each segment, as the height difference between the lowest and the highest segment is identical to the height

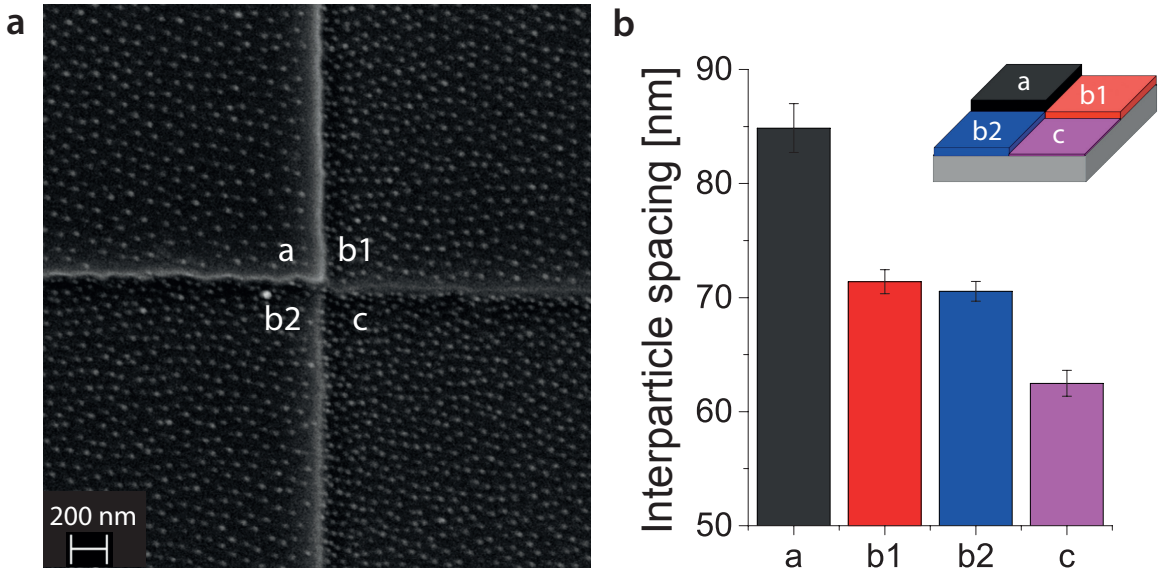

Figure 2.7: *(a) SEM image of a gold-nanoparticle-decorated quadruple structure revealing variations in interparticle spacing between the different segments of the quadruple. (b) Interparticle spacing of nanoparticles on segments of different height, averaged from four quadruple structures. Clearly, the interparticle spacing is controlled by the segment height. The interparticle spacing was calculated from particle densities, assuming a hexagonal particle arrangement. Error bars denote the standard deviation. Inset: Color code of segments within a quadruple structure. Reprinted by permission from the American Chemical Society: Langmuir*[164]*, copyright 2015.*

difference of segments in the underlying Si microstructure. Additionally, it exhibits that micelles are loosely packed on segment *a* compared to segment *c* where they are densely packed. These observations are consistent with our interparticle spacing analysis of plasma-etched substrates shown in Fig. 2.7. Stacking of micelles can be also seen at the upward edges of the nanotopography.

The arrangement of micelles is attributed to two types of forces that take effect as the solution starts to evaporate: Steric interactions and immersion forces, which include drag forces due to the receding liquid surface, friction, convection, interparticle interaction, and capillary forces[69,174]. During solvent evaporation, micelles near the edge of neighboring segments experience such immersion forces (mainly capillary and drag forces) that sweep them towards a lower segment (Fig. 2.9 b). This leads to an accumulation of a greater number of micelles in lower segments and effectively results in higher particle densities and thus smaller interparticle spacing. This also causes disordering in particles distribution at the edges that leads to a lower order parameter. As the evaporation process continues, the edges of the nanotopographies

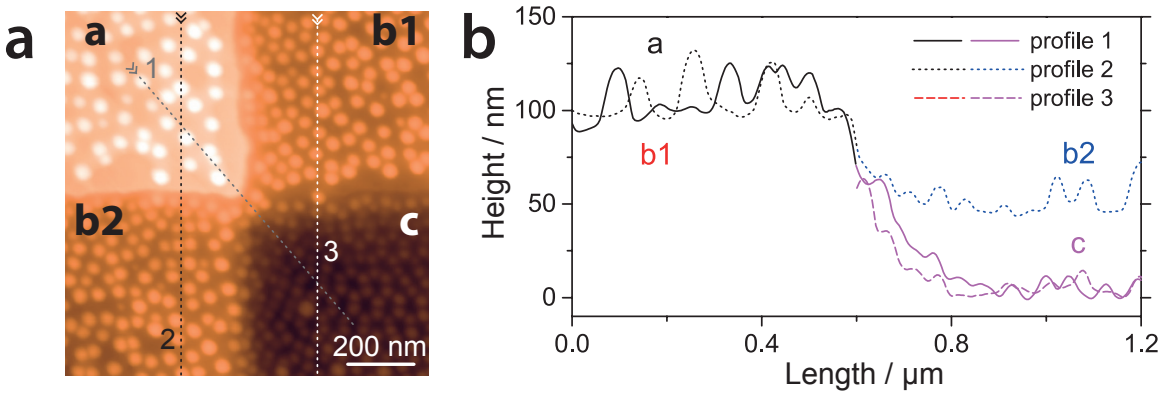

Figure 2.8: *(a) AFM image showing the distribution of micelles after the spin coating procedure. Depletion in nanoparticles at the edge of the highest square and the enrichment of nanoparticles at the edges of lower squares are clearly visible. (b) Height profiles for lines 1, 2, and 3 shown in (a) revealing the stacking of micelles at the edges of lower segments. These data also prove that indeed monolayers of micelles are adsorbed on all four segments. Reprinted by permission from the American Chemical Society: Langmuir*[164]*, copyright 2015.*

act as pinpoints for menisci and capillary effects create a flux of micelle solution toward the walls. This causes micelles to pile up at the boundaries of lower segments compared to higher neighboring segments (Fig. 2.9 b).

A detailed analysis of this edge effect is displayed in Fig. 2.9 a. The data show clearly that a depletion of nanoparticles on a topographically higher segment leads to an enrichment of nanoparticles on the adjacent lower segment.

2.4.1 Response of particle distribution to spin coating speeds

A detailed analysis was carried out for both the interparticle spacing on each of the topographical segments as well as the difference in spacing between those segments in response to changing spin coating speed. In order to conduct this study, the interparticle spacing has been analyzed on 9 spots on each of the four segments, each with an area of 1×1 μm as displayed in Fig. 2.10. The designated name for each spot represents its position from the segment's edge.

This method allows a comprehensive study of the deviation in interparticle spacing between different locations of the same segment. The examined samples were prepared spin coating speeds of 1000, 5000 and 7000 rpm, as demonstrated in Fig. 2.11. This study illustrates a clear correlation between the organization and spacing of nanoparticles on the one hand and the spin coating speed used during preparation on the

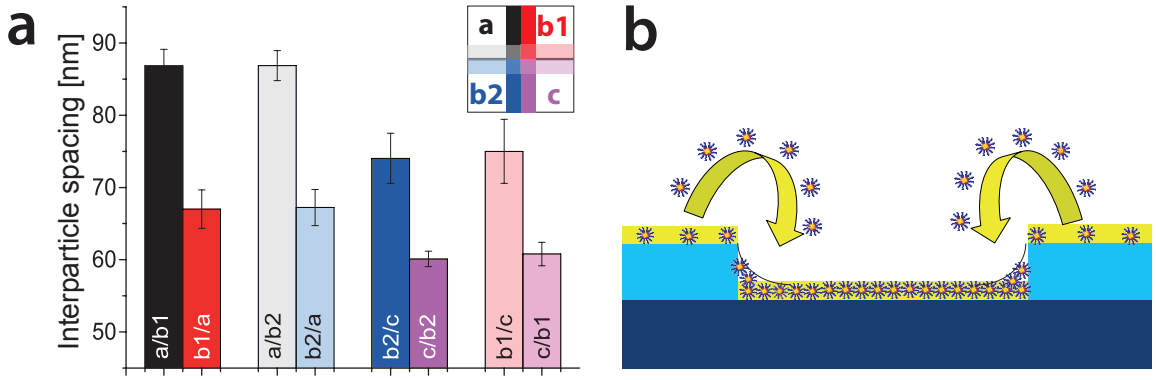

Figure 2.9: *(a) Average of interparticle spacing along a 1 µm broad stripe at the edge of different segments (x/y refers to the 1 µm broad stripe on segment x that is adjacent to segment y). The data quantify the enrichment and depletion of nanoparticles on the lower and higher segments, respectively. Furthermore, the data is consistent, as segments b1 and b2 have identical heights and lead to identical interparticle spacings. (b) Sketch of the proposed mechanism for micelle enrichment in the lower segments, caused by a flow of micelles toward the lower segments of the quadruple structure during solvent drying. Reprinted by permission from the American Chemical Society: Langmuir*[164]*, copyright 2015.*

other hand. Increasing the spacing between nanoparticles on the segments is attainable through increasing the spin coating speed as shown previously in section 2.2.1 and also in the work of Arnold *et al.*[97]. At a spin coating speed of 1000 rpm, the interparticle spacing appears to be almost homogeneous throughout each segment (Fig. 2.11 a). However, a significant accumulation of particles appears near the edges of lower segments of the quadruple at higher rpm as displayed in Fig. 2.11 b and c. Despite that accumulation, the difference in interparticle spacing between the centers of the segments is still minor, i.e. the difference becomes less significant the farther away the considered spot is from the segment's edge (Fig. 2.11 b and c).

Likewise, the disorder in the hexagonal pattern is restricted to a few hundred nanometers near the edges as displayed in Fig. 2.12, which illustrates the importance of selecting the optimum spin coating speed in this method. That is to say, low spin coating speeds yield larger interparticle spacing differences between the centers of different segments (here $>$ 20 nm between segments a and c for 1000 rpm, Fig. 2.7 b and Fig. 2.11 a) as well as a more homogeneous particles distribution over the entire segment compared to higher speeds.

Additionally, in an attempt to improve nanoparticle distribution at the segment edges, I followed a method based on adding a subsequent ultrasound annealing step after the spin coating process as explained in the following section[173].

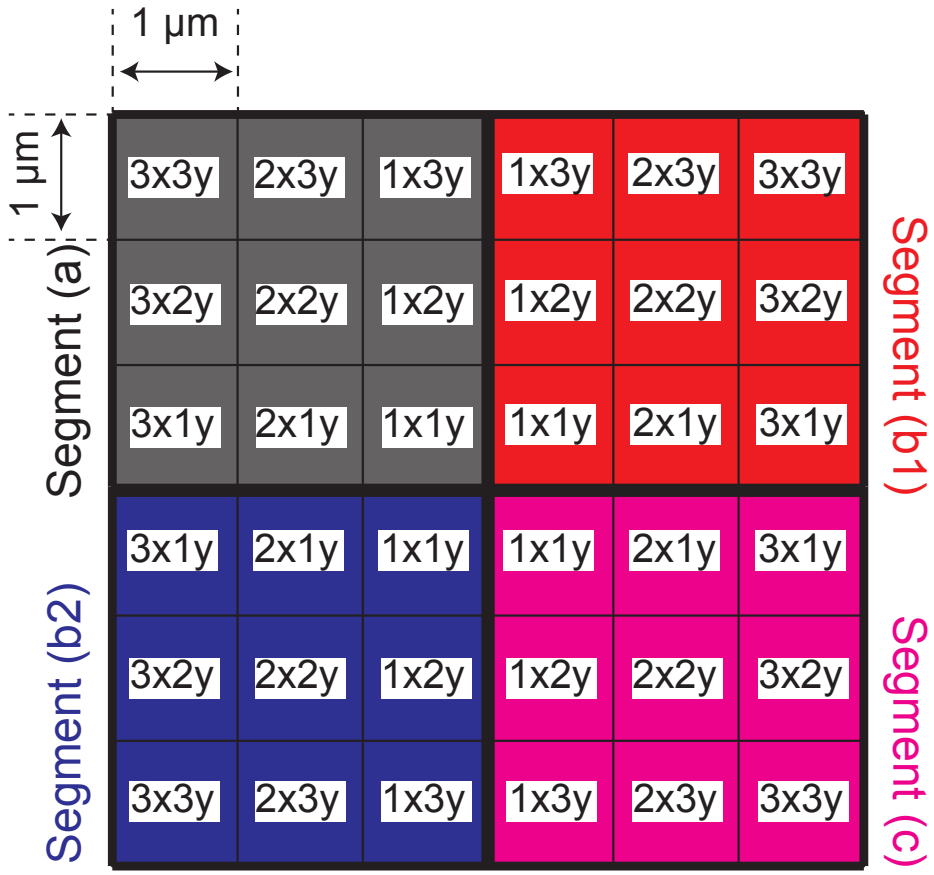

Figure 2.10: *9 areas of 1 × 1 µm on each of the four segments of a micronanostructure have been considered to conduct a detailed analysis of gold nanoparticle distribution. This method enables a precise study of the difference in interparticle spacing between the segments on one hand, and between different locations of the same segment on the other hand. The colors are codes for the segments within a quadruple structure.*

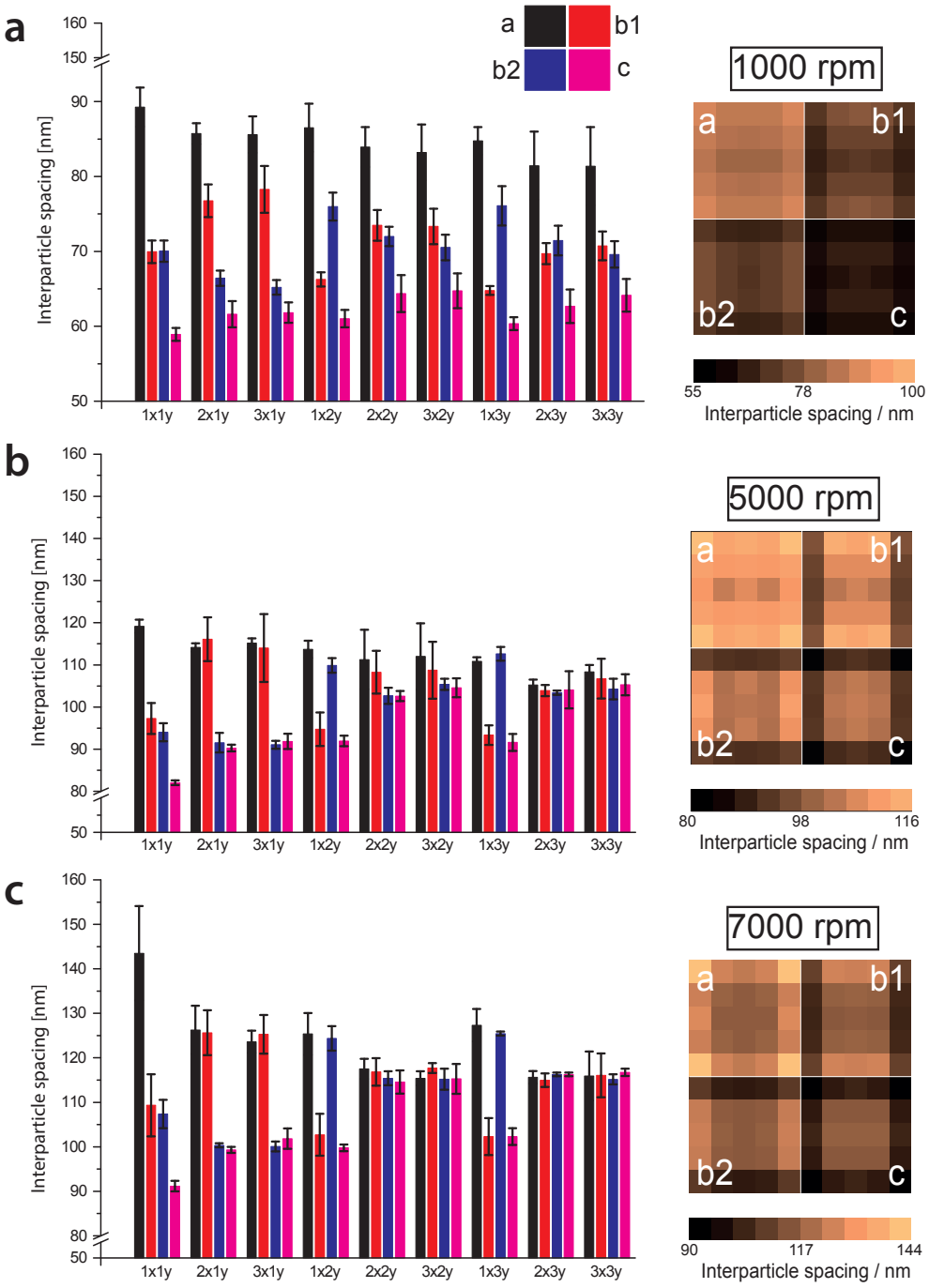

Figure 2.11: *Detailed analysis of interparticle spacings and their corresponding heat maps. The analysis demonstrate the regulation of nanoparticle spacing by both nanotopography and spin coating speed. Increasing the spin coating speed causes an overall increase in interparticle spacing. An almost homogeneous distribution of interparticle spacing within each segment can be seen at 1000 rpm (a). In contrast, at 5000 and 7000 rpm, the edge of the nanotopography dominates the regular self-assembly of the nanoparticles within the segments. A strong enrichment of particles and thus a smaller spacing are observed at the edges of lower segments. At higher spin coating speeds as in (b) and (c), the difference in interparticle spacing between the segments becomes less significant and eventually disappears the farther away from the segment's edge the considered spot is. The heat maps are reprinted by permission from the American Chemical Society: Langmuir*[164]*, copyright 2015.*

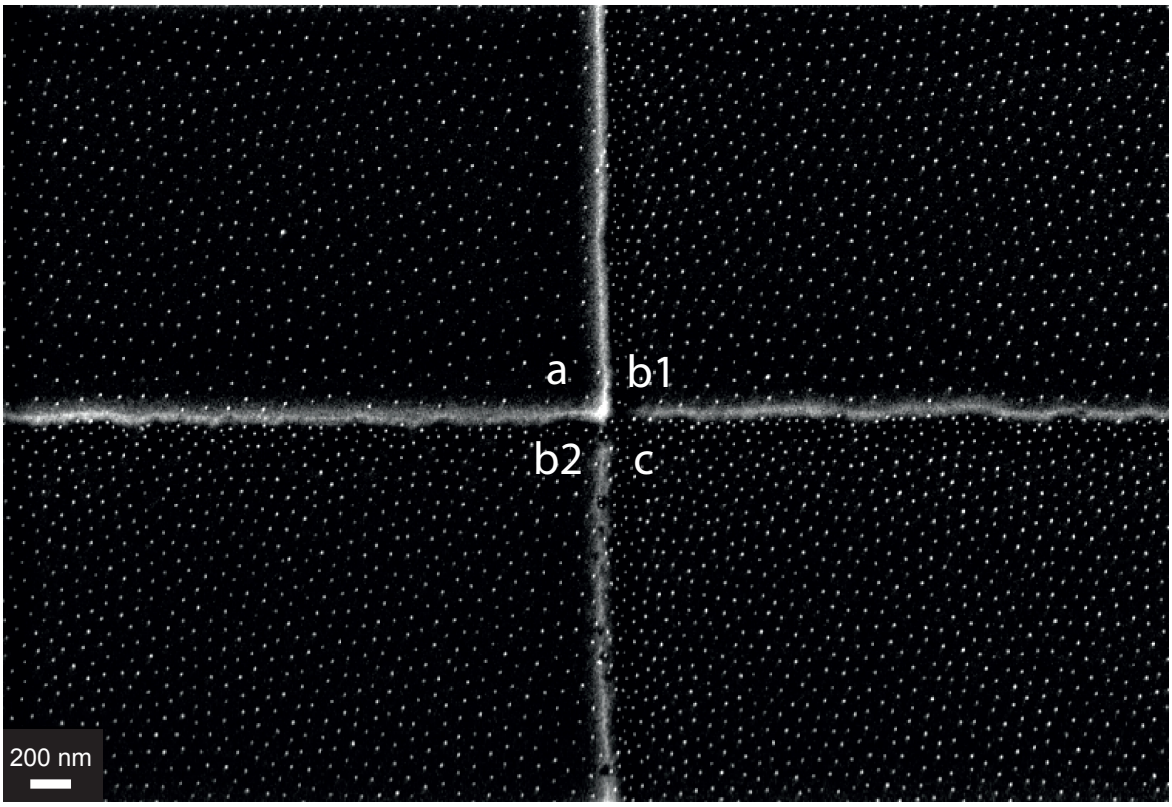

Figure 2.12: *Gold nanoparticles spin coated in a BCML process at 7000 rpm onto a Si nanotopographic substrate. An accumulation of particles appear near the edges of the quadruple's lower segments b1, b2 and c. Although this accumulation leads disruption of the hexagonal distribution of nanoparticles, this disordering is limited to a few hundred nanometers near the segment's edge. Reprinted by permission from the American Chemical Society: Langmuir*[164]*, copyright 2015.*

2.4.2 Improving the order parameter

Numerous applications require highly ordered patterns with constant interparticle spacing[173]. Periodic nanostructures offer a great variety in various applications such as density storage media[175], magnetic storage[176], solar cells and photodetectors[177]. Despite the high-throughput fabrication of particles offered by the BCML technique, a significant shortcoming of this method is represented by the structural defects that are reducible with optimized process parameters, but are still inevitable. These structural defects include fluctuating interparticle spacing and particle size to a certain extent, which compromises the complete structural monodispersity[178]. There have been many attempts to improve structural periodicity through post-preparation-process annealing. In the case of BCML, all these attempts depend on micelles' ability to rearrange due to their mobility when slightly detached from the substrate to which they adhere to. This occurs during exposure to heat[179,180], chemicals[181,182] and mechanical force[183]. However, despite the enhanced pattern order resulted through using these methods, it was reported that it may take from several hours to days in order to obtain the desired structure[181,182].

In this thesis, I followed a method suggested by Williges *et al.* in order to improve the hexagonal order of the gold nanoparticles. This method is based on self-organization of block copolymers through an additional subsequent annealing step that follows micellar deposition[173]. The strategy in this method is to apply a mechanical treatment using an ultrasound device as a fast and easy way of increasing nanoparticles order and thus mend structural defects. The longitudinal sound waves created by ultrasound caused the surrounding medium to repeatedly compress and decompress. During the period of reduced pressure, the medium's boiling point is lowered, leading to its evaporation in microbubbles. This results in a high-pressure wavefront that causes an implosion of these bubbles, producing pressure peaks, which are orders of magnitude larger than the standard pressure. The generated microshock waves compel micelles into a more equally distributed state. Therefore, a micelles-coated substrate is placed in a mixture of ethanol and clean water and then treated with ultrasound[173].

Fig. 2.13 shows the results of improving the order parameter of quasi-hexagonal gold nanoparticles prepared at 1000 rpm spin coating speed on micronanostructures. The order parameter measurements were taken for adjacent areas to segment edges, i.e. the 1 μm zones from the edges. Improving the order parameter of the gold nanoparticle distribution was undertaken using ultrasound annealing. The results

express a clear increase in order parameter for topographically-higher segments. The obtained values are analogous to previously reported ones for nanopatterns fabricated with BCML[184]. However, no improvement of order parameter can be seen on segment *c* due to small spacings between the gold nanoparticles on this segment. These results are in agreement with previous works that showed consistently lower order parameters for nanopatterns with small interparticle spacings[184].

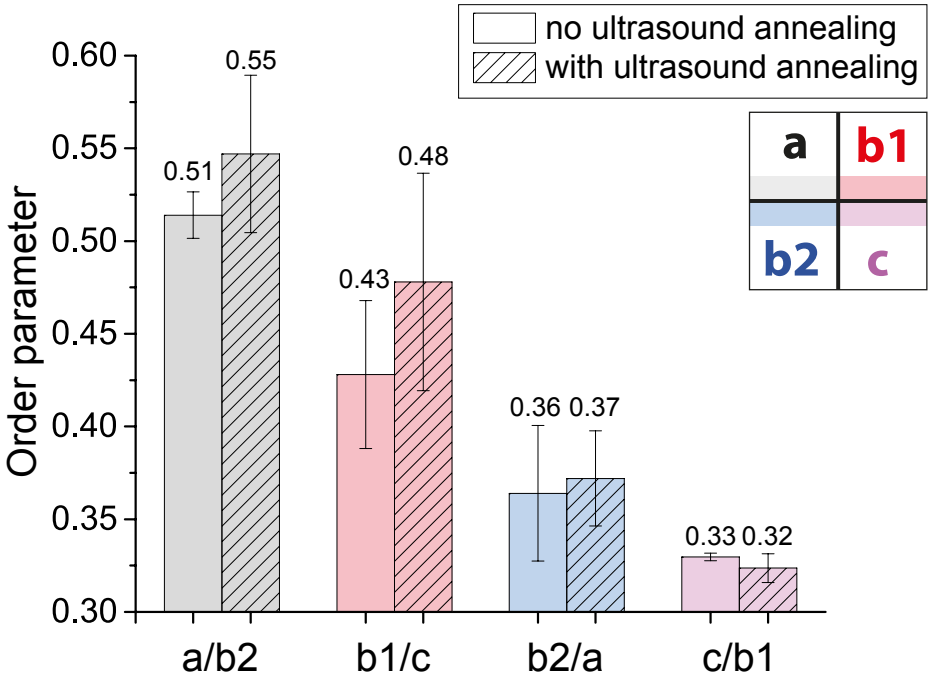

Figure 2.13: *Order parameter of the quasi-hexagonal nanoparticles on micronanostructures prepared at 1000 rpm spin coating speed. The order parameter measurements are for the areas adjacent to segments edges (the 1 µm zones from the edges). A clear improvement of order parameter can be seen for the topographically-high segments in response to ultrasound annealing. An increase in order parameter cannot be seen on segment c due to small spacings between particles on that segment. The inset demonstrates the color code used in the graph. Reprinted by permission from the American Chemical Society: Langmuir[164], copyright 2015.*

Furthermore, an improvement of order parameter was also obtained through ultrasound annealing in the central 2 × 2 µm area of the 5 × 5 µm segments. An increase of 4.5 % in order parameter on that 2 × 2 µm central area was seen on segment *a*. The order parameter increase on segments *b1* and *b2* were 3 and 2.5 %, respectively. However, there was again no notable improvement in order parameter on segment *c*.

2.4.3 Fluorescence microscopy for cells on topographical substrates

In order to examine cells' adhesion behavior on the micronanostructures presented in the chapter, standard fluorescence microscopy has been employed to image adhering cells on topographical substrates. The cells used for this experiment were REF52 YFP-pax (rat embryonic fibroblasts expressing YFP-paxillin). The preparation of cells for imaging was as follows: First, cell fixation was conducted using Para Formaldehyde (PFA) for 25 min followed by washing the sample with PBS buffer. Then, 0.1 % Triton X-100 was added and kept in incubation for 5 min in order to permeabilize the cells. Eventually, the Triton X-100 was removed and the sample was washed again with PBS. Finally, the cells were stained with the Alexa Fluor 555 phalloidin that enables visualizing the cell's cytoskeleton through the binding of phalloidin to the actin filaments. The staining is done by diluting 5 μl of the methanolic stock solution Alexa Fluor 555 phalloidin in 200 μl PBS, and then adding the diluted solution into the sample. The sample is lept for a 20 min incubation time at room temperature before washing with PBS. A stained adhering cell on a nanotopographic Si substrate is displayed in Fig. 2.14, which clearly shows that the surface topography does not hinder not restrain cells from developing a normal adhesion behavior.

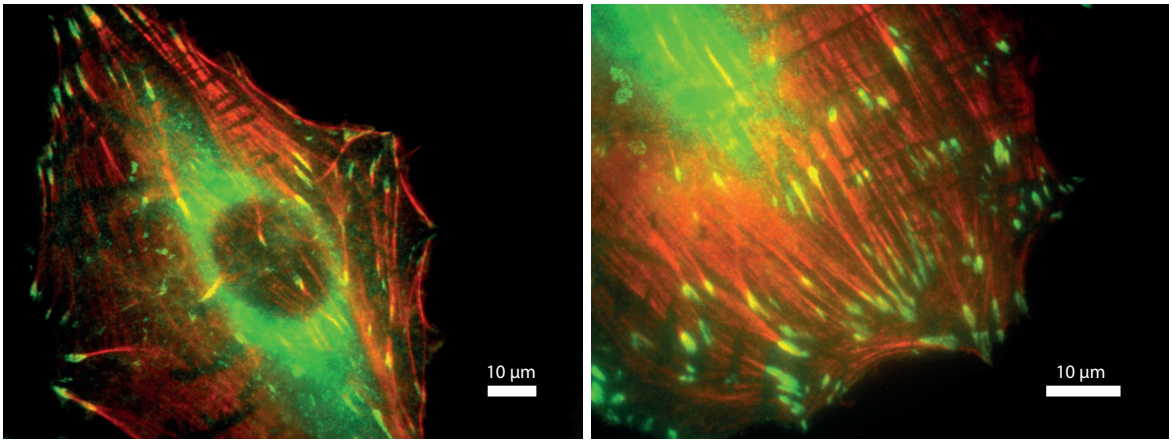

Figure 2.14: *Fluorescence microscopy of REF52 YFP cells on a nanotopographic substrate. The actin filaments stained with 555 phalloidin (red) and the YFP paxillin (green) are shown.*

2.4.4 Prospective

In initial attempts to apply BCML to metallic substrates, both magnesium and nickel titanium sputtered Si substrates were coated with gold nanoparticles. Despite the surface roughness of both samples, which impairs the regular quasi-hexagonal distribution of nanoparticles as reported previously[171,172], the gold nanoparticle arrays appear in a well-ordered status. Fig. 2.15 a and b show the gold nanoparticles on a Mg-coated Si substrate. Fig. 2.15 c displays the topographic condition of a NiTi substrate that had no noticeable influence on the gold nanoparticle distribution (Fig. 2.15 d), as it is with Mg-coated substrates.

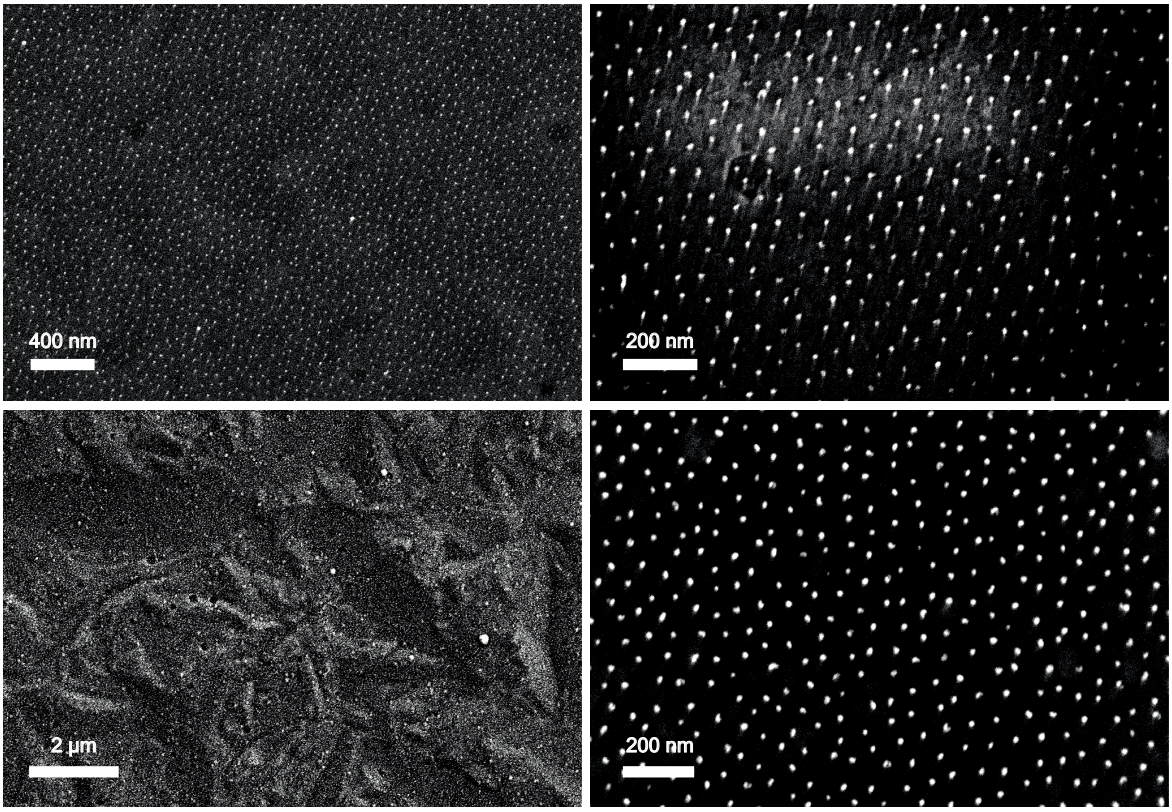

Figure 2.15: *Gold nanoparticle arrays on metallic substrates. (a) and (b) gold nanoparticles pattern spin coated on Mg substrates in a BCML process. (c) and (d) gold nanoparticles on NiTi substrates.*

Future work of BCML on metallic substrates is directed towards improving the biocompatibility of samples by enhancing cellular adhesion via surface nanostructuring.

2.5 Conclusion

In this chapter, I presented a novel self-assembly fabrication method for quasi-hexagonal patterns of gold nanoparticles with well-defined interparticle spacing on microstructured substrates using a combination of diblock copolymer micelle nanolithography and photolithography. Whereas it is known from previous works that nanoparticle structures can be regulated using substrates with topographical surfaces, the precise structure generated with such methods is difficult to control. On the contrary, the patterning method exhibited here combines the intriguing structural features of BCML with nanotopography-controlled arrangement, leading to hexagonally ordered micronanostructures by pure self-assembly. Hence, this strategy provides a high-throughput method to control the density and spacing of nanoparticles in micrometer-sized segments. The driving force for the observed topographic height-dependent interparticle spacing is attributed to immersion forces and steric interactions acting on the micelles during solvent evaporation. Moreover, the nanopatterns generated using this method show similar chemical contrast to conventional nanoparticle arrays created with BCML on flat substrates, thus standard protocols for coupling functional molecules to the gold nanoparticles can be utilized. Since BCML is compatible with various substrates types and the etching of regular nanotopographies has become a routine technique, a straightforward transfer of this surface-coating strategy to substrates other than SiO_2 wafers is now feasible.

Chapter 3

Rapid and Reversible Photoswitching of Cell Adhesion

3.1 Introduction

In this chapter, I present the work that was carried out to achieve a light-induced reversible switching of cell adhesion using c(RGDfK)-functionalized azobenzene [1]. Switching cell adhesion with light has become very attractive, as it allows both rapid [185] and localized switching of cell adhesion [186] on biointerfaces. To be of practical use, photoswitchable materials should allow for reversible and rapid switching at minimum light exposure, while at the same time ensuring that the binding of specific cell adhesion molecules is switched. The model demonstrated in this chapter is a versatile approach to achieve rapid reversible photoswitching of cell adhesion at illumination times of a few tens of seconds. The switching is attained by using azobenzenes biofunctionalized with c(RGDfK) peptides and covalently immobilized on glass surfaces. The azobenzenes were incorporated into a biologically inert monolayer of polyethylene glycol (PEG) [187]. C(RGDfK) peptides are ligands with high affinity for the cellular adhesion receptors integrin $\alpha_\nu\beta_3$ and $\alpha_\nu\beta_5$, thus promoting the adhesion of many cell types [188]. Upon UV illumination, the thermally stable azobenzene *trans* isomer switches to its *cis* configuration so that the c(RGDfK) is immersed into the PEG background. After subsequent illumination with visible light, the azobenzene switches back to the *trans* isomer and the c(RGDfK) ligand is again available for integrin binding.

[1] Part of this work is published in Kadem *et al.*, *Advanced Materials* [185], 2016.

The photoswitching of integrin-mediated cell adhesion on those substrates will be demonstrated using both cell culture studies and also single-cell measurements of cell adhesion behavior in several consecutive switching cycles.

3.2 Azobenzene-based photoswitchable interfaces

In an attempt to design biointerfaces with photoswitchable c(RGDfK) (cyclic - Arginine Glycine Aspartate) functionalities for controlling specific integrin-mediated cell adhesion, a mixed monolayer of c(RGDfK)-functionalized azobenzenes and polyethylene glycol (PEG2000) has been prepared (Fig. 3.1 a). The synthesis of the c(RGDfK)-azobenzenes and the preparation of the switchable interfaces have been kindly performed by Dr. Michelle Holz and Grace Suana in the group of Prof. Rainer Herges at Otto Diels Institute of Organic Chemistry at Christian-Albrechts-Universitt zu Kiel. PEG2000 inhibits nonspecific protein and cell interactions with the surface while c(RGDfK) mediates integrin-mediated specific cell binding. The molar ratio of c(RGDfK)-azobenzene and PEG2000 was adjusted to 1:99, which has recently been reported to offer adequate adhesion conditions for fibroblast cells[189]. This ratio corresponds to a c(RGDfK)-azobenzene packing density of around 0.5 molecules/nm^2, as determined with UV/Vis spectroscopy. Fig. 3.1 b illustrates the working hypothesis for switching of the mixed c(RGDfK)-azobenzene/PEG2000 monolayer. Irradiation with monochromatic UV light with a wavelength of 365 nm causes photoswitching of the surface properties, as the azobenzenes change their configuration from *trans* to *cis*, even at short illumination times of 20 s (Fig. 3.1 c). In consequence the c(RGDfK) headgroup is forced to dip into the non-adhesive PEG2000 background. Illumination with 440 nm visible light switches the azobenzenes back into their *trans* configuration, making the c(RGDfK) again available for cell adhesion. This process is reversible, as demonstrated by UV/Vis spectroscopy (Fig. 3.1 c). Comparing the UV/Vis spectra before and after illumination with 365 nm and assuming that the *cis* isomer does not absorb at the π-π^* transition (λ = 359.6 nm), shows that about 47 % of azobenzene molecules in average are switched into *cis* configuration, as determined from four independent experiments.

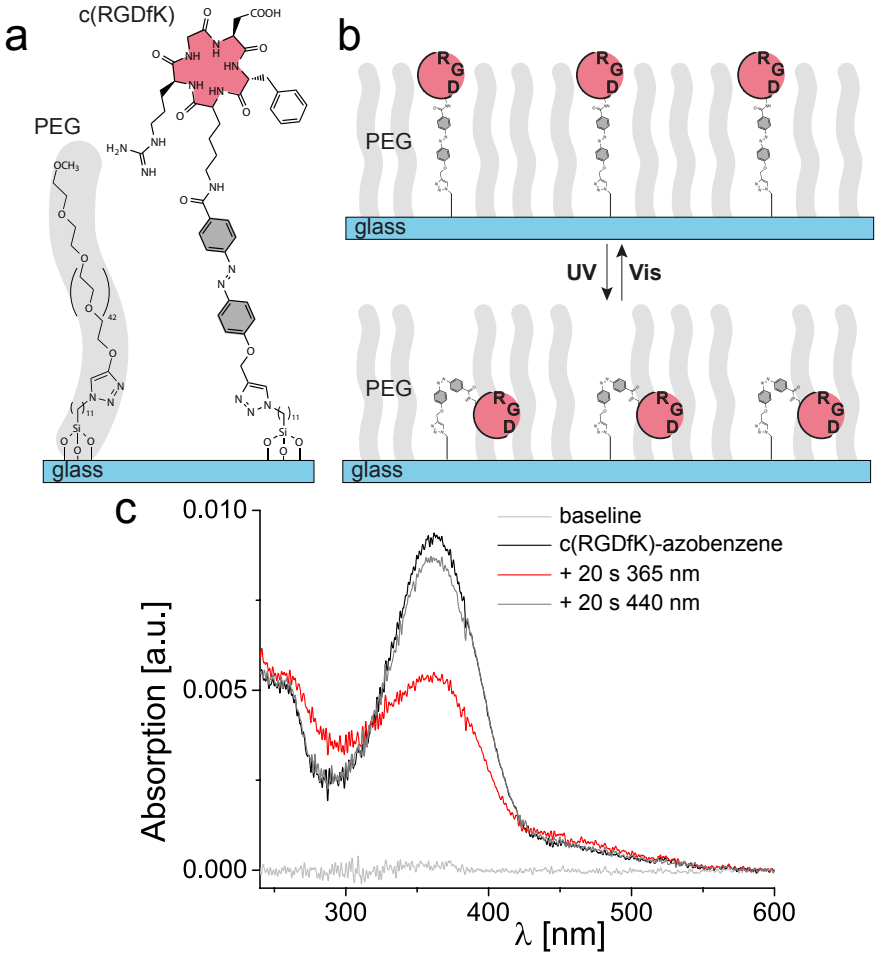

Figure 3.1: *(a) Structure of the c(RGDfK)-azobenzene and its covalent immobilization on glass. (b) Illustration of the photoswitchable c(RGDfK) surfaces. The glass surface is functionalized with a mixed monolayer of polyethylene glycol (PEG) and c(RGDfK)-azobenzenes. In response to UV illumination, the azobenzene changes its configuration from the trans to the cis isomer and the c(RGDfK) headgroup is immersed into the non-adhesive PEG background. (c) UV/Vis spectra demonstrating the reversible photoswitching of a mixed monolayer of PEG and c(RGDfK)-Azo-[N3] on quartz. (a) and (b) are modified from Kadem et al.*[185]*. (c) is reprinted by permission from the Wiley-VCH: Advance Materials*[185]*, copyright 2016.*

In recent years, different strategies for preparation of switchable azobenzene surfaces have been developed, including self-assembled monolayers[190], the triazatriangulenium (TATA) platform[191], and polyelectrolyte multilayers[149]. Thiol-based self-assembled monolayers often do not provide enough free volume for functional groups to switch, a limitation that has been overcome by employing TATA-platforms. Still, both surface functionalization strategies require the usage of gold or silver surfaces, thus limiting their applicability. In order to generate a widely applicable surface coating, a covalent binding approach based on surface silanization was chosen, which leads to stable self-

assembled monolayers[192]. During surface coating, first a coupling layer is generated that allows further functionalization with click-chemistry. This surface coating strategy can be applied to many different biomaterial types, including Ti and NiTi[193].

Cell adhesion assays using fibroblast cells (REF52 wt - Rat Embryonic Fibroblasts) have been performed by Dr. Qian Li to demonstrate and asses the capability of the c(RGDfK)-azobenzene surfaces to switch cell adhesion[185]. In these experiments, cells were seeded onto sterilized azobenzene surfaces that were either stored in the dark (*trans* configuration) or illuminated with UV light of 365 nm (*cis* configuration). After 15 min, the samples were gently rinsed with buffer solution to remove loosely bound or floating cells and then the number of adherent cells was determined (Fig. 3.2 a). The results showed a dramatic reduction in adherent cells of about 50 % on surfaces with c(RGDfK)-azobenzene in *cis* configuration compared to surfaces where the c(RGDfK)-azobenzene was in *trans* configuration (Fig. 3.2 b). This efficiency of cell adhesion switching is also evident from the phase contrast images shown in Fig. 3.2 c and Fig. 3.2 d[185].

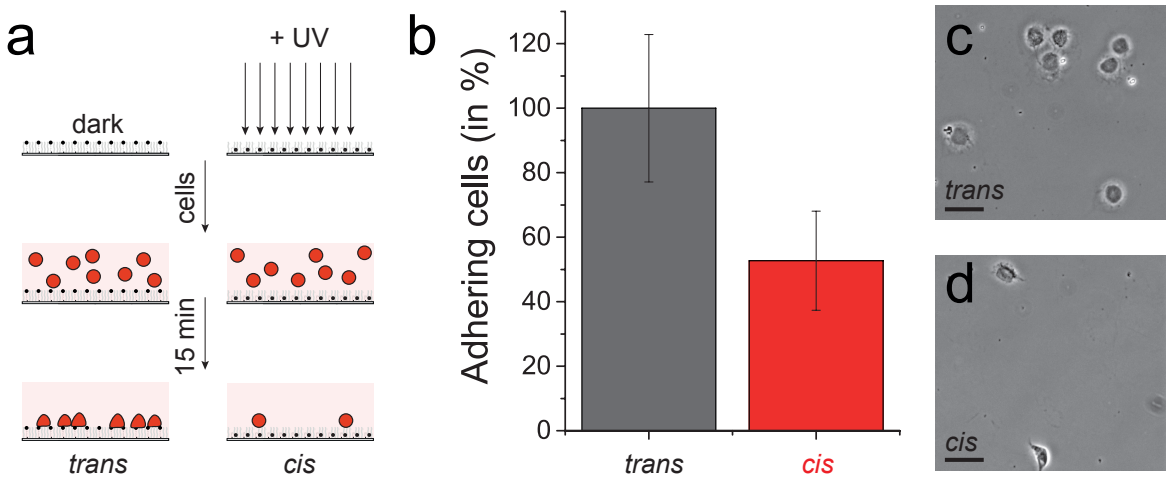

Figure 3.2: *(a) Schematic illustration of the cell culture assay used for the photoswitching test. Cells were seeded onto substrates that were either stored in the dark (trans) or illuminated with UV light (cis). After 15 min, the number of adhering cells was determined. (b) In the cell culture experiments, the adhesion of fibroblast cells to the c(RGDfK)-azobenzene surfaces was shown to significantly reduce to about 50 % when in the cis configuration compared to the trans configuration. Error bars denote standard deviation. (c) Phase contrast image of cells after 15 min adhesion on a surface in the trans configuration and (d) in the cis configuration. Scale bars: 50 µm. Reprinted by permission from the Wiley-VCH: Advance Materials[185], copyright 2016.*

In order to study the switching effect in greater detail at the single-cell level, SCFS experiments have been performed, as discussed in section 3.3. Moreover, cell confor-

mation was tested in response to repeated UV exposure. REF52 wt cells were cultured on a glass substrate for a few hours prior to irradiation (Fig. 3.3 a). The cells were then irradiated with 365 nm for 30 s (Fig. 3.3 b) followed by another 30 s exposure with 440 nm (Fig. 3.3 c). No notable change in the conformation of cells could be observed[185].

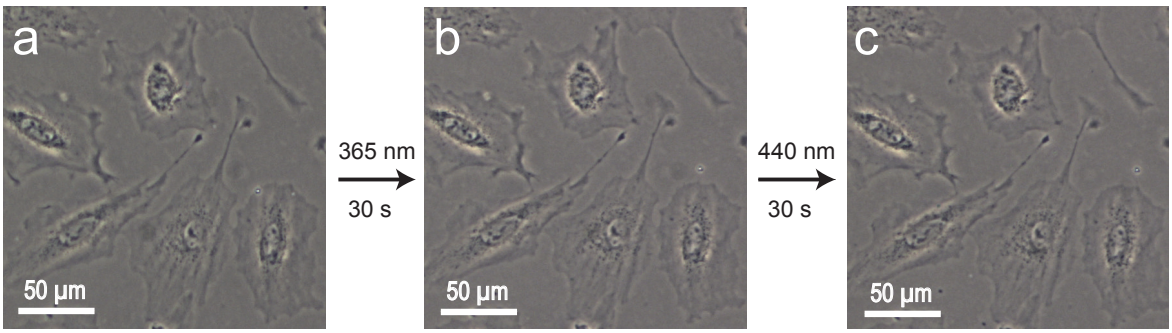

Figure 3.3: *Cell conformation response to UV exposure. (a) REF52 wt cells on a glass substrate prior to irradiation. (b) Cells after 30 s exposure to UV light with 365 nm. (c) Cells after 30 s exposure to UV light with 440 nm. No notable change in cell conformation can be seen. Reprinted by permission from the Wiley-VCH: Advance Materials[185], copyright 2016.*

The results of the cell culture assay used for demonstrating photoswitchable adhesion confirm efficient cell adhesion switching at considerably shorter UV illumination times of only a few tens of seconds compared to previous studies where at least one hour of UV illumination was required to obtain similar results[148–150].

3.3 Single-cell force spectroscopy on switchable substrates

3.3.1 Cell adhesion measurements

For quantitatively assessing cell adhesion switching at the level of individual cells, Single-Cell Force Spectroscopy (SCFS) was employed. This technique is an atomic force microscopy (AFM) based method for characterizing cell adhesion by measuring cell detachment forces[3]. Cell detachment forces can be determined with piconewton (pN) and nanonewton (nN) resolution at the single cell and single molecule level. Furthermore, cell adhesion can repeatedly be tested *in situ* with the same single cell, thus avoiding experimental errors from surface inhomogeneity and from cell-to-cell

variations. This presents a considerable advantage over cell culture assays, which typically only represent ensemble measurements that merely yield averaged results. Here, the excellent potential of SCFS is both the capacity to directly quantify the detachment forces of cells even at sub-second timescales, and the possibility to quantitatively demonstrate the true reversibility of photoswitching *in situ* on the single-cell level, thus avoiding statistical ensemble differences.

SCFS experiments were carried out in physiological buffer using live REF52 wt cells. The buffer used in the SCFS experiments was the Hank's balanced salt solution (HBSS). Like other buffers such as phosphate buffered saline (PBS), the HBSS is also a balanced salt solution that provide cells with water and inorganic ions as well as maintaining a physiological pH and an osmotic pressure. Both buffers are isotonic solutions whose salinities resemble that of the human body and thus makes cells stable during an experiment. However, unlike PBS, HBSS also contains glucose that assists keeping cells alive and in a good condition for longer times. The HBSS used in this work contains sodium bicarbonate, but does not contain phenol red (a pH indicator), calcium chloride nor magnesium sulfate to avoid affecting the azobenzene molecules. Nonetheless, this buffer provides cells with a sufficient amount of salt ions to balance the amount of water inside the cell. Maintaining the correct amount of salt ions in solution assists preserving cells in their natural state and thus prevents cell shrinkage or bursting.

Fig. 3.4 a depicts the setup for measuring cell detachment forces. The measurements were carried out with an AFM mounted on an inverted light microscope using tipless cantilevers that were calibrated using the thermal noise method (implemented in the JPK AFM software and will be discussed in detail in Appendix B.1.4) and were functionalized with Concanavalin A (conA) according to standard procedures[3,115,194].

In order to attach a single REF52 wt cell to the free end of a cantilever, a small number of freshly trypsinized cells was injected into the sample chamber. Immediately, the cantilever was approached to a cell up to a contact force of a few nN and held at constant force for about 8 s, followed by careful lift-off from the surface and a 12 min resting time. This procedure ensures stable attachment of the cell to the cantilever[3,115,194]. The cell was then repeatedly brought into contact with and retracted from the c(RGDfK)-azobenzene surface. The cantilever deflection is directly proportional to the force acting on the cell and is typically plotted against the distance of the cantilever from the surface as shown in Fig. 3.4 b (a detailed description of SCFS can be found in section 1.5.2).

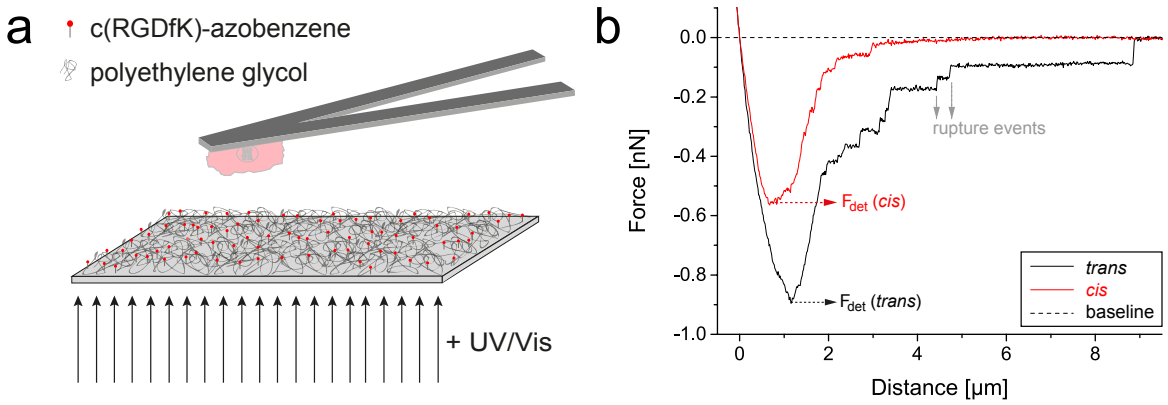

Figure 3.4: *Single-cell force microscopy experiments on azobenzene-coated surfaces. (a) Sketch of the AFM cell adhesion experiment. The cell is attached to the free end of a tipless cantilever in an AFM device and brought into contact with a c(RGDfK)-azobenzene surface, which is photoswitched by illumination from below. (b) Representative force curves for a cell detached from a c(RGDfK)-azobenzene surface in cis and trans state. The cell detachment force, F_det, is defined as the force needed to initiate cell detachment, i.e. corresponds to the minimum of the force curves (red, black arrows). Single rupture events are derived from distinct rupture events in the force curve (grey arrows). Reprinted by permission from the Wiley-VCH: Advance Materials*[185]*, copyright 2016.*

Force-distance curves were recorded for an approach/retract speed of 30 μm/s and the contact between cell and surface was held at a contact force of 500 pN for both 1 and 3 s cell-substrate contact time experiments. For each azobenzene configuration, 20 force curves were taken at four different positions defined by the vertices of a 10 $\times$ 10 μm square. For switching between isomeric configurations, the cell was retracted from the surface and the surface was illuminated for 30 s from below using an LED combination mounted on objective slots. Each irradiation period was followed by a waiting period of 3 min before commencing force-distance measurement cycles. A single cell was employed for at least two complete switching cycles, where a cycle implies switching from *trans* to *cis* and back to *trans* isomerization.

Fig. 3.4 b shows the retract segment of representative force curves for a cell adhering to a substrate in *trans* (black) and *cis* (red) configuration, respectively. At a certain time during the cantilever retraction course, the pulling force reaches a critical value termed the cell detachment force (F_{det} in Fig. 3.4 b), at which the cell starts to successively detach from the substrate. Under continued force load during cantilever retraction, individual cell-substrate bonds dissociate (rupture events in Fig. 3.4 b) until the cell is completely detached from the substrate. These rupture events show that specific molecular bonds are formed between the cell and the surface. For the assess-

ment of cell adhesion as a function of the isomeric state of the c(RGDfK)-azobenzene layer, cell detachment forces as well as the number of single rupture events in individual force curves are key parameters for a quantitative and qualitative comparison. Whereas cell detachment forces characterize adhesion at the level of the whole cell, the number of single rupture events gives information about the number of molecular bonds formed between the cell and the surface, thus giving information about the number of available binding sites on the surface. As shown in Fig. 3.4 b, detachment forces as well as the number of successive single rupture events after 1 s cell-surface contact time are noticeably decreased for the *cis* configuration compared to the *trans* configuration.

3.3.2 Reversible photoswitching of cell adhesion

In order to demonstrate reversible photoswitching of cell detachment forces, we carried out several cycles of UV/Vis irradiation *in situ* during SCFS. Commencing with c(RGDfK)-azobenzenes in the *trans* configuration, 20 force curves were taken at four different positions on the substrate with 1 s contact time. Then, the cell was lifted from the surface and the azobenzenes were switched into the *cis* configuration by irradiation with 365 nm UV light from below for 30 s. Another 20 curves were recorded at the same positions as before and the azobenzenes were photoswitched back into the *trans* configuration by irradiation with light of 470 nm wavelength for the next set of force curves. This switching cycle was repeated several times with the same cell, and detachment forces and number of rupture events per individual force curve were analyzed.

Fig. 3.5 shows the detachment force results (normalized values) of representative *in situ* cell adhesion photoswitching SCFS experiments with 1 s cell-substrate contact time. In addition to the 1 s contact time experiments, 3 s adhesion time experiments on azobenzene-coated substrates were conducted. These experiments showed that the cell detachment force demonstrates a similar trend to that observed for 1 s adhesion time experiments, i.e. stronger cell adhesion on azobenzene in the *trans* configuration than on the *cis*. The results of those experiments are shown in Fig. 3.5, which displays the results from the first switching cycle. More switching cycles were not feasible because the cell was not able to survive further force measuring rounds due to repeated loading for a relatively long contact time. In order to examine the influence of UV exposure on the surface properties of glass and whether it affects the strength of adhesion of cells

on it, a control SCFS experiment was carried out. The experiment was performed on a blank glass substrate with a 1 s cell-sample contact time. More than 80 force-distance curves were first recorded after exposure with 365 nm for 30 s. Subsequently, a similar number of measurements were taken after exposure with 440 nm for 30 s. The results show no difference in detachment force between the two conditions as can be seen in Fig. 3.5.

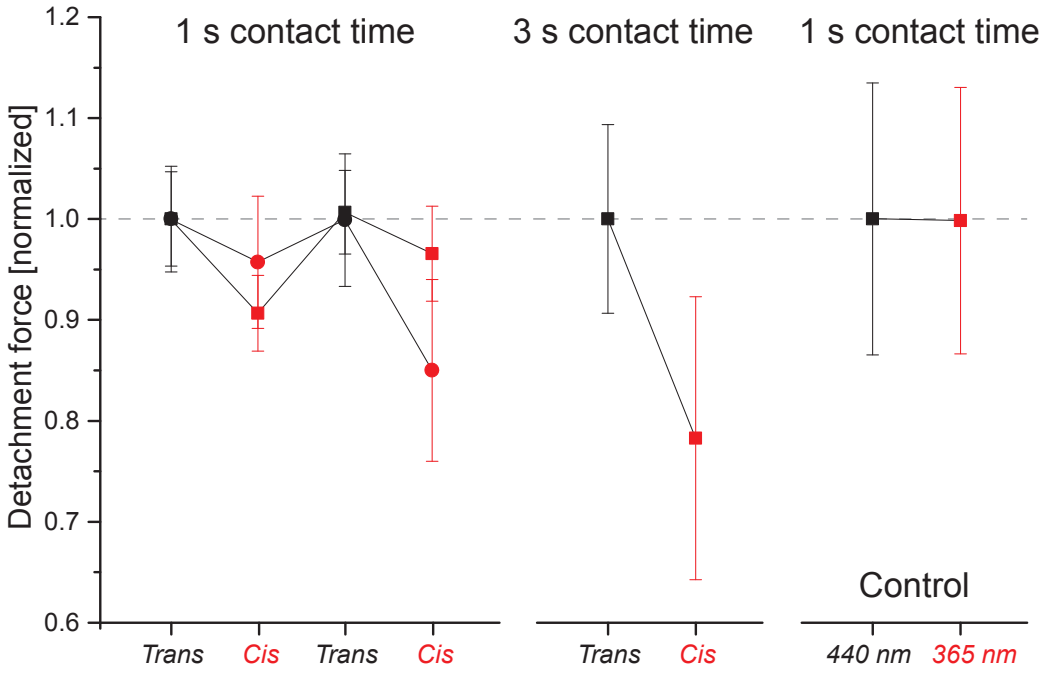

Figure 3.5: *Switching of cell-detachment forces (normalized values) measured at 1 s and 3 s cell-substrate contact times in SCFS experiments. A SCFS experiment on blank glass as a control experiment is also shown. The latter was performed at 1 s contact time after irradiation with 400 nm and 365 nm, where ≥80 force-distance curves were recorded for each situation, and no difference in the detachment force can be seen. In 1 s contact time experiments, each data point is the average of ≥20 force curves recorded on c(RGDfK)-azobenzene coated surfaces. Cell detachment forces are different in the cis and trans configurations of the c(RGDfK)-azobenzene and can be reversibly switched in two consecutive switching cycles. As in 1 s contact time, a clear difference in the detachment force can be seen between the trans and the cis configurations in the first switching cycle for a 3 s contact-time experiment. Performing further switching cycles was not feasible due to cell failure.*

The cell detachment force values for a representative *in situ* cell adhesion photoswitching SCFS experiments with 1 s cell-substrate contact time is shown in Fig. 3.6 a. For azobenzenes in the *trans* configuration, the average cell detachment force ranged between $F_{det} = (0.74 \pm 0.03)$ nN before any illumination and $F_{det} = (0.92 \pm 0.04)$ nN in the final switching cycle with a mean of $F_{det} = (0.83 \pm 0.04)$ nN. In the *cis* state, the average detachment force was significantly decreased to $F_{det} = (0.65 \pm 0.03)$ nN,

corresponding to a reduction by more than 20 % (Fig. 3.6 a). The analysis of the SCFS experiments on 5 independent cells have shown that the mean cell detachment forces in the *cis* and *trans* state are significantly different at the 0.001 level (one-tail independent sample t test (discussed in detail in Appendix A.1), number of forces curves: 1186 (*trans*) and 796 (*cis*)). Consistently, the number of rupture events per force curve was reduced for surfaces with azobenzenes in *cis* configuration, demonstrating that fewer binding sites are available if azobenzenes were in *cis* configuration and that single molecular binding to surfaces can be controlled by photoswitching. The results of the analysis of rupture events for the data set shown in Fig. 3.6 a is displayed in Fig. 3.6 b).

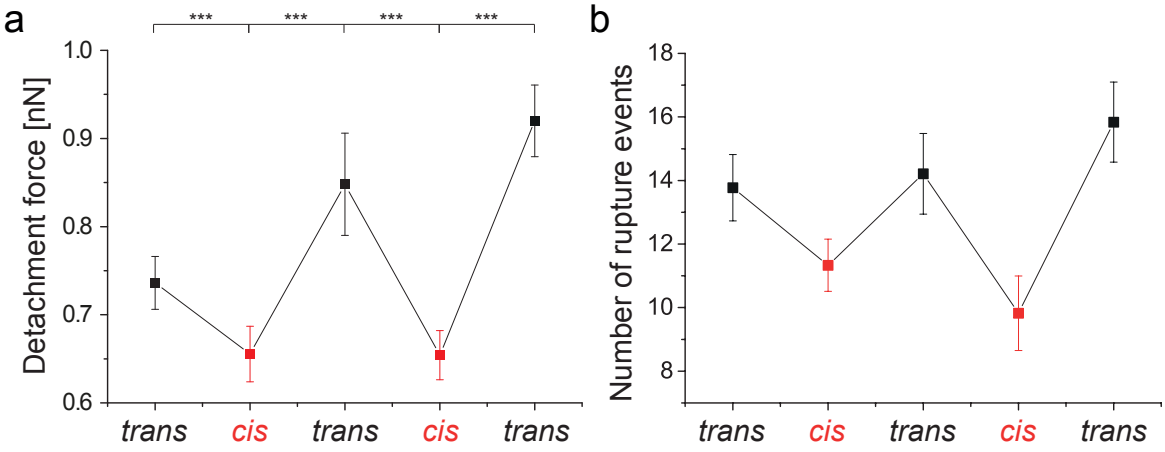

Figure 3.6: *(a) Switching of cell-detachment forces of a single cell measured at 1 s cell-substrate contact time in a SCFS experiment. Each datapoint is the average of >76 force curves from four different locations on the c(RGDfK)-azobenzene surface. Cell detachment forces are different in the cis and trans configurations of the c(RGDfK)-azobenzene and can be reversibly switched in several consecutive switching cycles. (b) A change in the number of rupture events per force curve due to the cis/trans isomerization of the c(RGDfK)-azobenzene for the experiment shown in (a). Error bars: Standard deviation. Reprinted by permission from the Wiley-VCH: Advance Materials*[185]*, copyright 2016.*

Moreover, in order to measure the work needed to achieve a complete detachment of the cell from the substrate, the detachment energy was measured. Fig. 3.7 shows that the energy needed to detach the cell from the substrate is larger when the azobenzene is in the *trans* state. This behavior can be seen in both 1 and 3 s adhesion time SCFS experiments. Fig. 3.7 also demonstrates that the energy needed to detach the cell from the substrate is larger for 3 s adhesion experiments compared to 1 s experiments.

Exploiting the excellent potential of SCFS to quantify photoswitching at the single-cell level, I compared three easily accessible parameters, the force, the energy and the

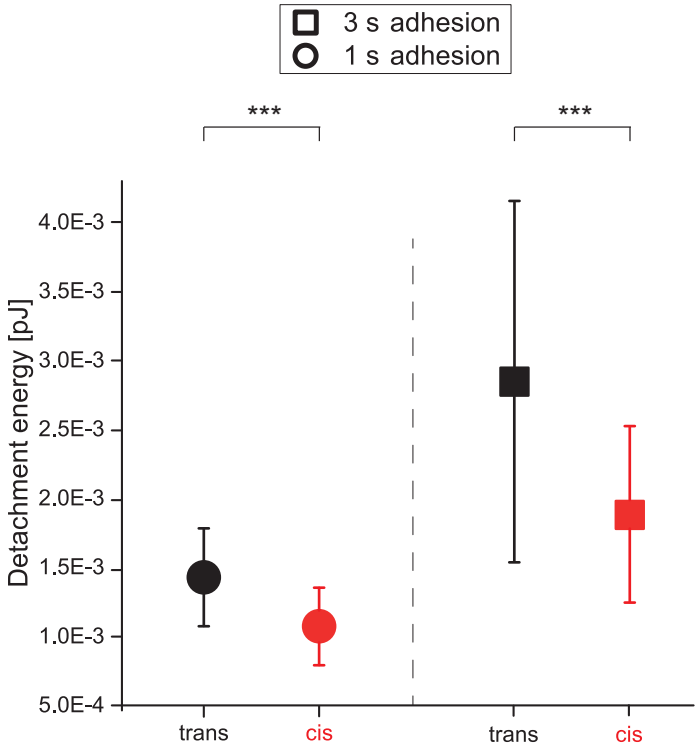

Figure 3.7: *Cell detachment energy for both 1 (left of dashed line) and 3 (right of dashed line) s cell-substrate contact time. The detachment energy at both contact times is larger at the trans configuration compared to the cis.*

number of individual rupture events needed to detach a single cell from the surface. Cell adhesion was significantly hampered with c(RGDfK) azobenzenes in *cis* configuration as indicated by a drastically reduced cell detachment force and consistently fewer individual rupture events.

Moreover, repeated back and forth switching between isomeric states within one experiment was performed, demonstrating the true reversibility of surface functionality. Here, it is important to mention that cell detachment forces did not continually decrease during the consecutive switching cycles, proving the stable binding of the c(RGDfK)-azobenzenes to the surface.

However, our measurements of cellular detachment forces and particularly the analysis of single rupture events also show that cell adhesion, though significantly reduced, was not switched to zero in response to *cis-trans* isomerization. This result might be caused to a small extent by unspecific background adhesion to the polyethylene glycol background[115]. The major reason for this observation is presumably caused by the incomplete switching of the c(RGDfK)-azobenzene layer, which is about 50 % as determined by UV/Vis. This is highly consistent with our cell culture assays, which

have shown that the number of adhering cells was reduced by 50 % for surfaces in the *cis* configuration compared to the *trans* configuration.

Single cellular focal adhesion sites react very sensitively to variations in local ligand density and experience a complete turnover of participating molecules within only 15 min[85,131]. Furthermore, in myogenic differentiation a temporally controlled variation of ligand density has strong impact[125]. Hence, a strong impact on cell adhesion due to any photoswitching-caused differences in ligand presentation can be anticipated either locally or globally. This aspect will be subject to future investigation. Furthermore, it has become increasingly evident that temporal changes in ligand presentation influence a variety of cellular properties that are not limited to cell adhesion[125,126]. With regard to such effects, this strategy to generate rapid and reversible integrin-mediated photoswitching holds significant potentials for *in vitro* and *in vivo* applications, particularly in order to control cellular behavior by temporal and spatial control of cell adhesion.

3.4 Conclusion

In this work, a controlled, rapid and reversible photoswitching of integrin-mediated cell adhesion has been successfully achieved using a powerful and widely-applicable surface functionalization strategy based on c(RGDfK)-functionalized azobenzene monolayers. Photoswitching of cell adhesion was investigated in cell culture assays and by measuring cell detachment forces at the single-cell level. This study provided an illustration of the photoswitching mechanism at both cellular and molecular scales and also allowed an unprecedented dynamic control of cell adhesion. Detailed analysis of cell detachment curves revealed that cell adhesion can be reversibly switched at the single-cell level and that fewer individual rupture events between cell and surface are detected when the surface is in *cis* configuration. This indicates that indeed fewer cell adhesion ligands are available for binding on the surfaces due to isomerization of the c(RGDfK)-functionalized azobenzene molecules. The surface coating strategy presented here can be easily applied to many different metallic materials that contain a silanizable oxide layer, including biomedically relevant implant materials such as Ti and NiTi. This model is an important stepping stone towards greater development of a novel class of photoswitchable biointerfaces that enables a flexible and reversible control of cell adhesion for a variety of *in vitro* and *in vivo* applications.

Chapter 4

Light-triggered mechanical stimulation of integrin-mediated adhesion

4.1 Introduction

Cells are able to sense[57,195] and actively react to the mechanical properties of their environment through a dynamic restructuring of adhesion sites[45,196,197]. Those mechanical forces are essential for determining cell functionality and tissue formation[198]. The ability of cells to adapt to environmental changes via modifying the cellular adhesion machinery implies that cell adhesion is a highly dynamic process[117,118]. However, despite the extensive research conducted to shed light on the mechanism of cellular mechanosensing, the experimental settings that have been used are dominantly limited to providing a static control of cell adhesion. In this chapter, a novel and intriguing strategy for a reversible control of cell adhesion at the molecular level is presented. This new approach is based on using c(RGDfK) ligands coupled to photoactive push-pull azobenzenes, which can be stimulated by visible light. Azobenzenes and spiropyranes have been previously employed in a few attempts to achieve switchable cell adhesion, as both of their configurations can be switched between two well-defined isomeric states using two different wavelengths[148,185,186]. Nevertheless, the inconvenience that both of these molecules have to put up with is the necessity for two wavelengths to complete a two-way switching. Using two different wavelengths in a biological system can induce complications due to the exposure to a wider, possibly undesirable, range of the electromagnetic spectrum. The shortcoming in these rather "conservative approaches" can be overcome by using the push-pull type of azobenzenes that are excellent alter-

natives to regular azobenzenes, as they could be reversibly set between an "active" and an "inactive" state with a single wavelength within the visible spectrum. Active is a state of rapid (millisecond) trans/cis switching of the push-pull azobenzene that takes place during exposure to a 530 nm light, which leads to an oscillation of the c(RGDfK) ligands. This oscillation is seized once the light is switched off and thus the inactive state is resumed. In this work, I show that the light-triggered mechanical oscillations of single integrin ligands modulate cell adhesion and gene expression of focal adhesion cluster proteins. The results exhibit a remarkable reinforcement of cell adhesion due to the oscillation of the c(RGDfK) ligands. Likewise, the results also shows that the expression of genes associated with mechanosensing and focal adhesion formation, such as talin, vinculin, zyxin and paxilin, is upregulated in response to the oscillation. This study is a significant milestone in understanding the regulation of cellular mechanosensory mechanisms by molecular-scale forces.

4.2 Photo-responsive interfaces

In this study, the push-pull azobenzenes were first covalently coupled to glass substrates along with a biologically passive polyethylene glycol (PEG) layer, then the molecules were functionalized with the integrin ligand c(RGDfK)[188] (Fig. 4.1 a). The synthesis of the c(RGDfK)-azobenzenes and the preparation of the interfaces have been kindly performed by Dr. Michelle Holz and Grace Suana in the group of Prof. Rainer Herges at Otto Diels Institute of Organic Chemistry at Christian-Albrechts-Universitt zu Kiel. The molar ratio of c(RGDfK)-azobenzene and PEG2000 was set to 1:99, which is identical to that used in Chapter 3 to perform a reversible switching of cell adhesion. This molar ration has been reported to be adequate for providing a suitable adhesion condition for fibroblasts[185,189]. The c(RGDfK)-azobenzene packing density on such substrates was about 1.07 ± 0.33 molecules/nm^2, which is twice as dense as the c(RGDfK)-azobenzene used in Chapter 3, as determined with UV/Vis spectroscopy. Fig. 4.1 b illustrates the working principle of the c(RGDfK)-coupled push-pull azobenzene monolayer. The azobenzene remains in the *trans* configuration as long as the light is switched off. Once the 530 nm light is turned on, the azobenzene molecules start oscillating between the two isomeric states. As shown in the work of Hugel *et al.*, azobenzene is capable of switching back and forth between the two isomeric states under an externally applied force[199]. Azobenzenes can still change their configuration from *trans* to *cis* while withstanding external loads in the range of 400

pN[200]. This rapid thermal reversion of the push-pull azobenzene will then be delivered as a mechanical work. This switching can still take place when integrins have bound to the c(RGDfK) headgroup of the push-pull azobenzene. During one motion cycle, the azobenzene molecule changes its length from 9$\mathring{A}$ in the *trans* configuration to 5.5$\mathring{A}$ in the *cis*[140,141]. Therefore, this millisecond oscillation of the push-pull azobenzene is believed to be transferred to the c(RGDfK) ligand, which in turn exerts mechanical stimuli on the integrins in the cell membrane.

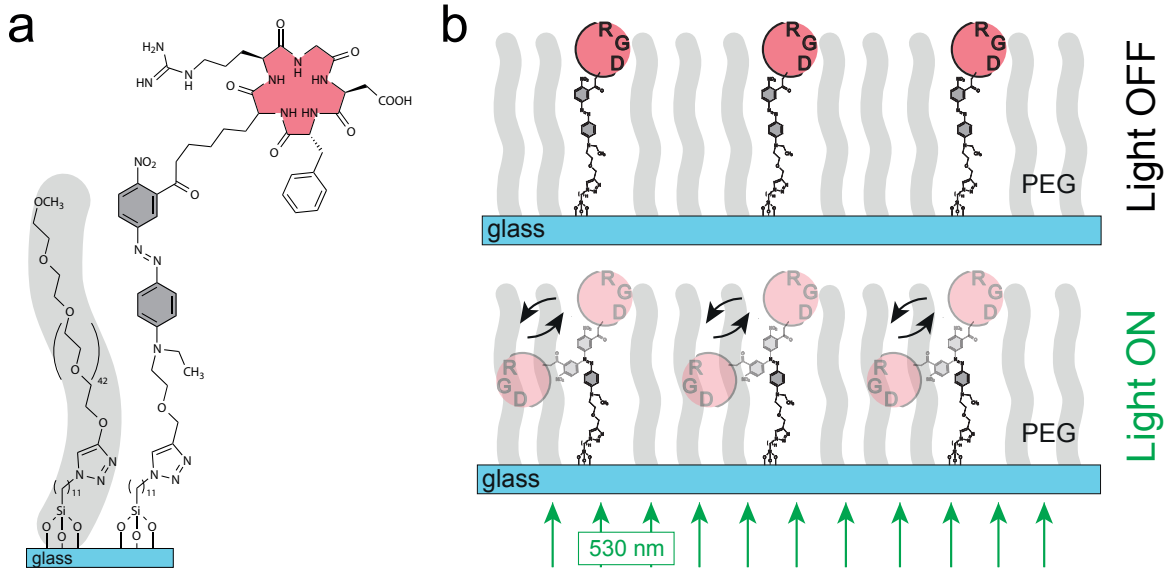

Figure 4.1: *Chemistry and working principle of the push-pull azobenzene. (a) shows the functionalization of a glass surface with PEG2000 and c(RGDfK) push-pull azobenzene. (b) Top: C(RGDfK)-coupled azobenzene monolayer. Bottom: Oscillation of the c(RGDfK)-azobenzene molecules during irradiation with 530 nm light*

To study the effect of such a light-induced ligand oscillation on cells, two complementary approaches were employed: Single-Cell Force Spectroscopy (SCFS) and gene expression experiments, both of which will be discussed in sections 4.3 and 4.4, respectively.

4.3 Single-Cell Force Spectroscopy (SCFS) on push-pull interfaces

Single-cell force spectroscopy enables an objective study of the reversibility of cell adhesion *in situ* on single-cell level using the same cell repeatedly on the same location of the sample[185]. Here, I measured cell detachment forces (F), last rupture strength

(F_s) and position (d) as well as the last tether length (w) in response to a cyclic switching of surface status, i.e. the light OFF/light ON course. Force distance curves were recorded after immobilizing a single cell on a tipless cantilever (inset in Fig. 4.2) in a setup similar to that described in section 3.3.1 in Chapter 3. Fig. 4.2 shows the detachment of an adhering cell from a c(RGDfK) push-pull azobenzene decorated surface in a force-distance curve for both when the surface is inactive (light switched OFF) (black curve) and when it is active (light switched ON) (green curve). The illumination of the substrate is done by an LED light mounted underneath the sample.

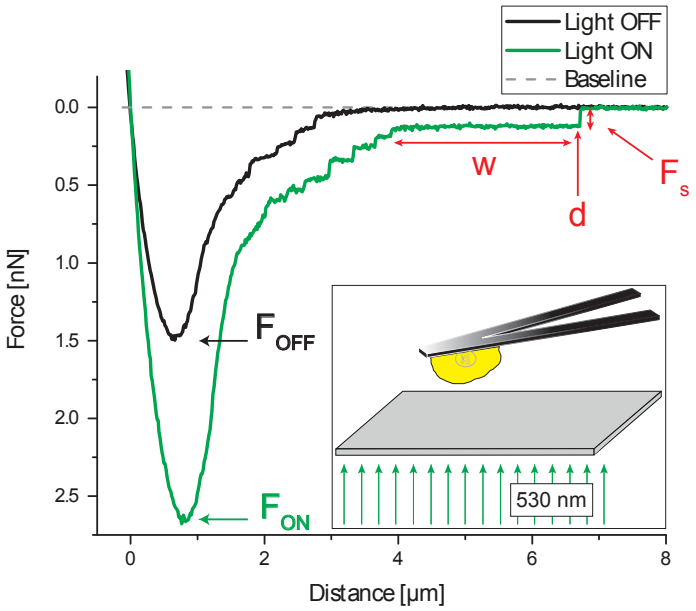

Figure 4.2: *SCFS experiment where a single cell is immobilized on a tipless cantilever and brought into contact with the substrate. Force-extension curves in the dark (black) and with 530 nm light (green) are shown. F_{OFF} and F_{ON} are the cell detachment forces when the light is switched off and on, respectively. F_s stands for the forces associated with the last rupture event, d is the detachment length in µm and w is the last tether length. Inset: A cell immobilized on a tipless cantilever and brought into contact with substrates.*

In order to examine the effect of ligand oscillation on cell adhesion and also to check the reversibility of this effect, several illumination cycles were performed *in situ* using a single cell (Fig. 4.3). Force-distance curves were initially recorded in the dark, i.e. with the c(RGDfK)-azobenzene in the *trans* state, before turning green light (530 nm) on. Subsequently, the surface molecules were oscillated by turning on the 530 nm light. Then, the light was switched off and the same cycle was repeated several times with cell-surface contact times of 1 and 3 s. A similar method was followed in a SCFS experiment with 5 s contact time. However, due to cell failure resulting from extended contact times and repeated loading of the cell, only a single switching cycle

was achieved (Fig. 4.3). As a first parameter, cell detachment forces were analyzed. Cell detachment force represents a critical value that is necessary to initiate cell release from the substrate. For both 1 and 3 s cell-surface contact time, there was a significant increase in detachment force when the light was switched on (Fig. 4.3). In detail, we determined an increase by 21.7 % ± 6.8 % for 1 s cell-surface contact time (6 cells, 2186 force curves) and by 26.4 % ± 11.5 % for 3 s cell-surface contact time (5 cells, 951 force curves). Only one SCFS experiment with 5 s contact time has been performed, thus the detachment force results will only be shown qualitatively in Fig. 4.3 and will not be taken into consideration for further detailed calculations. A continuous irradiation with light while recording force-distance curves might lead to a temperature increase inside the sample chamber. However, previous work had shown theoretically as well as experimentally that a temperature increase causes a drop in binding strength as discussed in detail in Appendix D.3[201]. The increase in cell detachment force that was observe on the c(RGDfK) push-pull azobenzene surfaces is believed to be resulting from the mechanical oscillation transmitted from the azobenzene molecules to the integrins in the cell membrane.

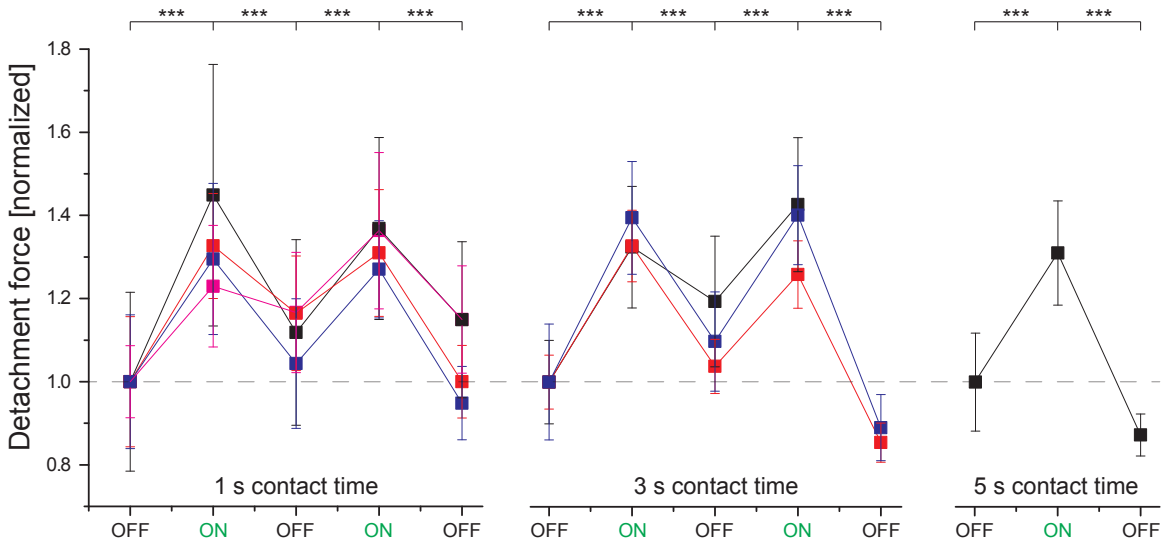

Figure 4.3: *The normalized values for cell detachment force in several subsequent irradiation cycles for 1, 3 and 5 s contact times. Each curve represents the results of a different experiment with a different cell. Cell detachment force increases considerably when the azobenzene molecules are illuminated and can oscillate. Due to cell failure, some cell were not able to complete the multiple switching cycle, as shown by the black curve in the 3 s contact time and also the 5 s contact time. Error bars indicate normalized standard deviations.*

A very important parameter in SCFS experiments is the force associated with the last single rupture, as it should mainly give results about the adhesion of tiny adhesion

sites or even single molecules with the surface. In these experiments, the force associated with the last rupture and the position of the last rupture event show a noticeable shift towards stronger values during irradiation (Fig. 4.4). The maxima of the last rupture force distributions for 1 and 3 s adhesion times are shifted by approximately 6 and 8 pN, respectively and the maxima shift of the detachment length distributions are approximately 0.8 and 0.9 μm, respectively. Those shifts are significant at a level of $p < 0.001$ (Students t-test) for both cell-surface contact times (number of force curves for 1 s contact time: 1318 (light OFF) and 868 (light ON); 3 s contact time experiments: 559 (light OFF) and 392 (light ON)).

Hence, a clear increase in relative frequency at higher rupture forces in response to light illumination is evident. A significant increase due to light illumination has also been observed for the length of the last tether w, which gives information about the lifetime of bonds under constant force load (more information can be found in section 1.5.2). The increase of single rupture force, detachment length and tether length observed in these experiments is believed to be due to a mechanical stimulation of integrin binding that is attributed to the oscillation of the push-pull azobenzene.

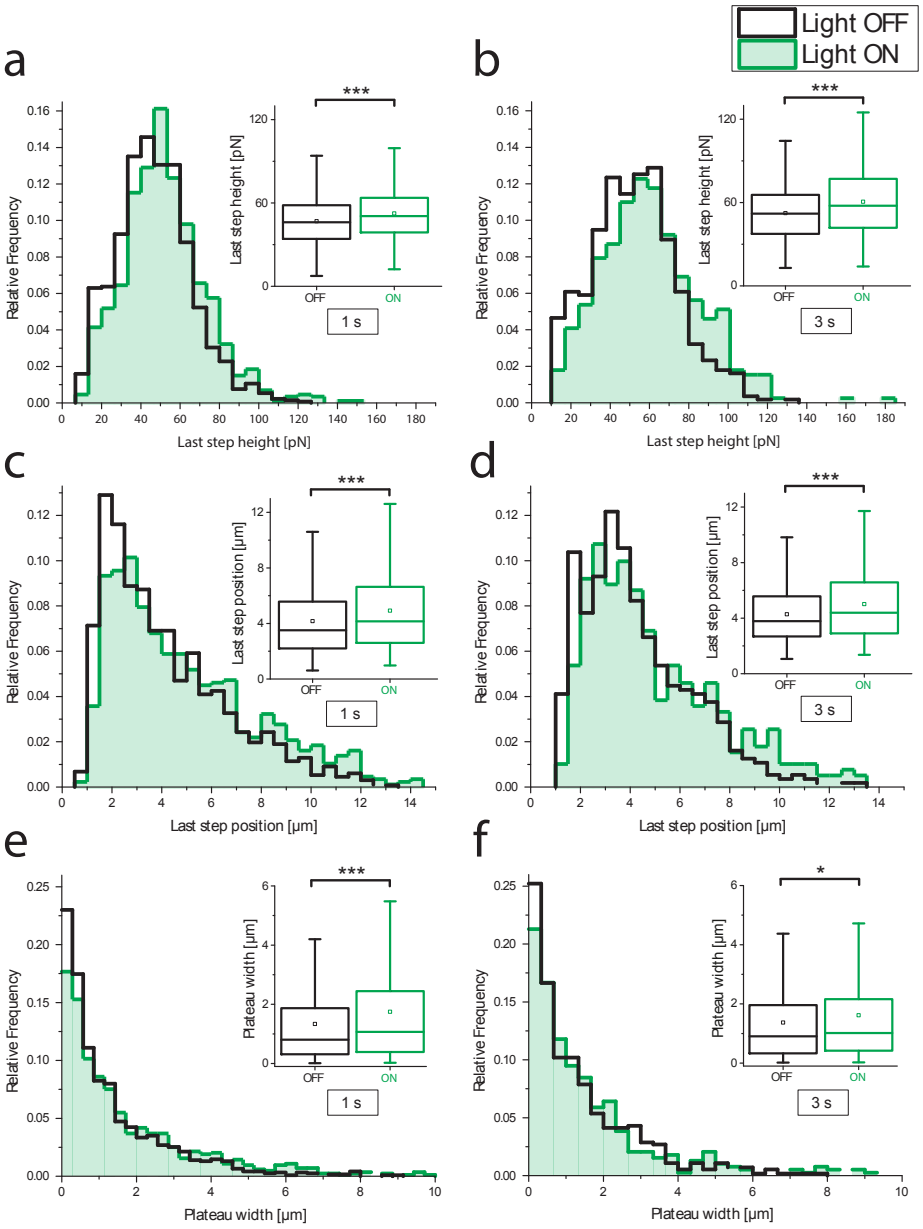

Figure 4.4: *Relative frequencies of the last rupture's force F_s and position d as well as the plateau width w, all of which extracted from force-distance curves of the SCFS experiments. The results of F_s, d and w are shown for both 1 s contact time in a, c and e, respectively, and 3 s contact time in b, d, and f, respectively. The results show a noticeable shift towards higher values as a response to the oscillation of the push-pull azobenzene. These shifts are confirmed by the t test (one-tail independent sample t test that is discussed in detail in Appendix A.1), which shows a significant difference at the 0.001 level (except for the plateau width in the 3 s contact time experiment, which only showed a significance at 0.1 level), which are displayed in the insets in each figure. Number of analyzed rupture events: 1318 (OFF) and 868 (ON) for 1 s, 559 (OFF) and 392 (ON) for 3 s.*

Moreover, in order to measure the work needed to achieve a complete detachment of the cell from the substrate, the detachment energy was measured for 1, 3 and 5 s cell-substrate contact time experiments. Fig. 4.5 shows that the energy needed to detach the cell from the substrate is larger when the azobenzene is in an oscillating state, i.e. during light exposure. This behavior can be seen in 1, 3 and 5 s contact time SCFS experiments. Fig. 4.5 also demonstrates that the energy needed to detach the cell from the substrate is larger for 3 s adhesion experiments compared with 1 s experiments.

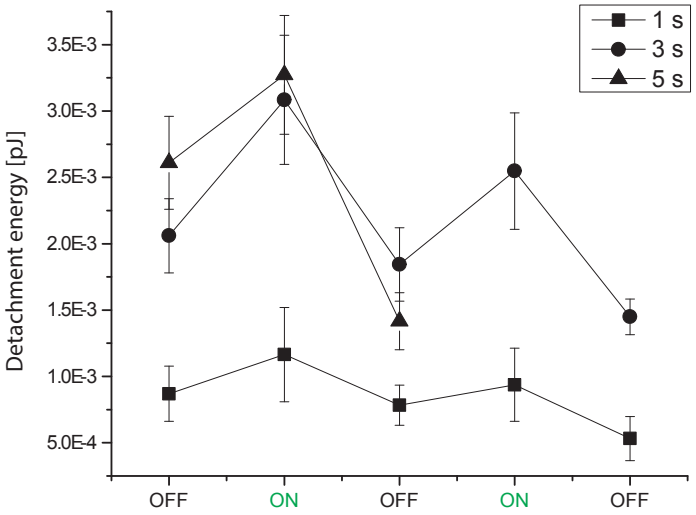

Figure 4.5: *Representative examples of cell detachment energies for 1, 3 and 5 s cell-substrate contact time SCFS experiments on c(RGDfK) functionalized push-pull azobenzene. An increase in detachment energy is observed in response to the oscillation of the c(RGDfK) ligand in the push-pull azobenzene, which is triggered during light exposure. In the 5 s experiment, on force curves were recorded after the first switching cycle due cell failure.*

In order to test the influence of c(RGDfK) oscillation on rupture formation, we calculated the number of ruptures associated with each force-distance curve taken. The results show no noticeable difference in the number of ruptures between oscillating and static conditions (Fig. 4.6).

The cell detachment force, the detachment energy and the last rupture analysis provide a plethora of information about cellular interaction with the environment. However, these parameters fail to provide information regarding the type of interaction the cell develops with the substrate, i.e. they fall short of describing the anchorage of integrins to the microenvironment[202]. A good description of this interaction can be obtained by evaluating the slope before a rupture event, which is demonstrated in Fig. 4.7 a, with the distance from the surface at which the rupture takes place. This

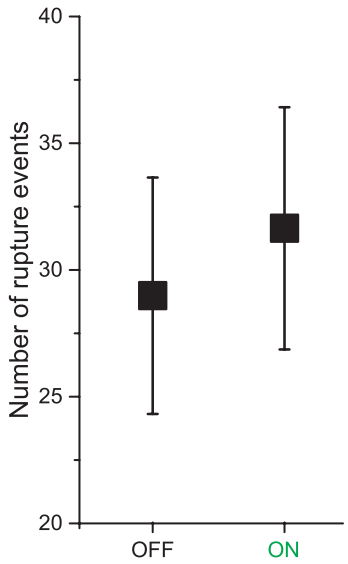

Figure 4.6: *The number of rupture events calculated for a representative example (i.e. one cell) of a SCFS experiment with 1 s contact time. The results show no noticeable difference in the number of events occurring when the light is switched on or off, i.e. with or without ligand oscillation.*

offers a two-dimensional density plot that enables a simple method to visualize the results. It also enables an easy way to distinguish long membrane tethers from shorter jump-like ruptures that are usually obtained from cytoskeletal-anchorage bindings[202]. Therefore, in order to acquire a better understanding of the integrin-c(RGDfK) ligand interaction in the system presented in this chapter, the two-dimensional probability density was plotted and illustrated in Fig. 4.7 (heat maps). The results show that there is no noticeable difference in the slope prior to the last rupture event between the active (light on) and the inactive (light off) states for both 1 and 3 s contact time experiments (Fig. 4.7 b and c, respectively). The results also show that the slope values in both the active and the inactive are mostly zero, indicating that the last rupture is dominantly a membrane tether. This also implied that the ligand oscillation does not change the cytoskeletal coupling.

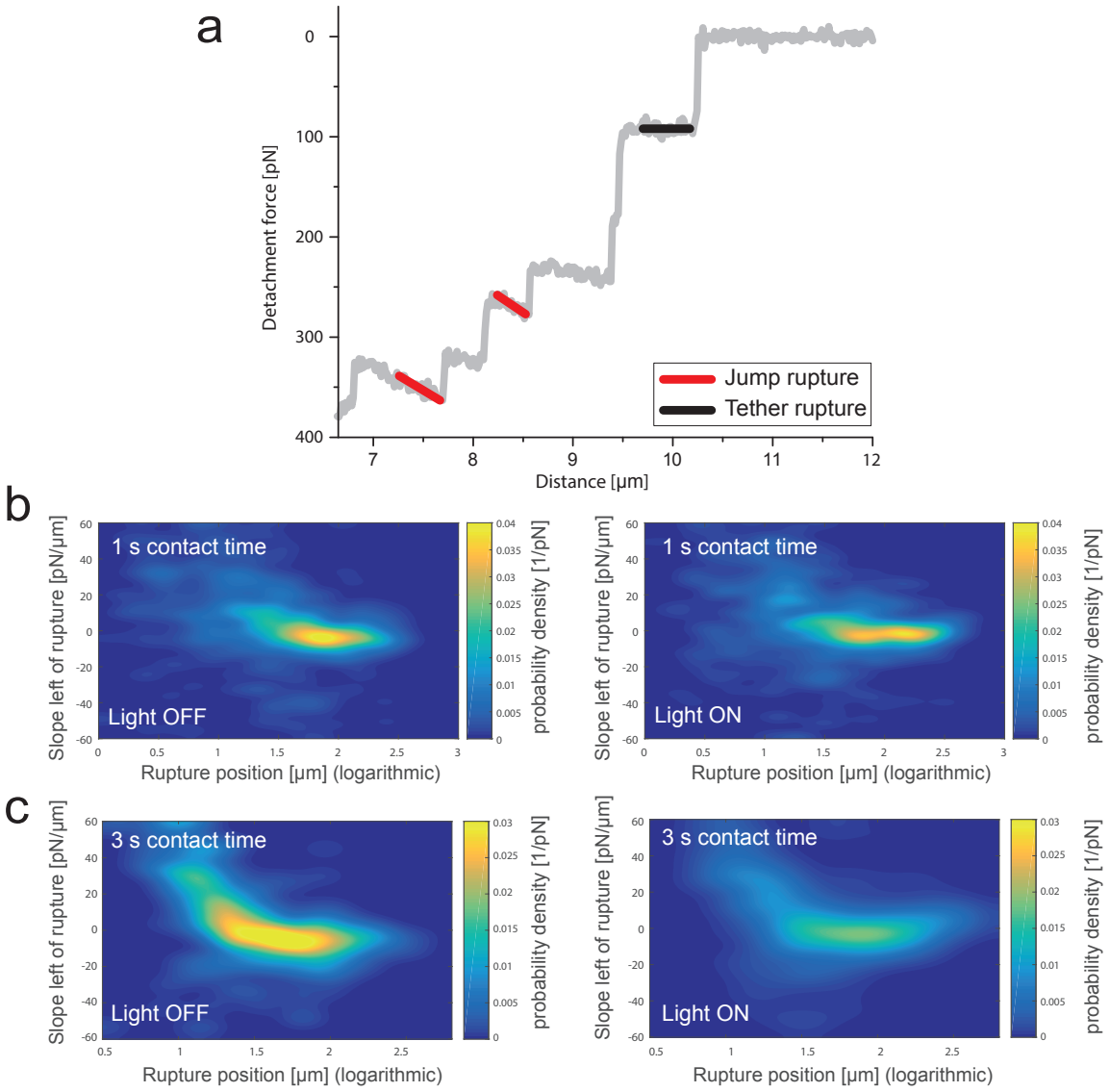

Figure 4.7: *(a) A representative force-distance curve demonstrating both jump and tether ruptures, which can be distinguished by the slope prior (left) to the rupture. (b) and (c) The two-dimensional probability densities for both 1 and 3 s contact time experiments, respectively. The slope prior to the last rupture in both experiments does not seem to change in response to ligand oscillation, which takes place when the light is switched on. Number of analyzed rupture events: 1318 (OFF) and 868 (ON) for 1 s, 559 (OFF) and 392 (ON) for 3 s.*

4.4 Gene expression experiments on push-pull interfaces

Mechanical forces are transmitted from the extracellular matrix to the cell's cytoskeleton through integrins, which in turn are connected to the actin filaments through a number of linker proteins such as vinculin, paxillin, zyxin and talin. In addition to providing means to transfer signals to the cytosol, these proteins also help stabilizing adhesion clusters by regulating gene expression through a feedback system. The change in adhesion behavior due to ligand oscillation, as presented in the previous section, implies a change in cell function, which is governed by proteins encoded by genes[203]. One of the most reported cellular response to mechanical signals is through a regulation of gene expression, i.e. an increase or decrease in generating gene products such as proteins[204–206]. Therefore, the gene expression of these linker proteins at the mRNA level has been studied in response to a mechanical stimulation delivered through the oscillation of c(RGDfK)-functionalized push-pull azobenzene. This study has been kindly conducted by Dr. Wei Wang.

The gene expression experiment was conducted as illustrated in Fig. 4.8. Fibroblast cells were seeded on push-pull azobenzene-coated substrates and left to incubate for 30 min. The samples then underwent consecutive series of light exposure and incubation cycles, each with defined time and number of repetitions (Fig. 4.8 A). The results show a clear upregulation of the gene expression for vinculin, paxillin, zyxin and talin with a clear fold change in expression level (Fig. 4.8 B) in response to irradiation of cells on a c(RGDfK)-push-pull azobenzene in comparison to cells on uncoated glass surfaces. Fold change is a common measure of gene expression that signifies the change from the initial to the final value, e.g. a fold change of one corresponds to a doubling of the counts obtained. All these proteins are essential proteins in a focal adhesion cluster, which has previously been reported to have mechanosensory properties[207]. Hence, this upregulation of proteins is believed to be triggered by the molecular mechanical stimulation, like a "tickling" of the cell, prompted through oscillations of the c(RGDfK) push-pull azobenzenes that is encountered by integrins during light exposure.

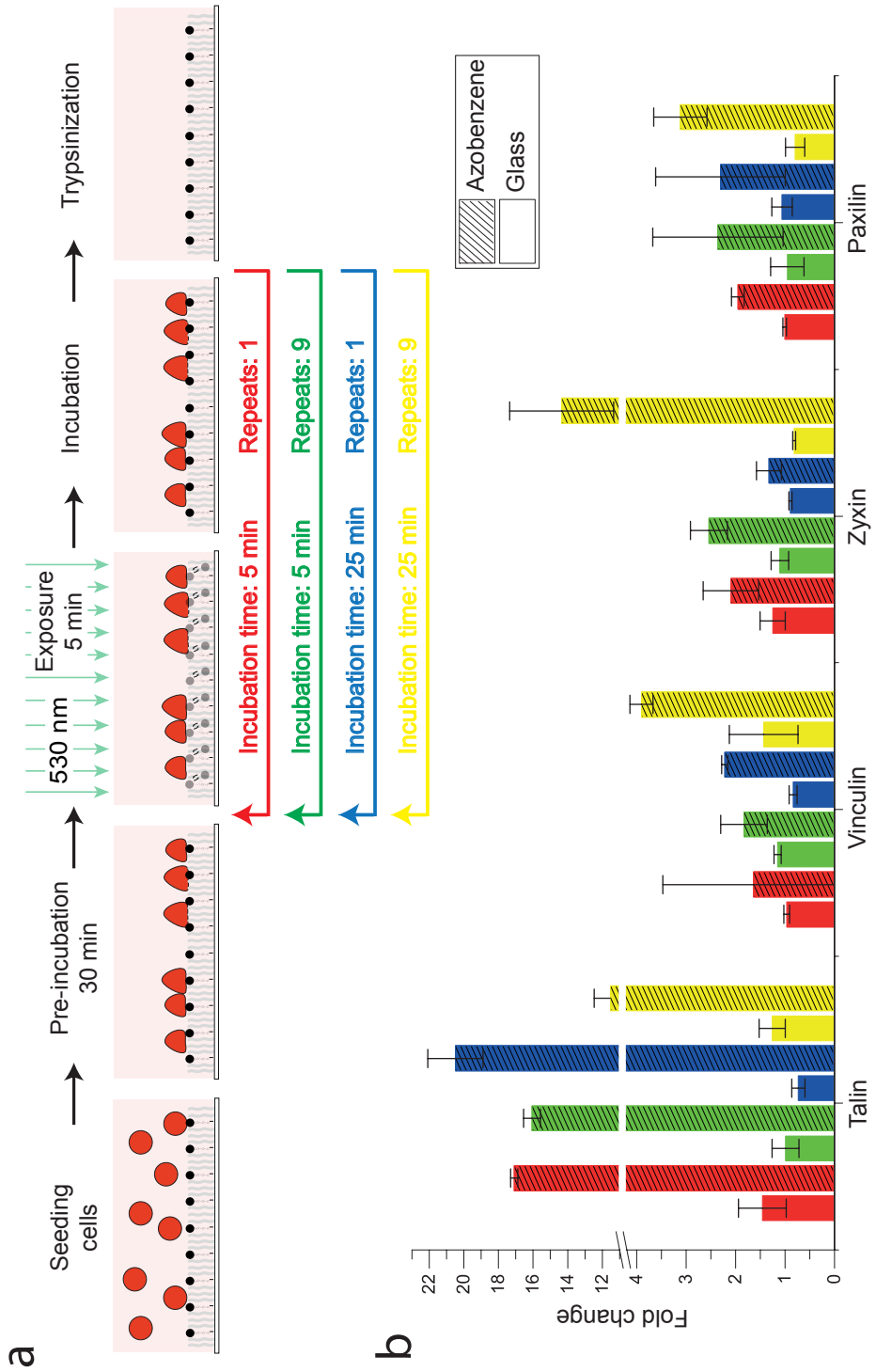

Figure 4.8: *Gene expression experiment. (a) Experimental steps showing four different types of experiments with different light stimulation protocols (different incubation times and repetitions). (b) Average fold changes in gene expression in response to different light stimulation protocols on c(RGDfK) push-pull azobenzene surfaces. Three samples were analyzed for each data point and error bars denote standard deviation.*

4.5 Conclusion

The SCFS results show a significant increase in cell detachment force as a result of the mechanical oscillation of the c(RGDfK) ligands coupled to the push-pull azobenzene molecules. Likewise, the results from the gene expression experiments also show a significant upregulation in the expression of several proteins that have been reported to be involved in mechanosensing. As the light-induced heating of push-pull azobenzenes is negligible, the observed reinforcement in cell adhesion, at both cell and single-rupture levels, as well as the upregulation in gene expression are attributed to the activation of mechanosensory mechanisms. The increase in detachment force is believed to be attributed to the activation of a catch bond mechanism in the binding of integrins, which becomes stronger in response to an applied force. Bond strengthening could also be due to a mechanical stimulation of other components of the focal adhesion clusters, which have been proposed to act as mechanosensors, such as talin and vinculin. The experimental outcome of this work shows that cell adhesion is not only influenced by large scale forces transmitted through the cytoskeleton, as reported previously, but also by the oscillations of integrin ligands. The ability to exert oscillatory "tickling" forces to single adhesion proteins provides both an intriguing method to investigate cellular reaction to molecularly-defined forces as well as a novel approach to induce mechanotransduction. As cellular mechanosensing is an important mechanism in stem cell differentiation, the ability to trigger molecular interactions through mechanosensing will offer a great potential to provide pioneering strategies for prompting cell functions. This work represents a starting point for exciting possibilities to control cellular behavior at the molecular level with light.

Conclusion

In my thesis, biological interfaces that enable a comprehensive study of the impact of ligand density, structure and oscillation on cellular interactions with the environment, have been developed. These biofunctional interfaces offer intriguing methods to control cell adhesion on a wide scale, starting from cellular to single-cell and down to the molecular level. Controlling cell adhesion in this work was conducted in both static and dynamic fashions. The static approach for controlling cell adhesion using novel micronanostructured interfaces is presented in the first part of my thesis. On the other hand, the approach for a dynamic control of cell adhesion is carried out using light-responsive interfaces, as discussed in the second part of this work. The static control of cell adhesion was performed using novel micronanostrucutures that have been prepared using Block-Copolymer Micelle Nanolithography (BCML) in combination with photolithography. The combination of the two techniques enabled the development of a unique method for fabricating microstructured substrates decorated with gold nanoparticles having well-defined interparticle spacings.

In this method, nanotopographic substrates with checkerboard-like patterns consisting of segments of varying heights have been generated using conventional photolithography. Using these substrates as platforms for subsequent patterning by BCML resulted in micronanostructures with a controlled arrangement of quasi-hexagonally ordered gold nanoparticles via pure self-assembly. The interparticle spacing is dictated by the height of the topographical segment and different interparticle spacings between adjacent segments have been achieved. Thus, this strategy provides a high-throughput method for controlling the density and spacing of the nanoparticles on micrometer-sized segments. Fluorescence microscopy showed that the nanotopographic pattern does not hinder cells from adhering to the substrate. Hence, these micronanostrucutures have a great potential to control specific cellular functions through a local microstructuring of the density of proteins that mediate cell adhesion. As BCML is applicable to various types of substrates and the etching of regular nanotopogra-

phies has become a routine process, a straightforward transfer of this surface-coating strategy to numerous kinds of samples is now feasible.

In the second half of my thesis, a dynamic control of cell adhesion was addressed with two strategies that allowed a rapid and reversible switching of cell adhesion. Both strategies are based on using light-responsive azobenzenes that have been biofunctionalized with RGD peptides. These two studies provide a demonstration of the photoswitching mechanism at both cellular and molecular scales and allow an unprecedented dynamic control of cell adhesion. In the first strategy, the dynamic control of cell adhesion was realized using Single-Cell Force Spectroscopy (SCFS) measurements, which showed that cell adhesion was reversibly switched. This was proven by measuring the reversible change in the detachment force, with a variation of approximately 20 %, in several consecutive *trans*/*cis* switching cycles. The SCFS results also showed a drop in the number of individual single rupture events between the cell and the surface when the azobenzene was switched to the *cis* configuration, hence proving the change in bound molecules due to switching. The surface coating strategy presented here can be easily applied to many different metallic materials that contain a silanizable oxide layer, including biomedically relevant implant materials such as Ti and NiTi.

In another attempt to achieve a dynamic control of cell adhesion, push-pull azobenzenes have been used for the preparation of biofunctional interfaces. If the RGD-coupled push-pull azobenzenes were forced to oscillate through visible light illumination, an average increase in cell detachment force of about 21 −27 % has been demonstrated by the SCFS experiments. This result is supported by gene expression studies at the mRNA level. The observed reinforcement in cell adhesion as well as the upregulation in gene expression are both attributed to the activation of mechanosensory mechanisms. The experimental outcome demonstrates that cell adhesion is not only influenced by large scale forces transmitted through the cytoskeleton, as reported previously, but also by the oscillations of integrin ligands. The ability to exert oscillatory "tickling" forces to single adhesion proteins provides both an intriguing method to investigate cellular reaction to molecularly-defined forces as well as a novel approach to induce mechanotransduction. As cellular mechanosensing is an important mechanism in stem cell differentiation, the ability to trigger molecular interactions through mechanosensing will offer a great potential to provide pioneering strategies for prompting cell functions. The dynamic control of cell adhesion proposed in this study presents a great stepping stone towards exciting possibilities for controlling cellular behavior at the molecular level with light.

Bibliography

[1] Marco Arnold. Molecularly Defined Nanostructured Interfaces as Tools for the Regulation and the Measurement of Functional Length Scales in Cell Adhesion Mediating Protein Clusters. *PhD Thesis*, page 162, 2005.

[2] Alberts et al. *Molecular Biology of the Cell*. New York: Garland Science, 2002.

[3] Martin Benoit and Christine Selhuber-unkel. Atomic Force Microscopy in Biomedical Research. 736, 2011.

[4] R Brackenbury. Cell adhesion molecules. *annual reports in medicinal chemistry*, 1989.

[5] Peter Hinterdorfer and Yves F Dufrêne. Detection and localization of single molecular recognition events using atomic force microscopy. *Nature methods*, 3(5):347–355, 2006.

[6] James Faull, Mark Howard, R J Faull, and Renal Unit. Signaling Through. *Journal of the American Society of Nephrology*, pages 1091–1097.

[7] Christine Selhuber-Unkel. *Biological Adhesion on Nanopatterned Substrates Studied with Force Spectroscopy and Microinterferometry*. PhD thesis, 2006.

[8] Richard O. Hynes. Integrins: Bidirectional, allosteric signaling machines. *Cell*, 110(6):673–687, 2002.

[9] Renhao Li, Neal Mitra, Holly Gratkowski, Gaston Vilaire, Rustem Litvinov, Chandrasekaran Nagasami, John W Weisel, James D Lear, William F Degrado, and Joel S Bennett. Activation of integrin alphaIIbbeta3 by modulation of

transmembrane helix associations. *Science (New York, NY)*, 300(5620):795–798, 2003.

[10] Ulrich Schwarz. Forces and elasticity in cell adhesion. *Habilitation*, pages 1–133, 2004.

[11] Evan Evans. Probing the relation between force lifetime and chemistry. 2001.

[12] H.A. Kramers. Brownian motion in a field of force and the diffusion model of chemical reactions. *Physica*, 7(4):284–304, 1940.

[13] Wendy E Thomas, Viola Vogel, and Evgeni Sokurenko. Biophysics of catch bonds. *Annu. Rev. Biophys.*, 37:399–416, 2008.

[14] E Evans and K Ritchie. Dynamic strength of molecular adhesion bonds. *Biophysical journal*, 72(4):1541–1555, 1997.

[15] Julian Shillcock and Udo Seifert. Escape from a metastable well under a time-ramped force. pages 1–9, 1998.

[16] Ernst-ludwig Florin, Vincent T Moy, and Hermann E Gaub. Adhesion Forces Between Individual Ligand-Receptor Pairs. *Science*, 264(April):415–417, 1994.

[17] Irina Schumakovitch, Wilfried Grange, Torsten Strunz, Patricia Bertoncini, Hans-Joachim Güntherodt, and Martin Hegner. Temperature dependence of unbinding forces between complementary DNA strands. *Biophysical journal*, 82(1 Pt 1):517–521, 2002.

[18] George I Bell and George I Bell. Models for the Specific Adhesion of Cells to Cells. 200(4342):618–627, 1978.

[19] H Qian and B E Shapiro. Graphical method for force analysis: macromolecular mechanics with atomic force microscopy. *Proteins*, 37(4):576–581, 1999.

[20] E. Evans. Energy landscapes of biomolecular adhesion and receptor anchoring at interfaces explored with dynamic force spectroscopy. *Faraday Discussions*, 1998.

[21] R Merkel, P Nassoy, a Leung, K Ritchie, and E Evans. Energy landscapes of receptor-ligand bonds explored with dynamic force spectroscopy. *Nature*, 397(January):50–53, 1999.

[22] M. Dembo, D. C. Torney, K. Saxman, and D. Hammer. The reaction-limited kinetics of membrane-to-surface adhesion and detachment. *Proceedings of the Royal Society of London B: Biological Sciences*, 234(1274):55–83, 1988.

[23] Yuriy V. Pereverzev, Oleg V. Prezhdo, Manu Forero, Evgeni V. Sokurenko, and Wendy E. Thomas. The Two-Pathway Model for the Catch-Slip Transition in Biological Adhesion. *Biophysical Journal*, 89(3):1446–1454, 2005.

[24] Denis Bartolo, Imre Derényi, and Armand Ajdari. Dynamic response of adhesion complexes: Beyond the single-path picture. *Physical Review E - Statistical, Nonlinear, and Soft Matter Physics*, 65(5):051910, 2002.

[25] Wendy Thomas, Manu Forero, Olga Yakovenko, Lina Nilsson, Paolo Vicini, Evgeni Sokurenko, and Viola Vogel. Catch-bond model derived from allostery explains force-activated bacterial adhesion. *Biophysical journal*, 90(3):753–764, 2006.

[26] *Mechanobiology of Cell-Cell and Cell-Matrix Interactions*. Springer US, 2011.

[27] Ning Wang, Jessica D Tytell, and Donald E Ingber. Mechanotransduction at a distance: mechanically coupling the extracellular matrix with the nucleus. *Nature reviews. Molecular cell biology*, 10(1):75–82, 2009.

[28] Ronald H. Schwartz. Adhesion-dependent cell mechanosensitivity. *Annual Review of Immunology*, 21(1):305–334, 2003.

[29] J. H C Wang and B. P. Thampatty. An introductory review of cell mechanobiology. *Biomechanics and Modeling in Mechanobiology*, 5(1):1–16, 2006.

[30] Akiko Mammoto, Kip M Connor, Tadanori Mammoto, Chong Wing Yung, Dongeun Huh, Christopher M Aderman, Gustavo Mostoslavsky, Lois E H Smith, and Donald E Ingber. A mechanosensitive transcriptional mechanism that controls angiogenesis. *Nature*, 457(7233):1103–1108, 2009.

[31] Dennis E Discher, Paul Janmey, and Yu-Li Wang. Tissue cells feel and respond to the stiffness of their substrate. *Science (New York, N.Y.)*, 310(5751):1139–43, 2005.

[32] Carson H Thomas, Joel H Collier, Charles S Sfeir, and Kevin E Healy. Engineering gene expression and protein synthesis by modulation of nuclear shape. *Proceedings of the National Academy of Sciences of the United States of America*, 99(4):1972–7, 2002.

[33] C S Chen, M Mrksich, S Huang, G M Whitesides, and D E Ingber. Geometric control of cell life and death. *Science (New York, N.Y.)*, 276(5317):1425–1428, 1997.

[34] Adam Curtis and Chris Wilkinson. Topographical control of cells. *Biomaterials*, 18(24):1573–1583, 1997.

[35] Hong-bei B Wang, Micah Dembo, Yu-li L Wang, Saba Ghassemi, Giovanni Meacci, Shuaimin Liu, Alexander a Gondarenko, Anurag Mathur, Pere Roca-cusachs, Michael P Sheetz, James Hone, Jennifer L Leight, Michele a Wozniak, Sophia Chen, Michelle L Lynch, and S Christopher. Substrate flexibility regulates growth and apoptosis of normal but not transformed cells. *American journal of physiology. Cell physiology*, 279(5):C1345—-50, 2013.

[36] Adam J. Engler, Shamik Sen, H. Lee Sweeney, and Dennis E. Discher. Matrix Elasticity Directs Stem Cell Lineage Specification. *Cell*, 126(4):677–689, 2006.

[37] W Sigurdson, a Ruknudin, and F Sachs. Calcium imaging of mechanically induced fluxes in tissue-cultured chick heart: role of stretch-activated ion channels. *The American journal of physiology*, 262(4 Pt 2):H1110–5, 1992.

[38] Steven Munevar, Yu-Li Wang, and Micah Dembo. Regulation of mechanical interactions between fibroblasts and the substratum by stretch-activated Ca2+ entry. *Journal of cell science*, 117(Pt 1):85–92, 2004.

[39] J Lee, a Ishihara, G Oxford, B Johnson, and K Jacobson. Regulation of cell movement is mediated by stretch-activated calcium channels. *Nature*, 400(6742):382–386, 1999.

[40] Marcus Schewe, Ehsan Nematian-Ardestani, Han Sun, Marianne Musinszki, Sönke Cordeiro, Giovanna Bucci, BertL. deGroot, StephenJ. Tucker, Markus Rapedius, and Thomas Baukrowitz. A Non-canonical Voltage-Sensing Mechanism Controls Gating in K2P K+ Channels. *Cell*, 164(5):937–949, 2016.

[41] Benjamin Geiger, Joachim P Spatz, and Alexander D Bershadsky. Environmental sensing through focal adhesions. *Nature reviews. Molecular cell biology*, 10(1):21–33, 2009.

[42] Sarah J Parsons and J Thomas Parsons. Src family kinases, key regulators of signal transduction. *Oncogene*, 23(48):7906–9, 2004.

[43] Neil O. Carragher and Margaret C. Frame. Focal adhesion and actin dynamics: A place where kinases and proteases meet to promote invasion. *Trends in Cell Biology*, 14(5):241–249, 2004.

[44] Satyajit K Mitra, Daniel A Hanson, and David D Schlaepfer. Focal adhesion kinase: in command and control of cell motility. *Nat Rev Mol Cell Biol*, 6(1):56–68, jan 2005.

[45] D Riveline, E Zamir, N Q Balaban, U S Schwarz, T Ishizaki, S Narumiya, Z Kam, B Geiger, and a D Bershadsky. Focal contacts as mechanosensors: externally applied local mechanical force induces growth of focal contacts by an mDia1-dependent and ROCK-independent mechanism. *The Journal of cell biology*, 153(6):1175–86, jun 2001.

[46] Christopher S. Chen, John Tan, and Joe Tien. Mechanotransduction at Cell-Matrix and Cell-Cell Contacts. *Annual Review of Biomedical Engineering*, 6(1):275–302, 2004.

[47] M J Davis, X Wu, T R Nurkiewicz, J Kawasaki, G E Davis, M a Hill, and G a Meininger. Integrins in Mechanotransduction. *American journal of physiology. Heart and circulatory physiology*, 280:H1427–H1433, 2001.

[48] D Choquet, D P Felsenfeld, and M P Sheetz. Extracellular matrix rigidity causes strengthening of integrin-cytoskeleton linkages. *Cell*, 88(1):39–48, 1997.

[49] N. Wang, J.P. P Butler, and D.E. E Ingber. Mechanotransduction across the cell surface and through the cytoskeleton. *Science (New York, N.Y.)*, 260(5111):1124–1127, 1993.

[50] Matthew J. Paszek, David Boettiger, Valerie M. Weaver, and Daniel A. Hammer. Integrin clustering is driven by mechanical resistance from the glycocalyx and the substrate. *PLoS Computational Biology*, 5(12), 2009.

[51] a. J. Garcia, F. Huber, and D. Boettiger. Force Required to Break 51Integrin-Fibronectin Bonds in Intact Adherent Cells Is Sensitive to Integrin Activation State. *Journal of Biological Chemistry*, 273(18):10988–10993, 1998.

[52] Kenya Honda, Hideyuki Yanai, Hideo Negishi, Masataka Asagiri, Mitsuharu Sato, Tatsuaki Mizutani, Naoya Shimada, Yusuke Ohba, Akinori Takaoka, Nobuaki Yoshida, and Tadatsugu Taniguchi. IRF-7 is the master regulator

of type-I interferon-dependent immune responses. *Nature*, 434(7034):772–777, 2005.

[53] H B Wang, M Dembo, S K Hanks, and Y Wang. Focal adhesion kinase is involved in mechanosensing during fibroblast migration. *Proceedings of the National Academy of Sciences of the United States of America*, 98(20):11295–300, 2001.

[54] R P Johnson and S W Craig. F-actin binding site masked by the intramolecular association of vinculin head and tail domains., 1995.

[55] Dongrong Chen, Caroline R M Wilkinson, Stephen Watt, Christopher J Penkett, W Mark Toone, Nic Jones, and Jürg Bähler. Multiple pathways differentially regulate global oxidative stress responses in fission yeast. *Molecular biology of the cell*, 19(1):308–317, 2008.

[56] N Q Balaban, U S Schwarz, D Riveline, P Goichberg, G Tzur, I Sabanay, D Mahalu, S Safran, a Bershadsky, L Addadi, and B Geiger. Force and focal adhesion assembly: a close relationship studied using elastic micropatterned substrates. *Nature cell biology*, 3(5):466–472, 2001.

[57] Viola Vogel and Michael Sheetz. Local force and geometry sensing regulate cell functions. *Nature Reviews Molecular Cell Biology*, 7(4):265–275, 2006.

[58] M. A. Schwartz. Integrins, oncogenes, and anchorage independence. *Journal of Cell Biology*, 139(3):575–578, 1997.

[59] Erik H J Danen and Kenneth M. Yamada. Fibronectin, integrins, and growth control. *Journal of Cellular Physiology*, 189(1):1–13, 2001.

[60] Victoria H. Freedman and Seung il Shin. Cellular tumorigenicity in nude mice: Correlation with cell growth in semi-solid medium. *Cell*, 3(4):355–359, 1974.

[61] Sui Huang and Donald E. Ingber. Cell tension, matrix mechanics, and cancer development. *Cancer Cell*, 8(3):175–176, 2005.

[62] Ilya Levental, Penelope C. Georges, and Paul A Janmey. Soft biological materials and their impact on cell function. 3(3):299, 2007.

[63] Kandice R. Levental, Hongmei Yu, Laura Kass, Johnathon N. Lakins, Mikala Egeblad, Janine T. Erler, Sheri F T Fong, Katalin Csiszar, Amato Giaccia, Wolfgang Weninger, Mitsuo Yamauchi, David L. Gasser, and Valerie M. Weaver.

Matrix Crosslinking Forces Tumor Progression by Enhancing Integrin Signaling. *Cell*, 139(5):891–906, 2009.

[64] Matthew J. Paszek, Nastaran Zahir, Kandice R. Johnson, Johnathon N. Lakins, Gabriela I. Rozenberg, Amit Gefen, Cynthia A. Reinhart-King, Susan S. Margulies, Micah Dembo, David Boettiger, Daniel A. Hammer, and Valerie M. Weaver. Tensional homeostasis and the malignant phenotype. *Cancer Cell*, 8(3):241–254, 2005.

[65] Sergey V. Plotnikov, Ana M. Pasapera, Benedikt Sabass, and Clare M. Waterman. Force fluctuations within focal adhesions mediate ECM-rigidity sensing to guide directed cell migration. *Cell*, 151(7):1513–1527, 2012.

[66] By Geoffrey A Ozin. Nanochemistry: synthesis in diminishing dimensions. *Precision Engineering*, 15:206, 1993.

[67] Markus Antonietti and C Göltner. Superstructures of functional colloids: chemistry on the nanometer scale. *Angew. Chem.*, 36:910–928, 1997.

[68] Paul Alivisatos, Paul F Barbara, a Welford Castleman, Jack Chang, David a Dixon, Michael L Klein, George L McLendon, Joel S Miller, Mark a Ratner, Peter J Rossky, Samuel I Stupp, and Mark E Thompson. From Molecules to Materials: Current Trends and Future Directions. *Advanced Materials*, 10(16):1297–1336, 1998.

[69] Joachim P. Spatz. Nano- and Micropatterning by Organic Inorganic Templating of Hierarchical. *Angewandte Chemie (International ed. in English)*, (18):3359–3362, 2002.

[70] Roman Johann Peter Glass. *Micellar Nano- and Electron Beam Lithography and its applications*. PhD thesis, Naturwissenschaftlich-Mathematischen Gesamtfakultt der Ruprecht-Karls-Universitt Heidelberg, 2005.

[71] Marco Arnold, Elisabetta Ada Cavalcanti-Adam, Roman Glass, Jacques Bluemmel, Wolfgang Eck, Martin Kantlehner, Horst Kessler, and Joachim P Spatz. Activation of integrin function by nanopatterned adhesive interfaces. *Chemphyschem : a European journal of chemical physics and physical chemistry*, 5(3):383–8, mar 2004.

[72] Roman Glass, Marco Arnold, Elisabetta Ada Cavalcanti-Adam, Jacques Blümmel, Christian Haferkemper, Charlotte Dodd, and Joachim P. Spatz. Block

copolymer micelle nanolithography on non-conductive substrates. *New Journal of Physics*, 6:1–17, 2004.

[73] W. R. Schowalter W. B. Russel, D. A. Saville. *Colloidal Dispersions*. Cambridge University Press, Cambridge, 1989.

[74] H Weller. Quantized Semiconductor Particles - a Novel State of Matter for Materials Science. *Advanced Materials*, 5(2):88–95, 1993.

[75] Richard Nötzel and Dr. Toshiaki Tamamura. Full paper. (2):2–6, 1995.

[76] D F Zaretsky. Giant dipole resonance in small metal clusters. 77:379–383, 1993.

[77] Kathy Selby, Vitaly Kresin, Jun Masui, Michael Vollmer, Walt A. De Heer, Adi Scheidemann, and W. D. Knight. Photoabsorption spectra of sodium clusters. *Physical Review B*, 43(6):4565–4572, 1991.

[78] Matteo Altissimo. E-beam lithography for micro-/nanofabrication. *Biomicrofluidics*, 4(2):2–7, 2010.

[79] Khalid Salaita, Yuhuang Wang, and Chad a Mirkin. Applications of dip-pen nanolithography. *Nature nanotechnology*, 2(3):145–155, 2007.

[80] David S. Ginger, Hua Zhang, and Chad A. Mirkin. The evolution of dip-pen nanolithography. *Angewandte Chemie International Edition*, 43(1):30–45, 2004.

[81] Joachim P. Spatz and Martin Möller. Gold nanoparticles in micellar poly(styrene)-b-poly(ethylene oxide) filmssize and interparticle distance control in monoparticulate films. pages 337–340, 1996.

[82] J K W Yang, Y S Jung, J B Chang, R A Mickiewicz, A Alexander-Katz, C A Ross, and K K Berggren. Complex self-assembled patterns using sparse commensurate templates with locally varying motifs. *Nature Nanotechnology*, 5(4):256–260, 2010.

[83] K G A Tavakkoli, K W Gotrik, A F Hannon, A Alexander-Katz, C A Ross, and K K Berggren. Templating Three-Dimensional Self-Assembled Structures in Bilayer Block Copolymer Films. *Science*, 336(6086):1294–1298, 2012.

[84] Theobald Lohmüller, Michael Helgert, Michael Sundermann, Robert Brunner, and Joachim P. Spatz. Biomimetic interfaces for high-performance optics in the deep-UV light range. *Nano Letters*, 8(5):1429–1433, 2008.

[85] Elisabetta Ada Cavalcanti-Adam, Tova Volberg, Alexandre Micoulet, Horst Kessler, Benjamin Geiger, and Joachim Pius Spatz. Cell Spreading and Focal Adhesion Dynamics Are Regulated by Spacing of Integrin Ligands. *Biophysical Journal*, 92(8):2964–2974, 2007.

[86] Joachim P Spatz, Sheiko Sergei, and M Ller Martin. Ion-Stabilized Block Copolymer Micelles: Film Formation and Intermicellar Interaction. *Macromolecules*, 29:3220–3226, 1996.

[87] Zhisheng Gao, Xing Fu Zhong, and Adi Eisenberg. Chain dynamics in coronas of ionomer aggregates. *Macromolecules*, 27:794–802, 1994.

[88] L Zhang and a Eisenberg. Multiple Morphologies of "Crew-Cut" Aggregates of Polystyrene-b-poly(acrylic acid) Block Copolymers. *Science (New York, N.Y.)*, 268(5218):1728–1731, 1995.

[89] Z S Gao and a Eisenberg. A Model of Micellization for Block-Copolymers in Solutions. *Macromolecules*, 26(cmc):7353–7360, 1993.

[90] K a Cogan, a P Gast, and M Capel. Stretching and Scaling in Polymeric Micelles. *Macromolecules*, 24:6512–6520, 1991.

[91] Lena J M Vagberg, Kathleen a Cogan, and Alice P Gast. Light-scattering study of starlike polymeric micelles. *Macromolecules*, 24:1670–1677, 1991.

[92] Theobald Lohmueller, Eva Bock, and Joachim P Spatz. Synthesis of Quasi-Hexagonal Ordered Arrays of Metallic Nanoparticles with Tuneable Particle Size. *Advanced Materials*, 20(12):2297–2302, 2008.

[93] Antony S Dimitrov and Kuniaki Nagayama. Continuous Convective Assembling of Fine Particles into Two-Dimensional Arrays on Solid Surfaces. *Langmuir*, 12(5):1303–1311, 1996.

[94] N Denkov, O Velev, P Kralchevski, I Ivanov, H Yoshimura, and K Nagayama. Mechanism of formation of two-dimensional crystals from latex particles on substrates. *Langmuir*, 8(12):3183–3190, 1992.

[95] N. D. Denkov, O. D. Velev, P. a. Kralchevsky, I. B. Ivanov, H. Yoshimura, and K. Nagayama. Two-dimensional crystallization, 1993.

[96] M. Haupt, S. Miller, a. Ladenburger, R. Sauer, K. Thonke, J. P. Spatz, S. Riethmüller, M. Möller, and F. Banhart. Semiconductor nanostructures defined

with self-organizing polymers. *Journal of Applied Physics*, 91(9):6057–6059, 2002.

[97] Marco Arnold, Vera C. Hirschfeld-Warneken, Theobald Lohmuller, Patrick Heil, Jacques Blummel, Elisabetta A. Cavalcanti-Adam, Monica Lopez-Garcia, Paul Walther, Horst Kessler, Benjamin Geiger, and Joachim P. Spatz. Induction of Cell Polarization and Migration by a Gradient of Nanoscale Variations in Adhesive Ligand Spacing. *Nano Letters*, 8(7):2063–2069, 2008.

[98] P A Kralchevsky and K Nagayama. Capillary interactions between particles bound to interfaces, liquid films and biomembranes. *Advances in Colloid and Interface Science*, 85(2-3):145–192, 2000.

[99] DONALD F. GERSON, J. E. ZAJIC, and M. D. OUCHI. *The Relation of Surfactant Properties to the Extraction of Bitumen from Athabasca Tar Sand by a SolventAqueous-Surfactant Process*, chapter 7, pages 66–79. 1979.

[100] J. D. Henry, M. E. Prudich, and K. R. Vaidyanathan. Novel Separation Processes for Solid/Liquid Separations in Coal Derived Liquids. *Separation & Purification Reviews*, 8(2):81–118, 1979.

[101] MM Nicolson. The interaction between floating particles. *Mathematical Proceedings of the Cambridge Philosophical Society*, 45(02):288–295, 1949.

[102] P.a Kralchevsky, V.N Paunov, I.B Ivanov, and K Nagayama. Capillary meniscus interaction between colloidal particles attached to a liquidfluid interface. *Journal of Colloid and Interface Science*, 151(1):79–94, 1992.

[103] M A Fortes. Attraction and repulsion of floating particles. *Canadian Journal of Chemistry*, 60(23):2889–2895, 1982.

[104] D.Y.C Chan, J.D Henry jr., and L.R White. The interaction of colloidal particles collected at fluid interfaces. *Journal of Colloid and Interface Science*, 79(2):410 – 418, 1981.

[105] V N Paunov, P A Kralchevsky, N D Denkov, and K Nagayama. Lateral Capillary Forces Between Floating Submillimeter Particles, 1993.

[106] Peter a Kralchevsky and Kuniaki Nagayama. Capillary forces between colloidal particles. *Langmuir*, 10(1):23–36, 1994.

[107] KC Keir C Neuman and Attila Nagy. Single-molecule force spectroscopy: optical tweezers, magnetic tweezers and atomic force microscopy. *Nature methods*, 5(6):491–505, 2008.

[108] R Conroy. Force Spectroscopy with Optical. 1970.

[109] B Drake, C B Prater, a L Weisenhorn, S a Gould, T R Albrecht, C F Quate, D S Cannell, H G Hansma, and P K Hansma. Imaging crystals, polymers, and processes in water with the atomic force microscope. *Science (New York, N.Y.)*, 243(4898):1586–1589, 1989.

[110] M Benoit, D Gabriel, G Gerisch, and H E Gaub. Discrete interactions in cell adhesion measured by single-molecule force spectroscopy. *Nature cell biology*, 2(6):313–7, jun 2000.

[111] Jonne Helenius, Carl-Philipp Heisenberg, Hermann E Gaub, and Daniel J Muller. Single-cell force spectroscopy. *Journal of cell science*, 121(Pt 11):1785–91, jun 2008.

[112] C. M. Franz and P.-H. Puech. Atomic Force Microscopy: A Versatile Tool for Studying Cell Morphology, Adhesion and Mechanics. *Cellular and Molecular Bioengineering*, 1(4):289–300, dec 2008.

[113] Jens Friedrichs, Kyle R. Legate, Rajib Schubert, Mitasha Bharadwaj, Carsten Werner, Daniel J. Müller, and Martin Benoit. A practical guide to quantify cell adhesion using single-cell force spectroscopy. *Methods*, 60(2):169–178, 2013.

[114] Mingzhai Sun, John S Graham, Balazs Hegedüs, Françoise Marga, Ying Zhang, Gabor Forgacs, and Michel Grandbois. Multiple membrane tethers probed by atomic force microscopy. *Biophysical journal*, 89(6):4320–9, 2005.

[115] Christine Selhuber-Unkel, Mónica López-García, Horst Kessler, and Joachim P Spatz. Cooperativity in adhesion cluster formation during initial cell adhesion. *Biophysical journal*, 95(11):5424–5431, 2008.

[116] Warren D Marcus, Rodger P McEver, and Cheng Zhu. Forces required to initiate membrane tether extrusion from cell surface depend on cell type but not on the surface molecule. *Mechanics & chemistry of biosystems : MCB*, 1(4):245–51, 2004.

[117] Michael C Brown and Christopher E Turner. Paxillin: adapting to change. *Physiological reviews*, 84(4):1315–1339, 2004.

[118] Benjamin Geiger and Kenneth M. Yamada. Molecular architecture and function of matrix adhesions. *Cold Spring Harbor perspectives in biology*, 3(5):1–21, 2011.

[119] Ronen Zaidel-bar, Shalev Itzkovitz, Avi Ma, Ravi Iyengar, and Benjamin Geiger. Adhesion. 9(8), 2007.

[120] F Grinnell. Wound repair, keratinocyte activation and integrin modulation. *Journal of cell science*, 101 (Pt 1:1–5, 1992.

[121] Nancy Hogg, Melanie Laschinger, Katherine Giles, and Alison McDowall. T-cell integrins: more than just sticking points. *Journal of cell science*, 116:4695–4705, 2003.

[122] R Zaidel-Bar, M Cohen, L Addadi, and B Geiger. Hierarchical assembly of cell-matrix adhesion complexes. *Biochemical Society transactions*, 32(Pt3):416–420, 2004.

[123] Haguy Wolfenson, Irena Lavelin, and Benjamin Geiger. Dynamic Regulation of the Structure and Functions of Integrin Adhesions. *Developmental Cell*, 24(5):447–458, 2013.

[124] R. Zaidel-Bar and B. Geiger. The switchable integrin adhesome. *Journal of Cell Science*, 123(9):1385–1388, 2010.

[125] Simone Weis, Ted T. Lee, Aránzazu del Campo, and Andrés J. García. Dynamic cell-adhesive microenvironments and their effect on myogenic differentiation. *Acta Biomaterialia*, 9(9):8059–8066, 2013.

[126] Ted T. Lee, José R. García, Julieta I. Paez, Ankur Singh, Edward A. Phelps, Simone Weis, Zahid Shafiq, Asha Shekaran, Aránzazu del Campo, and Andrés J. García. Light-triggered in vivo activation of adhesive peptides regulates cell adhesion, inflammation and vascularization of biomaterials. *Nature Materials*, 14(3):352–360, 2014.

[127] Melanie Wirkner, José María Alonso, Verona Maus, Marcelo Salierno, Ted T Lee, Andrés J García, and Aránzazu del Campo. Triggered cell release from materials using bioadhesive photocleavable linkers. *Advanced materials (Deerfield Beach, Fla.)*, 23(34):3907–10, sep 2011.

[128] Claudio G. Rolli, Hidekazu Nakayama, Kazuo Yamaguchi, Joachim P. Spatz, Ralf Kemkemer, and Jun Nakanishi. Switchable adhesive substrates: Revealing

geometry dependence in collective cell behavior. *Biomaterials*, 33(8):2409–2418, 2012.

[129] Woon Seok Yeo, Muhammad N. Yousaf, and Milan Mrksich. Dynamic Interfaces between Cells and Surfaces: Electroactive Substrates that Sequentially Release and Attach Cells. *Journal of the American Chemical Society*, 125(49):14994–14995, 2003.

[130] C Selhuber-Unkel, T Erdmann, M López-García, H Kessler, U S Schwarz, and J P Spatz. Cell adhesion strength is controlled by intermolecular spacing of adhesion receptors. *Biophysical journal*, 98(4):543–51, feb 2010.

[131] C Ballestrem, B Hinz, B a Imhof, and B Wehrle-Haller. Marching at the front and dragging behind: differential alphaVbeta3-integrin turnover regulates focal adhesion behavior. *The Journal of cell biology*, 155(7):1319–32, dec 2001.

[132] Wiktor Szymaski, John M. Beierle, Hans a V Kistemaker, Willem a. Velema, and Ben L. Feringa. Reversible photocontrol of biological systems by the incorporation of molecular photoswitches. *Chemical Reviews*, 113(8):6114–6178, 2013.

[133] Melanie Wirkner, José María Alonso, Verona Maus, Marcelo Salierno, Ted T Lee, Andrés J García, and Aránzazu Del Campo. Triggered Cell Release from Materials Using Bioadhesive Photocleavable Linkers. *Advanced materials (Deerfield Beach, Fla.)*, pages 3907–3910, may 2011.

[134] Jun Nakanishi, Yukiko Kikuchi, Tohru Takarada, Hidekazu Nakayama, Kazuo Yamaguchi, and Mizuo Maeda. Photoactivation of a substrate for cell adhesion under standard fluorescence microscopes. *Journal of the American Chemical Society*, 126(50):16314–16315, 2004.

[135] Jun Nakanishi, Yukiko Kikuchi, Tohru Takarada, Hidekazu Nakayama, Kazuo Yamaguchi, and Mizuo Maeda. Spatiotemporal control of cell adhesion on a self-assembled monolayer having a photocleavable protecting group. *Analytica Chimica Acta*, 578(1):100–104, 2006.

[136] Aya Mizutani, Akihiko Kikuchi, Masayuki Yamato, Hideko Kanazawa, and Teruo Okano. Preparation of thermoresponsive polymer brush surfaces and their interaction with cells. *Biomaterials*, 29:2073–2081, 2008.

[137] Martin A. Cole, Nicolas H. Voelcker, Helmut Thissen, and Hans J. Griesser. Stimuli-responsive interfaces and systems for the control of proteinsurface and cellsurface interactions. *Biomaterials*, 30(9):1827–1850, 2009.

[138] Kevin G Yager and Christopher J Barrett. Azobenzene Polymers as Photomechanical and Multifunctional Smart Materials. pages 424–446.

[139] Kevin G. Yager and Christopher J. Barrett. Novel photo-switching using azobenzene functional materials. *Journal of Photochemistry and Photobiology A: Chemistry*, 182(3):250–261, sep 2006.

[140] Hideko Koshima, Naoko Ojima, and Hidetaka Uchimoto. Mechanical motion of azobenzene crystals upon photoirradiation. *Journal of the American Chemical Society*, 131(20):6890–6891, 2009.

[141] Estbaliz Merino and Maria Ribagorda. Control over molecular motion using the cis-trans photoisomerization of the azo group. *Beilstein Journal of Organic Chemistry*, 8:1071–1090, 2012.

[142] H Rau, E. Lddecke, H. Nitsch, and H. Patzelt. The mechanism of photoisomerization of azobenzenes. *Bulletin des Socits Chimiques Belges*, 91(5):475–475, 1982.

[143] Michael a Kienzler, Andreas Reiner, Eric Trautman, Stan Yoo, Dirk Trauner, and Ehud Y Isacoff. A red-shifted, fast-relaxing azobenzene photoswitch for visible light control of an ionotropic glutamate receptor. *Journal of the American Chemical Society*, 135(47):17683–6, 2013.

[144] Norio Nishimura, Toshinobu Sueyoshi, Hideyuki Yamanaka, Etsuko Imai, Shunzo Yamamoto, and Shigeo Hasegawa. Thermal Cis-to-Trans Isomerization of Substituted Azobenzenes II. Substituent and Solvent Effects, 1976.

[145] Kirk S Schanze, T Fleming Mattox, and David G Whitten. Solvent effects on the thermal cis-trans isomerization and charge-transfer absorption of 4-(diethylamino)-4'-nitroazobenzene. *Journal of Organic Chemistry*, 48(17):2808–2813, 1983.

[146] Maria-Melanie Russew and Stefan Hecht. Photoswitches: From Molecules to Materials. *Advanced Materials*, 22(31):3348–3360, 2010.

[147] Jonathan D Humphries, Adam Byron, and Martin J Humphries. Integrin ligands at a glance. *Journal of Cell Science*, 119(19):3901–3903, 2006.

[148] Jörg Auernheimer, Claudia Dahmen, Ulrich Hersel, Andreas Bausch, and Horst Kessler. Photoswitched cell adhesion on surfaces with RGD peptides. *Journal of the American Chemical Society*, 127(46):16107–10, nov 2005.

[149] Alexis Goulet-Hanssens, Karen Lai Wing Sun, Timothy E. Kennedy, and Christopher J. Barrett. Photoreversible surfaces to regulate cell adhesion. *Biomacromolecules*, 13(9):2958–2963, 2012.

[150] Dingbin Liu, Yunyan Xie, Huawu Shao, and Xingyu Jiang. Using azobenzene-embedded self-assembled monolayers to photochemically control cell adhesion reversibly. *Angewandte Chemie International Edition*, 48(24):4406–4408, 2009.

[151] S O Lock, J V Fmend, and Colworth House. Phototoxicity Testing in Vitro : Evaluation of Mammalian Cell Culture Techniques. 24(6):789–793, 1986.

[152] Jort Robertus, Wesley R. Browne, and Ben L. Feringa. Dynamic control over cell adhesive properties using molecular-based surface engineering strategies. *Chem. Soc. Rev.*, 39(1):354–378, 2010.

[153] Andrew a Beharry and G Andrew Woolley. Azobenzene photoswitches for biomolecules. *Chemical Society reviews*, 40(8):4422–4437, 2011.

[154] Gökçen Birlik Demirel, Nursel Dilsiz, Mehmet Ali Ergün, Mehmet Çakmak, and Tuncer Çaykara. Photocontrollable DNA hybridization on reversibly photoresponsive surfaces. *Journal of Materials Chemistry*, 21(28):10415, 2011.

[155] J Xu, G Zhang, Q Wu, Y Liang, S Liu, Q Sun, X Chen, and Y Shen. Holographic recording and light amplification in doped polymer film. *Optics letters*, 20(5):504–506, 1995.

[156] Claudia Poloni, Wiktor Szymaski, Lili Hou, Wesley R. Browne, and Ben L. Feringa. A Fast, Visible-Light-Sensitive Azobenzene for Bioorthogonal Ligation. *Chemistry - A European Journal*, 20(4):946–951, 2014.

[157] Gautam Banerjee, Nishma Gupta, Arun Kapoor, and Govindarajan Raman. UV induced bystander signaling leading to apoptosis. *Cancer Letters*, 223(2):275–284, 2005.

[158] T. J. McMillan, E. Leatherman, A. Ridley, J. Shorrocks, S. E. Tobi, and J. R. Whiteside. Cellular effects of long wavelength uv light (uva) in mammalian cells. *Journal of Pharmacy and Pharmacology*, 60(8):969–976, 2008.

[159] Sebastian Kruss, Tobias Wolfram, Raquel Martin, Stefanie Neubauer, Horst Kessler, and Joachim P Spatz. Stimulation of cell adhesion at nanostructured teflon interfaces. *Advanced materials (Deerfield Beach, Fla.)*, 22(48):5499–506, dec 2010.

[160] Joachim P. Spatz, Stefan Mössmer, Christoph Hartmann, Martin Möller, Thomas Herzog, Michael Krieger, Hans Gerd Boyen, Paul Ziemann, and Bernd Kabius. Ordered deposition of inorganic clusters from micellar block copolymer films. *Langmuir*, 16(6):407–415, 2000.

[161] Stefan V. Graeter, Jinghuan Huang, Nadine Perschmann, Mónica López-García, Horst Kassler, Jiandong Ding, and Joachim P. Spatz. Mimicking cellular environments by nanostructured soft interfaces. *Nano Letters*, 7(5):1413–1418, 2007.

[162] Christine Selhuber, Jacques Blümmel, Fabian Czerwinski, and Joachim P Spatz. Tuning surface energies with nanopatterned substrates. *Nano letters*, 6(2):267–70, 2006.

[163] Marco Arnold, Elisabetta Ada Cavalcanti-Adam, Roman Glass, Jacques Blümmel, Wolfgang Eck, Martin Kantlehner, Horst Kessler, and Joachim P. Spatz. Activation of Integrin Function by Nanopatterned Adhesive Interfaces. *ChemPhysChem*, 5(3):383–388, 2004.

[164] Laith F. Kadem, Constanze Lamprecht, Julia Purtov, and Christine Selhuber-Unkel. Controlled Self-Assembly of Hexagonal Nanoparticle Patterns on Nanotopographies. *Langmuir*, 31(34):9261–9265, 2015.

[165] C S Chen, M Mrksich, S Huang, G M Whitesides, and D E Ingber. Geometric control of cell life and death. *Science (New York, N.Y.)*, 276(5317):1425–1428, 1997.

[166] Thomas Blttler, Christoph Huwiler, Mirjam Ochsner, Brigitte Stdler, Harun Solak, Janos Vrs, and H. Michelle Grandin. Nanopatterns with biological functions. *Journal of Nanoscience and Nanotechnology*, 6(8):2237–2264, 2006-08-01T00:00:00.

[167] Tobias N. Krauss, Esther Barrena, Theobald Lohmüller, Joachim P. Spatz, and Helmut Dosch. Growth mechanisms of phthalocyanine nanowires induced by Au nanoparticle templates. *Physical Chemistry Chemical Physics*, 13(13):5940, 2011.

[168] R. Glass, M. Arnold, J. Blümmel, a. Küller, M. Möller, and J.P. Spatz. Micro-Nanostructured Interfaces Fabricated by the Use of Inorganic Block Copolymer Micellar Monolayers as Negative Resist for Electron-Beam Lithography. *Advanced Functional Materials*, 13(7):569–575, jul 2003.

[169] Daniel Aydin, Marco Schwieder, Ilia Louban, Stefan Knoppe, Jens Ulmer, Tobias L Haas, Henning Walczak, and Joachim P Spatz. Micro-nanostructured protein arrays: a tool for geometrically controlled ligand presentation. *Small (Weinheim an der Bergstrasse, Germany)*, 5(9):1014–8, may 2009.

[170] Janosch a Deeg, Ilia Louban, Daniel Aydin, Christine Selhuber-Unkel, Horst Kessler, and Joachim P Spatz. Impact of local versus global ligand density on cellular adhesion. *Nano letters*, 11(4):1469–76, apr 2011.

[171] Roman Glass, Martin M ller, and Joachim P Spatz. Block copolymer micelle nanolithography. *Nanotechnology*, 14(10):1153–1160, 2003.

[172] Jinghuan Huang, Stefan V Gräter, Francesca Corbellini, Sabine Rinck-jahnke, Ralf Kemkemer, Horst Kessler, Jiandong Ding, and Joachim P Spatz. NIH Public Access. 9(3):1111–1116, 2010.

[173] Christian Williges, Wenwen Chen, Christoph Morhard, Joachim P Spatz, and Robert Brunner. Increasing the order parameter of quasi-hexagonal micellar nanostructures by ultrasound annealing. *Langmuir : the ACS journal of surfaces and colloids*, 29(4):989–93, 2013.

[174] Mariela J Pavan and Roy Shenhar. Two-dimensional nanoparticle organization using block copolymer thin films as templates. *Journal of Materials Chemistry*, pages 2028–2040, 2011.

[175] Jiyoung Hwang, June Huh, Bumsuk Jung, Jae-Min Hong, Min Park, and Cheolmin Park. Highly ordered microstructures of poly(styrene–isoprene) block copolymers induced by solution meniscus. *Polymer*, 46(21):9133–9143, 2005.

[176] Yong Luo. *Nanostructures design and fabrication for magnetic storage applications*. PhD thesis, North Carolina State University, 2008.

[177] Sven Hüttner, Michael Sommer, Arnaud Chiche, Georg Krausch, Ullrich Steiner, and Mukundan Thelakkat. Controlled solvent vapour annealing for polymer electronics. *Soft Matter*, 5(21):4206, 2009.

[178] Joachim P Spatz, Sheiko Sergei, and M Ller Martin. Ion-Stabilized Block Copolymer Micelles: Film Formation and Intermicellar Interaction. *Macromolecules*, 29:3220–3226, 1996.

[179] Y. Zhao, Z. Y. Xie, Y. Qu, Y. H. Geng, and L. X. Wang. Effects of thermal annealing on polymer photovoltaic cells with buffer layers and in situ formation of interfacial layer for enhancing power conversion efficiency. *Synthetic Metals*, 158:908–911, 2008.

[180] W. Ma, C. Yang, X. Gong, K. Lee, and A.J. Heeger. Thermally stable, efficient polymer solar cells with nanoscale control of the interpenetrating network morphology. *Advanced Functional Materials*, 15(10):1617–1622, 2005.

[181] Eva Oktavia Ningrum, Chien-Chih Chang, and Chieh-Tsung Lo. Effect of solvent annealing on the nano- and micro-structure of block copolymer thin film. *Journal of Macromolecular Science, Part B*, 50(7):1298–1312, 2011.

[182] Tae Hee Kim, June Huh, Jiyoung Hwang, Ho Cheol Kim, Seung Hyun Kim, Beong Hyeok Sohn, and Park Cheolmin. Ordered arrays of PS-b-P4VP micelles by fusion and fission process 7 upon solvent annealing. *Macromolecules*, 42(17):6688–6697, 2009.

[183] Manesh Gopinadhan, Pawe W. Majewski, Youngwoo Choo, and Chinedum O. Osuji. Order-disorder transition and alignment dynamics of a block copolymer under high magnetic fields by in situ X-ray scattering. *Physical Review Letters*, 110(7):1–5, 2013.

[184] Jinghuan Huang, SV Grater, Francesca Corbellini, and Sabine Rinck. Impact of order and disorder in RGD nanopatterns on cell adhesion. *Nano ...*, 2009.

[185] Laith F. Kadem, Michelle Holz, Kristine Grace Suana, Qian Li, Constanze Lamprecht, Rainer Herges, and Christine Selhuber-Unkel. Rapid Reversible Photoswitching of Integrin-Mediated Adhesion at the Single-Cell Level. *Advanced Materials*, 28(9):1799–1802, 2016.

[186] Wei Li, Zhaowei Chen, Li Zhou, Zhenhua Li, Jinsong Ren, and Xiaogang Qu. Noninvasive and Reversible Cell Adhesion and Detachment via Single-Wavelength Near-Infrared Laser Mediated Photoisomerization. *Journal of the American Chemical Society*, 137(25):8199–8205, 2015.

[187] Jacques Blümmel, Nadine Perschmann, Daniel Aydin, Jovana Drinjakovic, Thomas Surrey, Monica Lopez-Garcia, Horst Kessler, and Joachim P. Spatz. Protein repellent properties of covalently attached PEG coatings on nanostructured SiO2-based interfaces. *Biomaterials*, 28(32):4739–4747, 2007.

[188] M Kantlehner, P Schaffner, D Finsinger, J Meyer, A Jonczyk, B Diefenbach, B Nies, G Hölzemann, S L Goodman, and H Kessler. Surface coating with cyclic RGD peptides stimulates osteoblast adhesion and proliferation as well as bone formation. *Chembiochem : a European journal of chemical biology*, 1:107–114, 2000.

[189] Franziska C. Schenk, Heike Boehm, Joachim P. Spatz, and Seraphine V. Wegner. Dual-functionalized nanostructured biointerfaces by click chemistry. *Langmuir*, 30(23):6897–6905, 2014.

[190] David T. Valley, Matthew Onstott, Sergey Malyk, and Alexander V. Benderskii. Steric hindrance of photoswitching in self-assembled monolayers of azobenzene and alkane thiols. *Langmuir*, 29(37):11623–11631, 2013.

[191] Belinda Baisch, Diego Raffa, Ulrich Jung, Olaf M. Magnussen, Cyril Nicolas, Jerome Lacour, Jens Kubitschke, and Rainer Herges. Mounting freestanding molecular functions onto surfaces: The platform approach. *Journal of the American Chemical Society*, 131(2):442–443, 2009.

[192] Oliver Seitz, Poornika G. Fernandes, Ruhai Tian, Nikhil Karnik, Huang-Chun Wen, Harvey Stiegler, Richard a. Chapman, Eric M. Vogel, and Yves J. Chabal. Control and stability of self-assembled monolayers under biosensing conditions. *Journal of Materials Chemistry*, 21(12):4384, 2011.

[193] D. Tsiourvas, a. Tsetsekou, M. Arkas, S. Diplas, and E. Mastrogianni. Covalent attachment of a bioactive hyperbranched polymeric layer to titanium surface for the biomimetic growth of calcium phosphates. *Journal of Materials Science: Materials in Medicine*, 22(1):85–96, 2011.

[194] Clemens M Franz, Anna Taubenberger, Pierre-Henri Puech, and Daniel J Muller. Studying Integrin-Mediated Cell Adhesion at the Single-Molecule Level Using AFM Force Spectroscopy. *Sci. STKE*, 2007(406):pl5–, 2007.

[195] Dennis E Discher, Paul Janmey, and Yu-Li Wang. Tissue cells feel and respond to the stiffness of their substrate. *Science (New York, N.Y.)*, 310(5751):1139–43, 2005.

[196] Raja Paul, Patrick Heil, Joachim P. Spatz, and Ulrich S. Schwarz. Propagation of Mechanical Stress through the Actin Cytoskeleton toward Focal Adhesions: Model and Experiment. *Biophysical Journal*, 94(4):1470–1482, 2008.

[197] Alex Carisey, Ricky Tsang, Alexandra M. Greiner, Nadja Nijenhuis, Nikki Heath, Alicja Nazgiewicz, Ralf Kemkemer, Brian Derby, Joachim Spatz, and Christoph Ballestrem. Vinculin regulates the recruitment and release of core focal adhesion proteins in a force-dependent manner. *Current Biology*, 23(4):271–281, 2013.

[198] Wylie W. Ahmed, Tobias Wolfram, Alexandra M. Goldyn, Kristina Bruellhoff, Borja Arags Rioja, Martin Mueller, Joachim P. Spatz, Taher A. Saif, Juergen Groll, and Ralf Kemkemer. Myoblast morphology and organization on biochemically micro-patterned hydrogel coatings under cyclic mechanical strain. *Biomaterials*, 31(2):250–258, 2010.

[199] Thorsten Hugel, Nolan B Holland, Anna Cattani, Luis Moroder, Markus Seitz, and Hermann E Gaub. Single-molecule optomechanical cycle. *Science (New York, N.Y.)*, 296(5570):1103–1106, 2002.

[200] Nolan B. Holland, Thorsten Hügel, Gregor Neuert, Anna Cattani-Scholz, Christian Renner, Dieter Oesterhelt, Luis Moroder, Markus Seitz, and Hermann E. Gaub. Single molecule force spectroscopy of azobenzene polymers: Switching elasticity of single photochromic macromolecules. *Macromolecules*, 36(6):2015–2023, 2003.

[201] Yu Shiu Lo, Jack Simons, and Thomas P. Beebe. Temperature dependence of the biotin-avidin bond-rupture force studied by atomic force microscopy. *Journal of Physical Chemistry B*, 106(1):9847–9852, 2002.

[202] Ediz Sariisik, Cvetan Popov, Jochen P. Müller, Denitsa Docheva, Hauke Clausen-Schaumann, and Martin Benoit. Decoding Cytoskeleton-Anchored and Non-Anchored Receptors from Single-Cell Adhesion Force Data. *Biophysical Journal*, 109(7):1330–1333, 2015.

[203] C. M. O'Connor and J. U Adams. Essentials of cell biology, 2010.

[204] Matthias Chiquet, Laurent Gelman, Roman Lutz, and Silke Maier. From mechanotransduction to extracellular matrix gene expression in fibroblasts. *Biochimica et Biophysica Acta - Molecular Cell Research*, 1793(5):911–920, 2009.

[205] Kyung Shin Kang, Seung Jae Lee, Hak Sue Lee, Wonkyu Moon, and Dong Woo Cho. Effects of combined mechanical stimulation on the proliferation and differentiation of pre-osteoblasts. *Experimental & molecular medicine*, 43(6):367–373, 2011.

[206] Samer Alam, David B. Lovett, Richard B. Dickinson, Kyle J. Roux, and Tanmay P. Lele. Nuclear forces and cell mechanosensing. *Progress in Molecular Biology and Translational Science*, 126:205–215, 2014.

[207] Ulrich S. Schwarz, Thorsten Erdmann, and Ilka B. Bischofs. Focal adhesions as mechanosensors: The two-spring model. *BioSystems*, 83(2-3 SPEC. ISS.):225–232, 2006.

[208] George Argyrous. *Statistic for research*. 2011.

[209] Jeffrey L. Hutter and John Bechhoefer. Calibration of atomic force microscope tips. *Review of Scientific Instruments*, 64(7):1868–1873, 1993.

[210] D Braun and P Fromherz. Invited paper Fluorescence interference-contrast microscopy of cell adhesion on oxidized silicon. 348:341–348, 1997.

[211] R Haubner, D Finsinger, and H Kessler. Stereoisomeric Peptide Libraries and Peptidomimetics for Designing Selective Inhibitors of the Alpha(V)beta(3) Integrin for a New Cancer Therapy. *Ang Chem Int Ed*, 36(13-14):1375–1389, 1997.

[212] Tatiana Zubkov, André C B Lucassen, Dalia Freeman, Yishay Feldman, Sidney R Cohen, Guennadi Evmenenko, Pulak Dutta, and M E van der Boom. Photoinduced deprotection and ZnO patterning of hydroxyl-terminated siloxane-based monolayers. *The journal of physical chemistry. B*, 109(29):14144–53, 2005.

[213] J H Moon, J W Shin, S Y Kim, and J W Park. Formation of uniform aminosilane thin layers: An imine formation to measure relative surface density of the amine group. *Langmuir*, 12(20):4621–4624, 1996.

[214] Yu-shiu Lo, Neil D Huefner, Winter S Chan, Forrest Stevens, Joel M Harris, and Thomas P Beebe. Specific Interactions between Biotin and Avidin Studied by Atomic Force Microscopy Using the Poisson Statistical Analysis Method. *Langmuir*, 15(20):1373–1382, 1999.

Appendix-A

A.1 Independent samples t test

The independent samples t test, also known as the independent t test or alternatively the student t test, is a statistical tool employed to compare the means of two independent populations. This comparison provides evidence on whether the associated population means are significantly different. In order to perform the independent t test, two independent samples, i.e. independent of observations, are required. Also, there should be no relationship between the data of each group, i.e. data of each group can neither influence the other groups data nor replace them. The independent samples t test can be conducted in one of two forms, namely the one-tail or the two-tails tests[208]. Both tests will be presented below and the differences will be discussed.

In the one-tail independent t test, two hypotheses are proposed: The null hypothesis H_0 and the alternative hypothesis H_1. Both hypotheses are presented as follows

$$\begin{aligned} H_0 &: M_1 = M_2 \\ H_1 &: M_1 > M_2 \end{aligned} \tag{1}$$

where M_1 and M_2 are the means of group 1 and 2, respectively. The test statistic (t-value) in an independent t test is calculated as

$$t = \frac{M_1 - M_2}{\sqrt{\frac{S_1^2}{n_1} + \frac{S_2^2}{n_2}}} \tag{2}$$

where S_1^2 and S_2^2 are the variances and n_1 and n_1 are sample sizes of group 1 and 2, respectively (Fig. Appendix-A.1). In order to calculate the variance, we need to determine the deviation which can be obtained as follows: First, the mean value is

subtracted from the inputs within the sample size, i.e. $(n - mean)$ (Fig. Appendix-A.1). Then, the $(n - mean)$ value is squared (Fig. Appendix-A.1), i.e. $(n - mean)^2$, and the sum of all $(n - mean)^2$ values is calculated, i.e. $\sum(n - mean)^2$. Finally, the variance can be determined by dividing the sum value by the degree of freedom $(n-1)$ as shown below

$$S^2 = \frac{\sum(n - mean)^2}{n - 1} \tag{3}$$

n	n - mean	(n - mean)²
n1	n1 - mean	(n1 - mean)²
n2	n2 - mean	(n2 - mean)²
n3	n3 - mean	(n3 - mean)²
n4	n4 - mean	(n4 - mean)²
n5	n5 - mean	(n5 - mean)²
n6	n6 - mean	(n6 - mean)²
n7	n7 - mean	(n7 - mean)²
n8	n8 - mean	(n8 - mean)²
n9	n9 - mean	(n9 - mean)²

Figure Appendix-A.1: *Exemplary table of data demonstrating the steps needed to calculate the deviation.*

Having calculated the S^2 value of each group, the t-value will be simply determined using equation 2.

In order to reach an appropriate conclusion on whether a statistical difference between the two groups in the test exists, the p-value is needed. The p-value is the probability that the null hypothesis is true for the observed result. Thus, the smaller the p-value the more significant the difference is. Each p-vlaue corresponds to a defined t-value which can be obtained from Fig. Appendix-A.2.

In a one-tail t test under the hypothesis that M1 is larger than M2, the p-value is the shaded yellow area under the distribution curve in Fig. Appendix-A.3 a[208].

However, the p-value is double the shaded area in a two-tail independent test, i.e. the sum of both shaded areas under the distribution curve. In a two-tail t test, the

df	one tail	0.25	0.1	0.05	0.025	0.01	0.005	0.001
	two tails	0.5	0.2	0.1	0.05	0.02	0.01	0.002
1		1	3.078	6.314	12.706	31.821	63.657	318.309
2		0.816	1.886	2.92	4.303	6.965	9.925	22.327
3		0.765	1.638	2.353	3.182	4.541	5.841	10.215
4		0.741	1.533	2.132	2.776	3.747	4.604	7.173
5		0.727	1.476	2.015	2.571	3.365	4.032	5.893
6		0.718	1.44	1.943	2.447	3.143	3.707	5.208
7		0.711	1.415	1.895	2.365	2.998	3.499	4.785
8		0.706	1.397	1.86	2.306	2.896	3.355	4.501
9		0.703	1.383	1.833	2.262	2.821	3.25	4.297
10		0.7	1.372	1.812	2.228	2.764	3.169	4.144
11		0.697	1.363	1.796	2.201	2.718	3.106	4.025
12		0.695	1.356	1.782	2.179	2.681	3.055	3.93
13		0.694	1.35	1.771	2.16	2.65	3.012	3.852
14		0.692	1.345	1.761	2.145	2.624	2.977	3.787
15		0.691	1.341	1.753	2.131	2.602	2.947	3.733
16		0.69	1.337	1.746	2.12	2.583	2.921	3.686
17		0.689	1.333	1.74	2.11	2.567	2.898	3.646
18		0.688	1.33	1.734	2.101	2.552	2.878	3.61
19		0.688	1.328	1.729	2.093	2.539	2.861	3.579
20		0.687	1.325	1.725	2.086	2.528	2.845	3.552
21		0.686	1.323	1.721	2.08	2.518	2.831	3.527
22		0.686	1.321	1.717	2.074	2.508	2.819	3.505
23		0.685	1.319	1.714	2.069	2.5	2.807	3.485
24		0.685	1.318	1.711	2.064	2.492	2.797	3.467
25		0.684	1.316	1.708	2.06	2.485	2.787	3.45
26		0.684	1.315	1.706	2.056	2.479	2.779	3.435
27		0.684	1.314	1.703	2.052	2.473	2.771	3.421
28		0.683	1.313	1.701	2.048	2.467	2.763	3.408
29		0.683	1.311	1.699	2.045	2.462	2.756	3.396
30		0.683	1.31	1.697	2.042	2.457	2.75	3.385
35		0.682	1.306	1.69	2.03	2.438	2.724	3.34
40		0.681	1.303	1.684	2.021	2.423	2.704	3.307
50		0.679	1.299	1.676	2.009	2.403	2.678	3.261
60		0.679	1.296	1.671	2	2.39	2.66	3.232
120		0.677	1.289	1.658	1.98	2.358	2.617	3.16

Figure Appendix-A.2: *The corresponding t values for n degrees of freedom.*

following hypotheses are presumed

$$\begin{aligned} H_0 &: M_1 = M_2 \\ H_1 &: M_1 \neq M_2 \end{aligned} \tag{4}$$

and hence, the t-value can be either a negative or a positive value (Fig. Appendix-A.3 b).

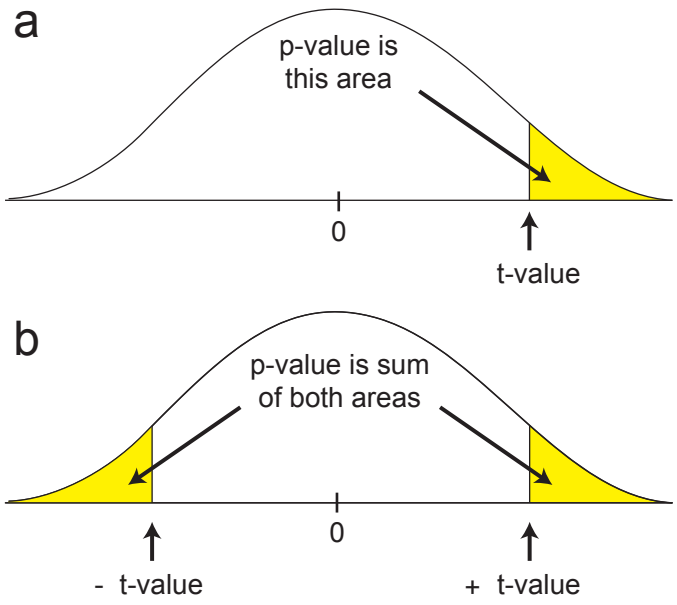

Figure Appendix-A.3: *One tail (a) versus two tail (b) independent t test. The x-axis is a set of possible results and the y-axis is the probability density. The t value together with the point where the curve cuts the x axis defines an area known as the p value.*

Appendix-B

B.1 Cantilever's spring constant calibration

B.1.1 Calculation using geometry

A theoretical calculation of the spring constant that is based on the geometry of the cantilever is the most basic method. The simplest formula for calculating the spring constant (k) is that for a rectangular and it is

$$k = \frac{E \cdot w}{4} \cdot (\frac{t}{l})^3 \tag{1}$$

where E is Young's modulus, w is width, t is thickness and l is the length of the cantilever. The resonance frequency (f) can be determined by

$$f = \frac{(1.8751)^2}{2\pi} \cdot \frac{t}{l^2} \cdot \sqrt{\frac{E}{12\rho}} \tag{2}$$

where ρ is the mass density.

Nonetheless, this method involves complications, which are difficult to overcome. Among these is the difficulty of knowing the exact geometry and material properties of a particular cantilever. Also, the cantilever's dimensions are difficult to control accurately during the manufacturing process, which implies inevitable errors in the calibration. Moreover, metal coatings can be applied onto the cantilever, which also affect the calculated spring constant due to using dissimilar materials.

B.1.2 Calculation using added mass

Adding mass to a cantilever with a well-defined weight is another technique to measure its spring constant. The method comprises adding small known weights (usually metal spheres) to the free end of the cantilever and monitor the change in the resonance frequency.

However, having an accurate added weight as well as positioning it precisely at the very end of the cantilever is a generally difficult task. The uncertainty of both the mass and position of the added weight yields errors in spring constant calculation.

B.1.3 Calculation using a reference cantilever

The spring constant of a new cantilever can be determined through a comparison with a known cantilever, i.e. reference cantilever. The calibration of the cantilever is performed by taking a force curve against a hard surface to attain the sensitivity, which is the slope obtained from the indentation part of the force curve. Then, the cantilever is pressed against the reference cantilever to acquire another force curve whose slope is compared to the other in order to obtain the spring constant as shown below

$$k = k_r(\frac{s_s}{s_r} - 1) \tag{3}$$

where k_r is the spring constant of the reference cantilever and s_s and s_r and the measured slopes on the solid surface and the reference cantilever, respectively.

In this method, it is essential to align the two cantilevers accurately so that the contact between both cantilevers only takes place at their tips. If there is a significant shift in the positioning of the two tips, a correction is need to be made as follows

$$k_{corr} = k(\frac{L}{L - \Delta L})^3 \tag{4}$$

where k_{corr} is the corrected spring constant, L is the length of the reference cantilever and ΔL is the offset between the two tips.

Because the measurement is needed to be conducted offline and separately, this method is relatively time-consuming compared to the thermal noise method that is

discussed in the next section.

B.1.4 Calculation using thermal noise analysis

This method, which was proposed in the work of Hutter *et al.*[209], is based on measuring the free fluctuation of the free end of a cantilever due to the thermal vibration. The fluctuation energy comes from the cantilever's thermal environment at, for instance, room or physiological temperatures. The thermal noise analysis has become widely used for the calibration of AFM cantilevers due to its convenience in being a passive measuring technique, which is applicable in liquid as well as *in situ.* during an experiment. However, factors such as the shape of the cantilever and details of the hydrodynamic damping affect the measurement and lead to a $5-10\,\%$ error in the calculation. Despite the consistent error, this method is fairly reliable when the main focus of the experiment is to have consistent force measurements, particularly when the same cantilever is used throughout the experiment.

The free end of the cantilever fluctuates due to the natural thermal energy in the environment. These fluctuations are of the order of 3 $\mathring{A}$ at room temperature for a soft AFM cantilever with a spring constant of around 0.05 N/m. The small deflections of the cantilever allow to approximate it as a simple harmonic oscillator with one degree of freedom. This implies that measuring the fluctuations of a freely-moving cantilever near the resonant frequency provides a good estimation of the spring constant.

A simple harmonic oscillator in equilibrium with its surrounding fluctuates due to thermal noise. The Hamiltonian of this system is

$$H = \frac{p^2}{2m} + \frac{1}{2}m\omega_0^2 q^2 \tag{5}$$

where q is oscillator displacement, p is its momentum, m is the oscillating mass and ω_0 is the resonant angular frequency. According to the equipartition theorem, the average value of each quadratic term in the Hamiltonian is equal to $k_B T/2$, where k_B is Boltzmann's constant and T is the temperature. Hence,

$$\frac{1}{2}k_B T = \left\langle \frac{1}{2}m\omega_0^2 q^2 \right\rangle \tag{6}$$

Since $\omega_0^2 = k/m$, the spring constant can be then determined using the measurement

of the mean-square spring displacement as

$$k = \frac{k_B T}{\langle q^2 \rangle} \tag{7}$$

In order to isolate the thermal oscillations from other noise sources, the data are examined in a frequency domain, which allows a study of the frequency dependence of the fluctuations. This yields a better analysis of the data at the resonance frequency, which allows to exclude low frequencies and other noises. The resonance peak of the free fluctuations when plotted against the frequency has a Lorantzian line shape. On the other hand, noise sources add a background to this thermal response. Because the noise signals are unlikely to have a resonance at the resonance frequency of the cantilever, excluding the background can be simply done. The area under the peak is then a measure of the energy in the resonance. As the integral of the area below the peak equals the mean square of the fluctuations, an estimation of the spring constant can be reached as follows

$$k = \frac{k_B T}{P} \tag{8}$$

where P represents the area under the peak and therefore the thermal fluctuations, being corrected by the noise.

Appendix-C

C.1 Microstructures

Microstructures were fabricated on single-side-polished, p-doped, 4 inch Si wafers (resistivity 130 Ωcm) that have a nominal thickness of 525 ± 25 μm (Siegert Wafer, Germany) using photolithography followed by wet etching[210]. The wafers were coated with a 1500 nm ± 5 % thermally grown oxide layer. First, the Si wafers were cleaned ultrasonically for 5 min in acetone (≥ 99.7 %, Ph.Eur., extra pure, Carl Roth, Germany) and then sonicated again in isopropanol (Rotipuran ≥ 99.8 %, p.a., ACS, ISO, Carl Roth, Germany) for another 5 min to remove the acetone before they were blown dry with N2. Before applying the photoresist, wafers were treated with HMDS (hexamethyldisilazane), which assists promoting resist adhesion. Afterwards, a positive photoresist (AZ1518, Microchemicals, Germany) was spin coated (OPTI spin ST22P, Solar-Semi, Germany) onto the wafers at 4000 rpm, resulting in a resist layer thickness of 1.8 μm. The wafers were then taken to the mask aligner (MicroTec MA 6/BA 6, Sss, Germany) and illuminated with UV light through a chromium photomask (Compugraphics Jena, Germany) consisting of 5-μm-wide stripes with a 5 μm gap between adjacent stripes. After developing with AZ 726 MIF (Microchemicals, Germany), wafers were etched for 40 s with ammonium fluoride (ammonium fluoride etching mixture, semiconductor grade Puranal, Sigma-Aldrich, Germany) to create 5-μm-wide, 60-nm-deep stripelike grooves in the silicon dioxide layer. Eventually, the rest of the photoresist on the wafers was stripped off through ultrasonic cleaning for 5 min in acetone and then another 5 min in isopropanol, and ultimately the wafers were blown dry with N2 (Fig. 2.5 a). To generate the quadruple pattern, a second set of stripes was etched into the wafers by repeating the photolithography and etching steps with the photomask rotated by 90°. This procedure results in a checkerboard structure with segments of different heights (Fig. 2.5 b)[164].

C.2 BCML on microstructures

The microstructured samples were patterned with gold particles using block copolymer micelle nanolithography. Polystyrene-b-poly-2-vinylpyridine (PS (110000)-block-P2VP (52000), 4 mg/mL, Polymer Source, Canada) was dissolved in toluene (p.A., Merck, Germany) and loaded with tetrachlorogold(III) acid trihydrate (Aldrich, Germany) in a molecular ratio of 0.4. The Si microstructures were cleaned in an acetone ultrasonic bath for 5 min followed by a 5 min ultrasonication in isopropanol. A droplet of 20 μL of the gold-loaded polymer solution was spin coated onto the microstructured Si substrate at 1000, 5000, and 7000 rpm (WS-650Mz-23NPP, Laurell, USA). To remove the micellar polymer, the spin coated, dry substrates were exposed to plasma using a mixture of hydrogen and argon gas (10 % hydrogen, 90 % argon) in a plasma etcher (TePla 100 plasma system, PVA, Germany) at 0.4 mbar and 300 W for 1 h[164]. In order to further homogenize the micelle distribution, on specific samples ultrasound annealing was carried out for 30 s as described by Williges *et al.*[173].

C.3 SEM and image analysis of micronanotopographies

Prior to SEM (Supra 55VP, Zeiss, Germany) imaging, the samples were coated with a thin layer of graphite using a sputter coater (BAL-TEC SCD 050, Capovani Brothers Inc., USA). SEM imaging was carried out at 5 kV using both in-lens and secondary electron detectors at a working distance of 3 mm. The interparticle spacing was on the one hand calculated using a custom-written Matlab routine (Matlab, Mathworks, USA), which first determined the particle density and then, assuming a perfect hexagonal particle distribution, calculated the corresponding nanoparticle spacing. On the other hand, for a more accurate measurement of interparticle spacing variations as well as for calculating the 6-fold bond orientational order parameter of the nanopattern, a nearest-neighbor detection algorithm was employed in ImageJ[173]. Both analysis methods were performed on multiple individual areas (1×1 μm) of the same segment. Heat maps were generated using the pcolormat function in Matlab[164].

C.4 AFM imaging and image processing of micronanotopographies

Atomic force microscopy (AFM) topographic imaging was employed to measure the step height of Si microstructures and to determine the topography after spin coating with micelle solution. Imaging was performed on a JPK NanoWizard 3 (JPK Instruments AG) operated in ac mode using ACTA cantilevers (spring constant $\approx$ 40 N/m, resonance frequency $\approx$ 300 kHz; Applied NanoStructures Inc.) for uncoated Si microstructures and MSNL-F (spring constant $\approx$ 0.6 N/m, resonance frequency $\approx$ 100 kHz, Bruker AFM Probes) for micelle-coated samples at scan rates of 1 - 2.5 Hz. Image processing and cross-sectional analysis were done in Gwyddion 2.37 (Gwyddion - free SPM, sourceforge.net)[164].

Appendix-D

D.1 Synthesis of azobenzene

The synthesis of the azobenzene compound 4-(2-(4-(Prop-2-yn-1-yloxy)phenyl) diazenyl)benzoic acid AB 3, and the preparation of mixed azobenzene and polyethylene glycol (PEG-MW: 2000 Dalton) monolayers, as well as the subsequent functionalization with cyclic RGD peptide c(RGD*f*K)[211] were kindly performed by Dr. Michelle Holz and Grace Suana. Packing densities of the mixed monolayers were determined via UV/Vis spectroscopy (Perkin-Elmer Lambda 14 spectrometer)[212,213]. Photoswitching between isomers was carried out with a UV LED combination assembled by Sahlmann Photochemical Solutions. Switching of the azobenzene from *trans*-to-*cis* configuration was induced by irradiation with UV light at a wavelength of 365 nm (Nichia LED, NCSU033, 350 mW) with a measured intensity of approximately 321 $\mu W/cm^2$. Switching back from *cis*-to-*trans* configuration was carried out by irradiating the sample with visible (VIS) light at a wavelength of 440 nm (Roithner LED, VL440-EMITTER, 300 mW) with a measured intensity of approximately 318 $\mu W/cm^2$.

D.2 Cell culturing experiment

Rat embryonic fibroblast 52 wild type cells (Ref52 wt) were maintained in Dulbeccos Modified Eagles Medium (DMEM, Biochrom) supplemented with 10 % Fetal Bovine Serum (FBS, Biochrom) at 37 °C, 5 % CO2 and about 90 % humidity. Before the cells were seeded, the samples were washed once with 70 % ethanol (Walter CMP) and then washed two times with sterilized 1× phosphate buffered saline (PBS, Sigma-Aldrich, P5493) in 6-well plates (Sarstedt). Cells were suspended in Hanks Balanced Salt Solution (HBSS, Sigma-Aldrich, H6648) after trypsinization (0.25 % trypsin/ 0.05 % ethylenediamine tetraacetic acid, Biochrom). In each well, 2×10^4 cells in HBSS were

seeded onto the samples. Azobenzene samples were either in *cis* or *trans* configuration prior to cell seeding (Fig. 3.2 a). The *cis* configuration was generated by 20 s UV illumination. Cells were incubated on the samples for 15 min at room temperature and subsequently washed with 1× PBS, before being fixed with 4 % paraformaldehyde (4 mL, Sigma-Aldrich) at room temperature for 25 min. Afterwards, samples were washed twice with 1× PBS. The number of adhering cells was counted manually using a 10× magnification objective (CACHN 10× 0.25, Olympus) in phase contrast microscopy (CKX41, Olympus) and data were plotted with Origin 9.1 (OriginLab). The assay was carried out in four independent experiments, each of them at least in duplicate.

D.3 Analysis of force-distance curves

The analysis of force-distance curves was carried out using a commercial AFM data processing software (JPK Instruments). Data were plotted and statistical significance was tested with Origin 9.1 (OriginLab).

Appendix-E

E.1 SCFS on push-pull azobenzene

The detachment forces of cells were measured using an atomic force microscope (Nanowizard III, JPK Instruments) mounted onto an inverted light microscope (IX71, Olympus). All experiments were undertaken in HBSS buffer at room temperature. First, tipless Si_3N_4 cantilevers with Au reflective coating and a nominal spring constant in the range of 0.06 to 0.35 N/m (NP-O10, Bruker) were calibrated using the thermal noise method implemented in the JPK AFM software. Then, the calibrated cantilevers were functionalized with Concanavalin A (conA, Sigma-Aldrich, C2272) in order to immobilize single REF52 wt cells according to standard procedures[3,115,194]. To capture a cell, a number of freshly trypsinised cells was injected into the sample chamber and the cantilever was immediately approached to a cell with an applied force of a few nN for 8s. Eventually, the cell-capturing cantilever was carefully lifted off the surface and held resting for 12 min to guarantee stable attachment of the cell[3,115,194].

Force-distance curves were recorded at an approach/retract speed of 30 m/s. Experiments with 1 and 3 s contact times between cell and surface were carried out at a constant force of 500 pN. The force curves were recorded on four different positions on the substrate as defined by the vertices of a 10 $\times$ 10 μm square. 20 and 10 force curves were taken on each of the four positions in the 1 and 3 s contact time experiments, respectively.

Force-distance curves were initially recorded in the dark, i.e. with the c(RGDfK)-azobenzene in the *trans* state, before turning green light (530 nm) on. Subsequently, the surface was set 'active' by switching on the 530 nm light (measured intensity of approximately 182 $\mu W/cm^2$), which is mounted on an objective lens slot and illuminates from underneath. During exposure, force curves were taken at exactly the same four positions of the sample. Each force-taking course (whether the light was switched on

or off) was followed by a 3 min waiting time before commencing with new force measurements in order to let the cell recover from previously taken force curves. Each cell was used for two complete cycles of light OFF/light ON/light OFF courses. Control experiments were conducted on glass substrates to show that cells are not influenced by irradiation.

The analysis of force curves was conducted using JPK Instruments data processing software. Statistical differences were determined using Origin 9.1 (OriginLab).

E.2 Gene expression

The gene expression experiments were kindly performed by Dr. Wei Wang. Quantitative real-time PCR (qRT-PCR): mRNA was extracted and cDNA was synthesized with SuperScriptTM III CellsDirect cDNA Synthesis System using oligo(dT)20 primer (Invitrogen). The qRT-PCR was performed using *GoTaq* qPCR Master Mix (Promega) on Applied Biosystems 7300 Real Time PCR System (ABI) according to the manufacturers protocol. Template cDNA amounts were equilibrated by GAPDH. All primers were diluted to 10 pmol/l. Their concentrations were measured using a Nanodrop spectrophotometer (Thermo Scientific). Each analysis was repeated with three technical replicates. All samples were analyzed using GAPDH as the reference gene. Expression levels were calculated with the Ct method.

E.3 Temperature dependence of biological bonds

In order to study the effect of temperature on the strength of non-covalent biological bonds, the work that has been conducted theoretically and experimentally in the group of Prof. Beebe is presented[201]. Temperature is an important parameter which affects the dissociation rate of biological bonds both in the presence or absence of an externally applied force. At high temperatures, thermal excitation requires less time to yield bond rupture under any applied force. In order to study the temperature dependence of biological bonds, both theoretical and experimental (using AFM) investigations have been conducted. These studies were carried out in the work of Beebe *et al.* on biotin-avidin binding[201]. Both approaches will be discussed in the next two chapters.

E.3.1 Experimental studies using AFM

The experiments conducted with AFM study the relationship between the force required to achieve a complete cantilever-substrate separation and the potential energy of bonding. After each cantilever-substrate contact, a number n of bonds develop and eventually rupture when the cantilever breaks free. As shown earlier, the probability that n number of bindings is formed in each measurement follows a Poisson distribution[214]. Therefore, the force needed to rupture a single bond can be determined by taking a large number of such measurements and perform a Poisson statistical analysis in order to extract the binding force for the case of $n = 1$. Each bond involves a number of operating force forms including hydrogen bonds, van der Waals interactions and polar group attractions[201].

As specified by the properties of the Poisson distribution, the mean μ_n and the variance δ_n^2 of the number of bonds ruptured during cantilever retraction in an AFM experiment (a single force-distance curve) are the same, i.e.,

$$\mu_n = \delta_n^2 \tag{1}$$

The detachment force m for n number of bonds ruptured in a single force-distance curve is determined by

$$m = n \cdot F_i \tag{2}$$

where F_i is the average rupture force of an individual bond. A sampling of a number of AFM force curves produces a mean detachment (pull off event) force μ_m and a detachment force variance δ_m^2. Based on the relation between the measured force and the number of ruptured bonds, the following equations can be obtained

$$\begin{aligned} \mu_m &= \mu_n \cdot F_i \\ \delta_m^2 &= \delta_n^2 \cdot F_i^2 \end{aligned} \tag{3}$$

And because $\mu_n = \delta_n^2$ for a Poisson distribution, the F_i value can be determined

as

$$\mu_m = \frac{\delta_m^2 \cdot F_i}{F_i^2} = \frac{\delta_m^2}{F_i}$$
$$F_i = \frac{\delta_m^2}{\mu_m} \tag{4}$$

Moreover, although they are unlikely to exist, non-specific long-range interactions $F_\circ$ can also be taken into consideration. The mean of the detachment forces can be determined as follows

$$\mu_m = \mu_n \cdot F_i + F_\circ \tag{5}$$

As for the variance, considering that $\mu_n = (\mu_m - F_\circ)/F_i$ and $\delta_m^2 = \mu_n \cdot F_i^2$, the variance is then calculated as shown below

$$\delta_m^2 = \frac{\mu_m - F_\circ}{F_i} F_i^2$$
$$\delta_m^2 = \mu_m F_i - F_i F_\circ \tag{6}$$

The slope of a linear regression curve of the variance versus the mean of a number of measurement sets gives the rupture force value of an individual bond (F_i) (Fig. EE.3.1). An estimated magnitude of any nonspecific (background) forces can be determined from the y-intercept ($-F_i F_\circ$) of that curve.

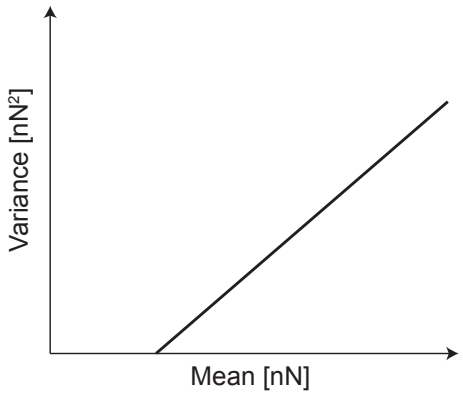

Figure EE.3.1: *According to the Poisson analysis, the slope of the linear regression curve represents the force magnitude for a single-bond rupture. Figure is modified from Lo et al.*[201]

The unbinding force for an individual bond was measured over a range of temperatures that varied between 13-37 $^{\circ}C$ and the results showed a reduction in force associated with an increase in temperature.

E.3.2 Theoretical studies

In each cantilever-substrate contact, n number of bindings develop and eventually rupture when the cantilever is pulled off. These bindings cause cantilever bending by a length of d during retraction, which leads to a force exerted on the sample. This force (F_1) is

$$F_1 = K_{canti} \cdot d \tag{7}$$

where K_{canti} is the cantilever spring constant. This stretching force is opposed by the force applied by n number of bonds when they are stretched by an amount δr in the direction of cantilever. This opposing force that balances the applied force is $K_{bond}.\delta r$. Each bond experiences this force (F_2), thus for a number n of bonds the equation becomes

$$F_2 = nK_{bond} \cdot \delta r \tag{8}$$

The other force (F_3) resulting from the stretching of bonds which balances the applied force and acts in the direction of the cantilever can be expressed as follows

$$F_3 = K_{canti} \cdot \delta r \tag{9}$$

Eventually, all opposing forces reach a balance state with

$$n.K_{bond} \cdot \delta r = K_{canti}(d - \delta r) \tag{10}$$

Furthermore, the energy deposited in the form of potential energy (E_p) within each bond can be determined as follows

$$E_p = \frac{1}{2} K_{bond} [\frac{K_{canti} \cdot d}{K_{canti} + nK_{bond}}]^2 \tag{11}$$

The net energy barrier δE_T required to be surmounted by thermal energy in order to rupture n bonds include several terms. The first term accounts for n times the energy ΔE^+ required to rupture a single binding in the absence of an external force. The second is a negative term that corresponds to the mechanical energy E_p applied onto n bindings by the AFM cantilever. The last term is for the energy dissipated due to viscous drag E_v that results from operating at a finite pulling rate. As a result, that energy barrier δE_T can be expressed as follows

$$\begin{aligned} \delta E_T &= n \cdot \Delta E^+ - n \cdot E_p + n.E_v \\ \delta E_T &= n \cdot \Delta E^+ - \frac{1}{2} n \cdot K_{bond} [\frac{K_{canti} \cdot d}{K_{canti} + nK_{bond}}]^2 + \frac{K_{canti} \cdot d}{K_{canti} + nK_{bond}} n \cdot \nu \cdot \gamma \end{aligned} \tag{12}$$

where ν is the pulling rate in $\mu m/s$ and γ is the damping coefficient in $pN.s/nm$.

The time needed to rupture n bonds (τ_R) is given as follows

$$\tau_R = \tau_D \cdot e^{\frac{\delta E_T}{n \cdot k_B T}} \tag{13}$$

where (τ_D) represents the time needed for the thermal dissociation of bonds in the absence of external forces and $n.k_BT$ is the average thermal energy available in the n bindings.

Hence, δE_T can be shown as

$$\delta E_T = n \cdot k_B T \cdot ln(\frac{\tau_R}{\tau_D}) \tag{14}$$

Combining equation 12 and 14, we obtain

$$n \cdot K_B T \cdot ln(\frac{\tau_R}{\tau_D}) = n \cdot \Delta E^+ - \frac{1}{2} n \cdot K_{bond} [\frac{K_{canti} \cdot d}{K_{canti} + nK_{bond}}]^2 + \frac{K_{canti} \cdot d}{K_{canti} + nK_{bond}} n \cdot \nu \cdot \gamma \tag{15}$$

Because $K_{bond} >> K_{canti}$, as proven below to be valid for our experimental conditions,

the equation becomes

$$\begin{aligned} n \cdot K_B T \cdot ln(\frac{\tau_R}{\tau_D}) &= n \cdot \Delta E^+ - \frac{1}{2} n \cdot K_{bond} [\frac{K_{canti} \cdot d}{n K_{bond}}]^2 + \frac{K_{canti} \cdot d}{n K_{bond}} n \cdot \nu \cdot \gamma \\ n \cdot K_B T \cdot ln(\frac{\tau_R}{\tau_D}) &= n \cdot \Delta E^+ - \frac{1}{2} \frac{(K_{canti} \cdot d)^2}{n K_{bond}} + \frac{K_{canti} \cdot d}{K_{bond}} \cdot \nu \cdot \gamma \end{aligned} \tag{16}$$

If $\nu = 30 \mu m/s$ and $\gamma = 2 \times 10^{-8} pN \cdot s/nm$, then $\nu \cdot \gamma = 6 \times 10^{-4} pN$. On the other hand, $K_{canti} \cdot d \approx 0.04(N.m) \times 10^{-9}(m) \approx 40 pN$. Therefore, $K_{canti} \cdot d >> \nu \cdot \gamma$ and hence we can exclude the term

$$\frac{K_{canti} \cdot d}{K_{bond}} \nu \cdot \gamma$$

and thus equation 16 becomes

$$n \cdot K_B T \cdot ln(\frac{\tau_R}{\tau_D}) = n \cdot \Delta E^+ - \frac{1}{2} \frac{(K_{canti} \cdot d)^2}{n K_{bond}} \tag{17}$$

For equation 17 to reproduce the Poisson distribution of forces, each component in the equation must scale linearly with the number of bindings (n) present. Hence, the cantilever force ($K_{canti} \cdot d$) is linearly proportional to n. That is

$$K_{canti} d = F_{total} = n F_i \tag{18}$$

where F_i is the force needed to rupture a single binding. In the calculation of temperature-dependent binding force, only the last rupture event should be taken into consideration, as no rebinding can take place. Therefore, the calculation done for the force needed to cause rupture within time τ_R is only accurate for a single binding, i.e. $n = 1$.

Therefore, equation 17 becomes

$$K_B T \cdot ln(\frac{\tau_R}{\tau_D}) = \Delta E^+ - \frac{1}{2} \frac{F_i^2}{K_{bond}} \tag{19}$$

Hence, the temperature dependence of individual binding rupture force at constant

loading rate can be expressed as follows

$$F_i^2 = 2K_{bond}[\Delta E^+ - K_B T \cdot ln(\frac{\tau_R}{\tau_D})] \tag{20}$$

When the bond rupture time is given by $\tau_R \approx 10^{-3}s$ and the diffusion time is about $\tau_D \approx 10^{83}s$, then the ratio of both is displayed as $\tau_R/\tau_D \approx 10^5$ (ratio in logarithm). Variations up to 2 orders of magnitude will only have a limited effect on force and energy calculations.

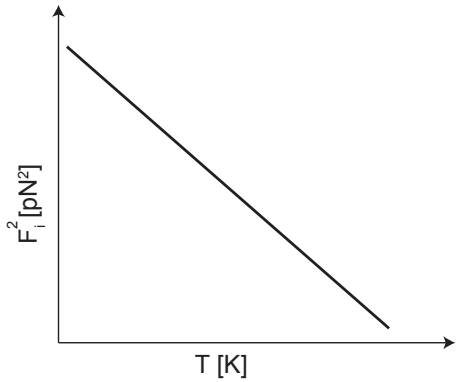

Figure EE.3.2: *Bond strength as a function of temperature. Figure is modified from Lo et al.*[201].

Fig. EE.3.2 demonstrates the theoretical bond rupture force dependance on temperature where the Slope=$K_{bond} \approx 17.4 \pm 1.4$ N/m and the y-intercept=$\Delta E^+ \approx 7.1 \pm 0.8$ kcal/mol. Thus, $K_{bond} >> K_{canti}$ as mentioned earlier.

Acknowledgments

I would like to express my sincere gratitude and appreciation to my adviser Prof. Christine Selhuber-Unkel for giving me the opportunity to work in her group on this great subject and for the continuous support during my PhD study.

I would also like to thank Prof. Rainer Herges for supporting my project and also thank Dr. Michelle Holz and Grace Suana for kindly providing us with the sample we needed in this work.

I would like to acknowledge the funding of this project from the Deutsche Forschungsgemeinschaft (DFG) through the SFB 677 (project B11) as well as from the European Research Council (ERC starting grant no. 336104).

I would like to thank Prof. Rainer Adelung for agreeing to review this work.

I would also like to thank Prof. Joachim Spatz and Yvonne McDuffie for their assistance in establishing the Block-Copolymer Micelle Nanolithography process in our lab.

I would like to thank Dr. Constanze Lamprecht for her support with the Atomic Force Microscope.

I would like to thank Dr. Wei Wang and Dr. Qian Li for their assistance in cell adhesion experiments.

I would like to express my sincere thanks to my friends and colleagues in the group Hendrikje Neumann, Dr. Sren Gutekunst, Dr. Carsten Grabosch, Steven Huth, Mohammadreza Taale, Dr. Julia Reverey, Michael Timmermann, Dr. Britta Hesseler and Manuela Lieb for providing a great working environment and for the countless fruitful discussions.

I would like to also thank all my students and research assistants (HiWi) Julia Purtov, Ali Raza, Karoline Teichmann, Hannes Westerhaus, Anneke Mhring, Florian

Uhrbrock, Yannic Hallier, Katharina Siemsen, Katharina Gpfert and Sandra Sindt for their kind help.

I would like to thank Dr. Anna-Marie Schuette and Frederike Schmied for the team work we had during our Atomic Force Microscopy experiments.

I would like to thank my friends Bodo Henkel, Larissa Sander, Ali Tavassolizadeh and Husam Taher for the spiritual support and the wonderful times we had.

I would also like to express my sincere gratitude to my girlfriend Mareike Hesebeck for her constant support throughout writing this thesis. I would also like to thank Mareike's family for their hospitality and kindness.

Finally, I would like to thank my family for the encouragement throughout my studies.

Publications

Kadem, L. F., Lamprecht, C., Purtov, J., and Selhuber-Unkel, C. (2015). Controlled Self-Assembly of Hexagonal Nanoparticle Patterns on Nanotopographies. *Langmuir*, 31(34), 92619265.

Kadem, L. F., Holz, M., Suana, K. G., Li, Q., Lamprecht, C., Herges, R., and Selhuber-Unkel, C. (2016). Rapid Reversible Photoswitching of Integrin-Mediated Adhesion at the Single-Cell Level. *Advanced Materials*, 28(9), 17991802.

Kadem, L. F., Holz, M., Suana, K. G., Wang, W., Herges, R., and Selhuber-Unkel, C. Light-Triggered, High Frequency Stimulation of Integrin-Mediated Adhesion. *In Preparation.*

Mehl, C., Kern, M., Schuette, A. M., **Kadem, L. F.**, and Selhuber-Unkel, C. Adhesion of Living Cells to Abutment Materials, Dentin, and Adhesive Luting Cement with Different Surface Qualities. *In preparation.*